MEASUREMENT OF (ALPHA, NEUTRON) REACTIONS AND DEVELOPMENT OF ANALYSIS TOOLS WITH THE MAJORANA DEMONSTRATOR

By

Tupendra Kumar Oli

M.S., Tribhuvan University, 2014
M.S., The University of South Dakota, 2018

A Dissertation Submitted in Partial Fulfillment of
the Requirements for the Degree of
Doctor of Philosophy

Department of Physics

Physics Program
In the Graduate School
The University of South Dakota

August 2022

The members of the Committee appointed to examine
the Dissertation of Tupendra Kumar Oli find it
satisfactory and recommend that it be accepted.

Chairperson, Dr. Wenqin Xu

Dr. Ralph Massarczyk

Dr. Joel Sander

Dr. Xinhua Bai

Dr. Chaoyang Jiang

ABSTRACT

Neutrinoless double-beta decay ($0\nu\beta\beta$) is a hypothetical nuclear transition which, if observed, would prove that neutrinos are Majorana particles. In addition, the decay rate could provide an effective neutrino mass scale. The decay violates lepton number conservation and could offer a potential path to explain the matter-antimatter asymmetry in the universe via leptogenesis. However, the experimental observation of this decay is very challenging and would require excellent energy resolution of detectors, low background levels, and high exposure. The MAJORANA DEMONSTRATOR experiment searches for this decay in ^{76}Ge using P-type Point Contact (PPC) High Purity Germanium (HPGe) detectors. In addition, the DEMONSTRATOR is probing a broad range of physics, including both Standard Model (SM) physics and Beyond the Standard Model (BSM) physics, thanks to the experiment's excellent energy performance, low analysis energy threshold, and low background. This dissertation will begin with an overview of neutrinos and neutrinoless double-beta decay physics. It will then briefly outline the MAJORANA DEMONSTRATOR experiment and its result on $0\nu\beta\beta$ search. The DEMONSTRATOR has achieved the best-in-field energy resolution, which is the result of intrinsic properties of detectors and analysis efforts. A brief description of the energy calibration procedure and the energy systematic study of DEMONSTRATOR will be presented. Then, the dissertation will describe an experimental study of ^{13}C(α,n)^{16}O reactions in MAJORANA's calibration data. The findings and impacts in low-background experiments will be presented. Finally, it will describe the machine learning approach of analyzing waveforms to discriminate signal-like and background-like events for $0\nu\beta\beta$ searches.

Dissertation Advisor Approval

Acknowledgements

I am incredibly grateful to my Ph.D. advisor Dr. Wenqin Xu for his unwavering support, motivation, mentoring, and guidance in making me a better researcher. For my Ph.D. study, I could not have asked for a greater mentor and advisor.

I am deeply indebted to Dr. Ralph Massarczyk, who has helped me in so many ways. I would like to extend my sincere thanks to Dr. Joel Sander, Dr. Xinhua Bai, and Dr. Chaoyang Jiang for their support and valuable suggestions.

I am also grateful to Dr. Pinghan Chu, for his insightful suggestions and feedback on the analysis. Special thanks to Dr. Aobo Li for his invaluable guidance on machine learning. I would not have made it this far without his help.

Special thanks to Dr. Steve Elliot for encouraging me by recognizing the importance of my research at an early stage. Many thanks to Dr. Mariano Lopez for his guidance and fruitful discussion about the energy calibration.

My appreciation also goes out to all my laboratory colleagues, C. J. Barton, Dr. Nabin Poudyal and Laxman Paudel. I had the pleasure of working with you all.

It was my best decision to choose USD Physics Program and join in the Majorana collaboration for my Ph.D. research. Thanks should be to all the Majorana collaborators. Also, thanks to all the faculty and staff in the department of physics.

Last but not least, I would like to extend my sincere thanks to my wife Shrijana DC for all her continuous encouragement and support. Thanks to my parents, sister, and brother for believing in me and caring in so many ways.

This material is based upon work supported by the U.S. Department of Energy, Office of Science, Office of Nuclear Physics, the Particle Astrophysics and Nuclear Physics Programs of the

National Science Foundation, and the Sanford Underground Research Facility. I specially acknowledge support from the Particle Astrophysics Program and Nuclear Physics Program of the National Science Foundation through grant numbers PHY-1812356 and PHY-2111140. Also, I am grateful to use the High-Performance Computing facilities at University of South Dakota funded by the NSF (OAC-1626516).

Any opinions, findings, and conclusions or recommendations expressed in this material are those of the author and do not necessarily reflect the views of the funding agencies.

Table of Contents

List of Tables

List of Figures

1

Neutrinos and Neutrinoless Double-Beta Decay

1.1 A Brief Introduction of Neutrino

1.1.1 Discovery of Neutrino

In nuclear β decay, it was expected that the energy of the emitted β-particle would be discrete. In contrast, extensive experimental efforts by J. Chadwick, C. D. Ellis, W. A. Wooster, L. Meitner, W. Orthmann, O. Hahn, and others observed a continuous energy spectrum with a well-defined endpoint energy [1–4]. Experimental uncertainties were settled after multiple measurements ended up with similar observations. However, theoretically, this observation resulted a dilemma as it violates energy conservation.

In 1930, Wolfgang Pauli suggested that some unknown, electrically neutral spin-1/2 particle may be produced additionally in nuclear β decay. Both energy and angular momentum are conserved in the presence of this particle. In 1934, three years after Chadwick discovered neutron [5], Enrico Fermi proposed the theory of weak interaction to explain the nuclear β-decay [6] and called the unknown particle neutrino. The postulated particle was electron anti-neutrino with the assumption that it is involved in the weak force transformation of a neutron into a proton, as shown in Fig. 1.1. The theory of β decay was not only capable of explaining the continuous energy spectrum but also the inverse β decay. The inverse β decay is the nuclear process in which a nucleus captures either neutrino or anti-neutrino and gives positron or electron, respectively. Two possible inverse β decays are given in Eq. 1.1. The theory also predicted that the cross section of inverse β decay would be exceedingly tiny, given that a weak force would mediate the process.

$$
\begin{aligned}
p + \bar{\nu}_e &\rightarrow n + e^+ \\
n + \nu_e &\rightarrow p + e^-
\end{aligned}
\tag{1.1}
$$

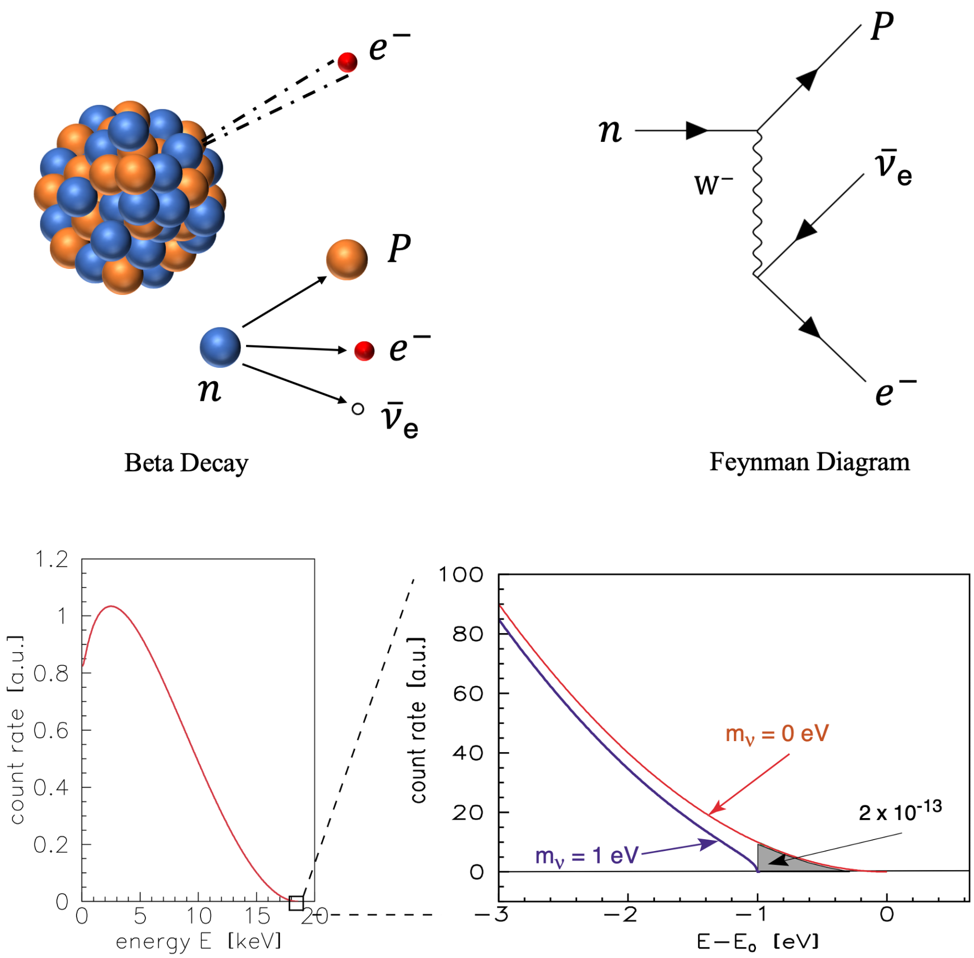

FIGURE 1.1: (Top Left): A schematic of a β^- decay, where a neutron changes into a proton releasing an electron and an electron anti-neutrino. (Top Right): A Feynman diagram of β^- decay. (Bottom Left): β^- decay energy spectrum of tritium measured by KATRIN experiment [7]. (Bottom Right): The same spectrum near the endpoint energy, E_0, considering neutrino masses of 0 and 1 eV.

The inverse β decay process provides a method for establishing the existence of neutrinos. In 1956, Fred Reines and Clay Cowan detected electron anti-neutrinos for the first time through inverse β decays [8]. In this experiment, electron anti-neutrinos from the Savannah River nuclear reactor were captured in a large water tank containing cadmium chloride (CdCl2) solution. The reaction produced neutrons and positrons, which annihilated with electrons, and the neutrons get diffused into the solution. The secondary particles that resulted from this reaction were 511 keV γ-rays from the annihilation, and high energy $\sim$ 8 MeV γ-rays when the diffused neutrons were detected.

1.1.2 Parity in Weak Interaction

Parity symmetry was considered to be conserved in weak interaction like in strong and electromagnetic interactions. However, in 1956, T.D. Lee and C.N. Yang suggested that parity could be violated in weak interaction [9] as well, based on the Theta-Tau Puzzle observed in experiments. After a year, Wu and collaborators [10] confirmed that parity symmetry is violated in the weak interaction. In 1958, the Goldhaber experiment measured the helicity of the neutrinos and found that neutrinos are left-handed particles and anti-neutrinos are right-handed particles [11], suggesting that parity is maximally violated in weak interaction; equivalently, charge symmetry is violated. However, the combined CP symmetry seems to be conserved in the weak interaction involving only the leptons, although it is known to be violated with quarks. For example, C on ν_L gives $\bar{\nu}_L$ which is not observed but adding P on it gives $\bar{\nu_R}$ which exist.

1.1.3 Three Flavors of Neutrinos

In 1948, a continuous energy spectrum of muon decay was observed, suggesting that two neutral particles must have emitted with an electron [12]. Two neutral particles were assumed to be two neutrinos, leading to the two-neutrino hypothesis. In 1962, a pion decay study using Alternating Gradient Synchrotron (AGS) accelerator showed that the neutrino beam that was produced along the way produced muons in the detector [13]. The observation verified that the second neutrino was muon-neutrino, μ_ν associated with a muon. The third charged lepton τ was discovered in 1975 in e^+e^- collisions [14]. So, a third neutrino was expected to be associated with this charged lepton. After nearly 25 years, the observation of tau-neutrino, ν_τ, associated with τ was confirmed by DONUT experiment [15]. There exist three flavors of neutrinos (ν_e, ν_μ, ν_τ) that are associated with three leptons.

1.1.4 Neutrinos in the Standard Model

By the 1970s, the Standard Model of particle physics emerged based on rapid expansion of knowledge in both lepton and hadron sectors. The Standard Model of particle physics is a theory that is an expanded form of electroweak unification to include strong interaction based on $SU(3)\times SU(2)\times U(1)$ symmetry. The $SU(2) \times U(1)$ refers to symmetry group in electroweak interaction [16–18], and $SU(3)$ refers to the symmetry group in strong interaction [19]. The Standard Model explains the way particles interact with one another by exchanging the fundamental particles. It consists of spin-1/2 fermions that are quarks and leptons each with three generations, four spin-1 bosons, and a spin-0 Higgs boson, as shown in Fig. 1.2. The photon mediates the electromagnetic force, W and Z bosons mediate the weak force, and the gluon mediates the strong force.

In the Standard Model, elementary fermions acquire their mass through the Higgs mechanism, where they interact with the Higgs field and acquire effective masses. The frequency of interaction measures how massive the particle could be. Also, the particle's handedness changes after the interaction with the Higgs field, *i.e.* left-handed particles become right-handed and vice-versa. However, neutrinos and anti-neutrinos were found to have a single-handedness, and the Higgs mechanism no longer applies for neutrino mass in the Standard Model. Therefore, they are the only fermions in the Standard Model with zero mass.

The Standard Model is a well-tested and powerful theory for understanding how the nature works in the most fundamental ways. However, it fails to include gravity and can not explain some compelling questions, for example, what is dark matter? Why is there a matter-antimatter asymmetry in the Universe? More importantly here, why do neutrinos have non-zero mass which was indicated by neutrino oscillation as discussed in next Section 1.2?

1.2 Non-Zero Neutrino Mass

1.2.1 Neutrino Oscillation

In 1958, Pontecorvo hypothesized a concept of neutrino mixing [20], which was further refined by Maki, Nakagawa, and Sakata in 1962 [21]. It assumed the existence of three mass eigenstates, ν_1, ν_2, ν_3 corresponding to three neutrinos called flavor eigenstates. The mass eigenstates and flavor eigenstates are different from one another. One set of eigenstates can be expressed as a quantum

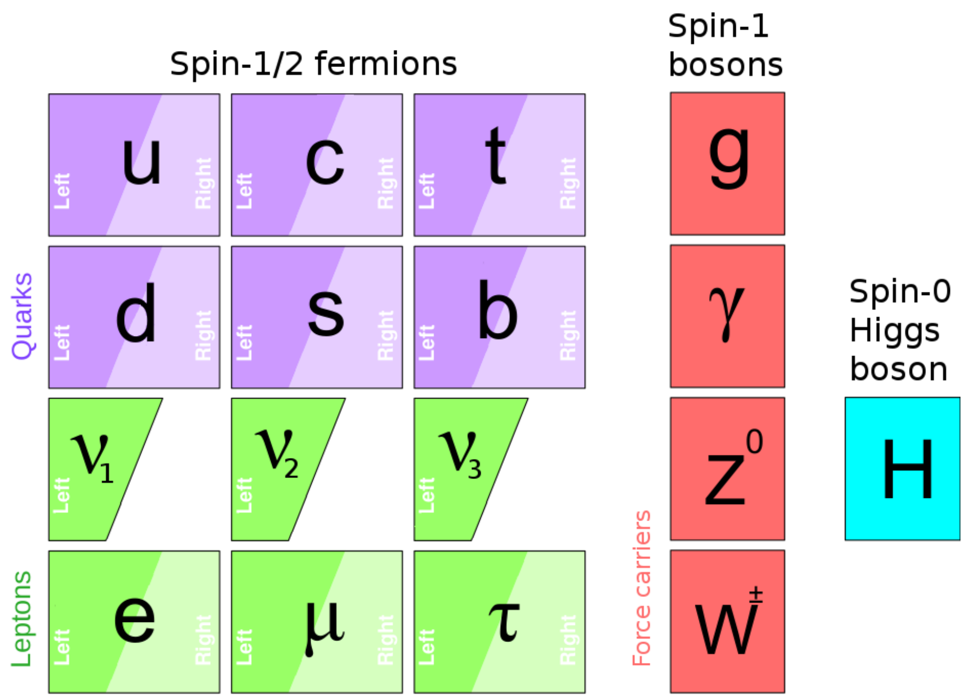

FIGURE 1.2: Summary of all experimentally observed Standard Model particles. All left-handed and right-handed fermions are shown separately, with a gap in right-handed neutrinos which are not observed. Four spin-1 bosons and a spin-0 boson are shown. The diagram is adapted from CERN document server (`https://cds.cern.ch/record/2262550/plots`).

mechanical superposition of another set. For example, a flavor eigenstate, ν_α, where α is e, μ or τ is a mixture of three mass eigenstates ν_1, ν_2 and ν_3 with a mixing determined by the components of $U_{\alpha i}$ as given by Eq. 1.2.

$$|\nu_\alpha\rangle = \sum_i U_{\alpha i}\nu_i = U_{\alpha 1}\nu_1 + U_{\alpha 2}\nu_2 + U_{\alpha 3}\nu_3 \tag{1.2}$$

The Pontecorvo-Maki-Nakagawa-Sakata (PMNS) matrix, also called a leptonic mixing matrix assuming neutrino obeys the Dirac equation, is given by Eq. 1.3.

$$U = \begin{pmatrix} 1 & 0 & 0 \\ 0 & c_{23} & s_{23} \\ 0 & -s_{23} & s_{23} \end{pmatrix} \times \begin{pmatrix} c_{13} & 0 & s_{13}e^{-i\delta_{CP}} \\ 0 & 1 & 0 \\ -s_{13}e^{i\delta_{CP}} & 0 & c_{13} \end{pmatrix} \times \begin{pmatrix} c_{12} & s_{12} & 0 \\ -s_{12} & c_{12} & 0 \\ 0 & 0 & 1 \end{pmatrix} \tag{1.3}$$

Here, c_{ij} and s_{ij} refer to mixing angle terms; $cos\theta_{ij}$, and $sin\theta_{ij}$ respectively. The δ_{CP} is the CP-violating phase term.

The observation of neutrino oscillation is compelling evidence that indicates neutrinos have non-zero mass. The Solar Neutrino Problem in the 1960s was the first hint behind the neutrino oscillation [22, 23]. The problem refers to the discrepancies in the measured and predicted solar neutrino flux, where only one-third of neutrino flux was measured. In comparison with the prediction based on the well-established solar fusion model [24].

Mixing neutrino eigenstate directly leads to the phenomenon of neutrino oscillation [25]. Pontecorvo hypothesized this process in 1969 to explain the missing neutrinos in the Solar Neutrino Problem. It refers to the change of neutrino flavor eigenstates after traveling through some macroscopic distance. For a simple illustration, we can assume just two neutrino eigenstates ν_α and ν_β. The neutrino produced in ν_α eigenstate at the source can be detected as a different eigenstate ν_β at the detector. The probability of measuring such flavor change in a vacuum is given by Eq. 1.4.

$$P_{\alpha\to\beta} = sin^2(2\theta_{ij})sin^2\left(\frac{\Delta m_{ij}^2 L}{4E}\right) \tag{1.4}$$

Here, θ_{ij}, $\Delta m_{ij}^2 = m_i^2$ - m_j^2, L, and E are the mixing angle, mass splittings, distance, and neutrino energy, respectively. In Eq. 1.4, probability of oscillation would be zero if either of θ_{ij} and Δm_{ij}^2 are zero. Therefore, observation of non-zero oscillation probability represents the evidence of both neutrino mixing and oscillation.

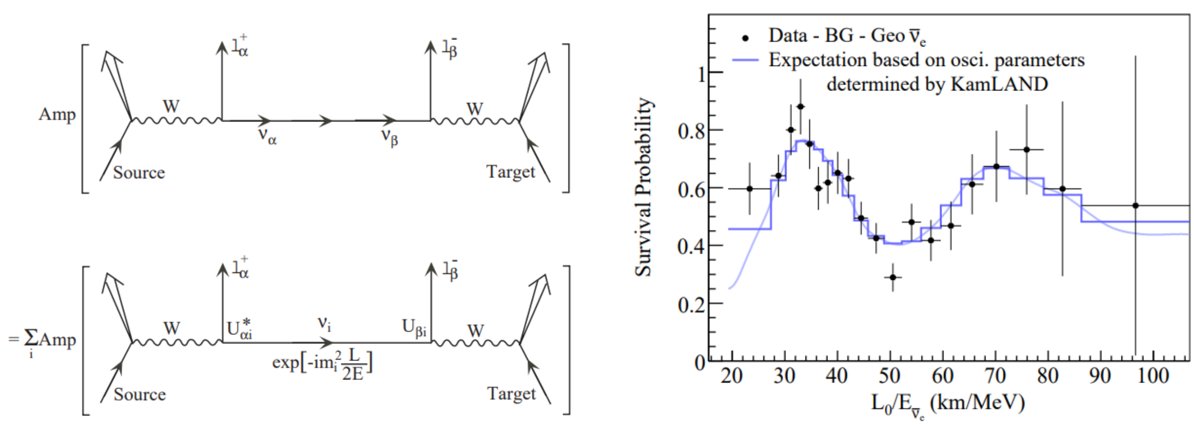

FIGURE 1.3: (Left) A diagram depicts neutrino oscillation. A neutrino in flavor eigenstate ν_α is created with corresponding charged lepton l_α^+ at source travels some distance and produces different charge lepton l_β^-. The amplitude of the process gives the probability of such flavor change contributed by all mass eigenstates. The diagram is adapted from [26]. (Right) Neutrino oscillation pattern measured by KamLAND [27]. The survival probability, *i.e.* $P_{\bar{\nu}_e\to\bar{\nu}_e}$, as a function of $\frac{L_0}{E}$ expected based on best fit oscillation parameters is well fitted with the data.

The evidence of neutrino oscillation observed by SNO collaboration [28] resolved the Solar Neutrino Problem. Similar to the Solar Neutrino Problem, the deficit in atmospheric neutrino was observed by SuperKamiokande in 1998 [29] and reactor neutrino by KamLAND in 2003 [30]. The discrepancies in the flux of solar neutrinos, atmospheric neutrinos, and reactor neutrinos were direct evidences behind the neutrino oscillation. Different experiments reported a good agreement between data and prediction after considering neutrino oscillation. For example, KamLAND observed a good agreement between data and prediction, as seen in Fig. 1.3. As seen in Eq. 1.4, the probability of neutrino oscillation oscillates as a function of L/E. An expected oscillation pattern measured in KamLAND experiment is shown in Fig. 1.3.

Neutrino oscillation experiments measure the oscillation parameters, including mixing angles, mass splittings, and the CP-violating phase. For example, atmospheric neutrino experiments are mostly sensitive to measure $sin^2\theta_{23}$ and Δm^2_{31}. There are many experimental efforts to precisely measure the parameters. The current status of those parameters is summarized in Ref. [31]. While these experiments can measure the precise value of mixing angles and mass splittings, they can not measure the absolute values of mass eigenstates. Furthermore, the sign of Δm^2_{23} is unknown, which brings the neutrino mass ordering problem. It is known that $m_2 > m_1$ but an unknown sign of Δm^2_{23} brings two possibilities in the mass ordering called Normal Ordering (NO) and Inverted Ordering (IO). The term NO refers to the case of $m_3 > m_2 > m_1$ and IO refers to $m_2 > m_1 > m_3$.

1.2.2 Neutrino Mass Mechanism

As discussed earlier, neutrino oscillation provided evidence of non-zero neutrino mass, unlike predicted in Standard Model. However, the mechanism of how neutrino acquires mass can not be explained as other Standard Model particles do. The other spin-1/2 fermions in the Standard Model are the Dirac particles [33] and acquire mass through the Higgs mechanism. The Dirac equation and Dirac Lagrangian ($\mathcal{L}_\mathcal{D}$) for relativistic spin-1/2 particles is given in Eq. 1.5.

$$\begin{aligned} (i\gamma^\mu \partial_\mu - m)\psi = 0 \\ \mathcal{L}_\mathcal{D} = \bar{\psi}(i\gamma^\mu \partial_\mu - m)\psi \end{aligned} \tag{1.5}$$

where, γ^μ are the Dirac spinors, and the Dirac mass of the particle is given by Eq. 1.6.

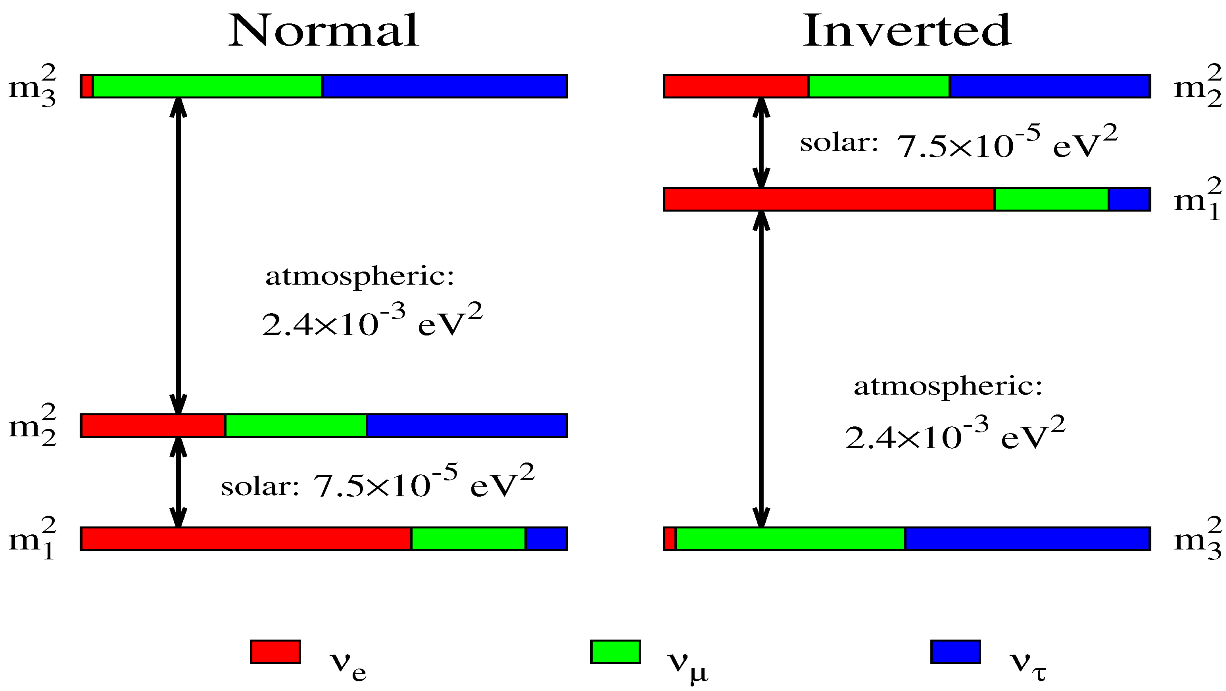

FIGURE 1.4: A depiction of normal and inverted mass ordering with the measured mass splitting values (not shown in the scale), adapted from Ref. [32].

$$m\bar{\psi}\psi = m\bar{\psi}_L\psi_R + m\bar{\psi}_R\psi_L \tag{1.6}$$

Therefore, Dirac particles acquire mass through couplings of left-handed and right-handed fields. However, right-handed neutrinos are not observed.

An alternative mass mechanism proposed by Ettore Majorana exist for neutral fermions [34]. The Majorana equation and Lagrangian are given by Eq. 1.7.

$$\begin{aligned} i\gamma^\mu\partial_\mu\psi - m\psi^C &= 0 \\ \mathcal{L}_{\mathcal{M}} &= \bar{\psi}\big(-i\gamma^\mu\partial_\mu\psi + m\psi^C\big) \end{aligned} \tag{1.7}$$

where,

ψ^C is charge-conjugated field given by:

$\psi^C = \mathcal{C}\psi^*$, ψ^* is the complex conjugate spinor.

Under this assumption, the Majorana field no longer needs left-handed and right-handed spinors like in the Dirac field. Instead, it can be constructed from either left-handed or right-handed spinors as given by either equation in Eq. 1.8 [1]. Furthermore, in any of the fields in Eq. 1.8 under the above assumptions, it can be shown that $\psi^C = \psi$, which tells that a Majorana particle is its own anti-particle. However, the Standard Model does not hold charge conjugation symmetry for other charged fermions. Therefore, neutrinos are the only Standard Model particles that could obey the Majorana equation.

$$\begin{aligned} \psi &= \psi_L + \psi_L^C \\ \psi &= \psi_R + \psi_R^C \end{aligned} \tag{1.8}$$

In the case of the neutrino, the Dirac mass term can be generated from left-handed and right-handed neutrino fields. However, Majorana mass term can be generated from either ν_L or ν_R. It is expected that if neutrinos have Dirac mass term, then it is likely to contain Majorana mass term as well. Another key difference is that the Majorana mass term violates the total lepton number conservation while the Dirac mass term does not, as seen in Fig. 1.5. However, lepton number conservation is an accidental symmetry in Standard Model without being associated with a known fundamental symmetry. At the same time, total lepton number violation could be highly related to baryon number violation.

If the neutrino mass eigenstates are Majorana, the PMNS matrix may contain additional Majorana CP phases; α_1 and α_2. The PMNS matrix for Majorana neutrinos would take the form as:

$$U_M = U_D \times \begin{pmatrix} e^{i\frac{\alpha_1}{2}} & 0 & 0 \\ 0 & e^{i\frac{\alpha_2}{2}} & 0 \\ 0 & 0 & 1 \end{pmatrix} \tag{1.9}$$

where,

U_D is the matrix represented by Eq. 1.3.

The generation of Majorana neutrino mass can be realized by various models, but all require BSM physics. Here, I will explain the well-motivated Type-I See-Saw mechanism that requires a minimal extension of the Standard Model. For other models, see Ref. [36]. The type-I See-Saw model assumes that an extremely heavy right-handed neutrino field exists so that Lagrangian would

[1] https://warwick.ac.uk/fac/sci/physics/staff/academic/boyd/stuff/neutrinolectures/lec_neutrinomass_writeup.pdf

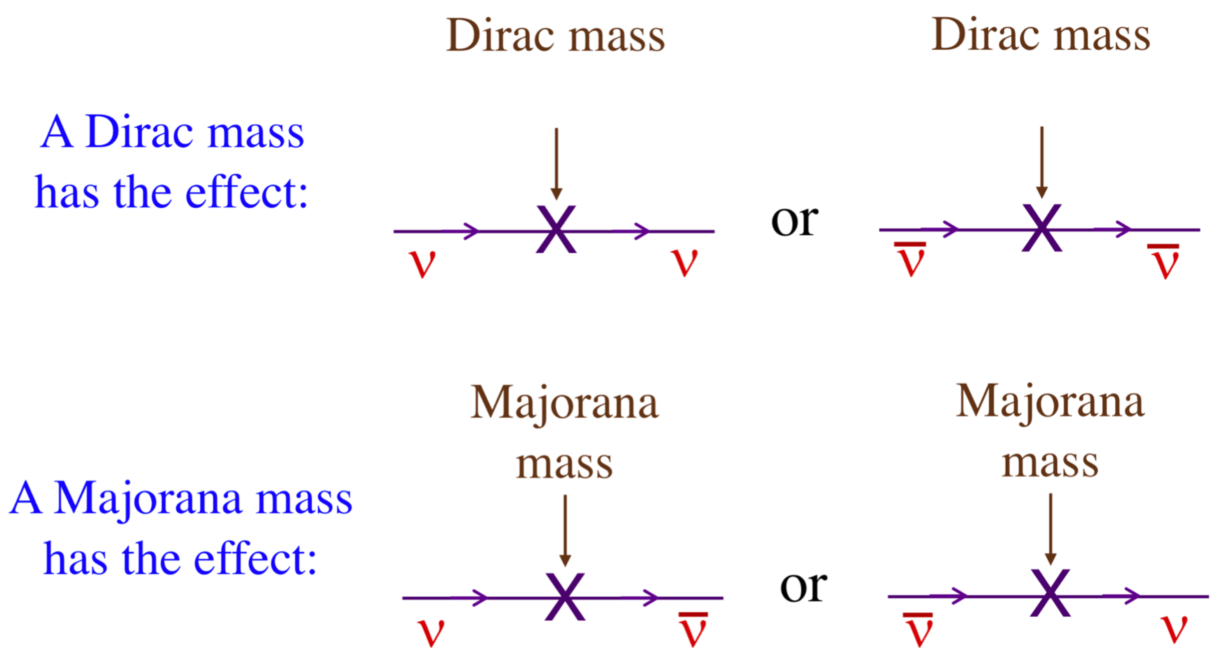

FIGURE 1.5: The effect of Dirac and Majorana mass terms in the Lagrangian. Since the lepton number (L) for neutrino is $+1$ and anti-neutrino is -1, the Dirac mass term conserves the lepton number while the Majorana mass term does not. The diagram is adapted from Ref. [35].

have both Dirac mass term and right-handed Majorana mass term. Using the similar notation as in Ref. [35], the Lagrangian would now appear as:

$$\mathcal{L} = -\frac{1}{2}\left[\bar{\nu}_L^c, \bar{\nu}_R\right] \begin{bmatrix} 0 & m_D \\ m_D & m_R \end{bmatrix} \begin{bmatrix} \nu_L \\ \nu_R^c \end{bmatrix} \tag{1.10}$$

where,

$M_\nu = \begin{bmatrix} 0 & m_D \\ m_D & m_R \end{bmatrix}$ is the neutrino mass matrix. m_D and m_R are the Dirac and right-handed Majorana mass, respectively. The Dirac mass, m_D, can be regarded as the mass scale comparable to the masses of other fermions in the Standard Model, while $m_R >> m_D$. Also, M_ν can be diagonalized [35], which gives two mass eigenvalues:

$$\begin{aligned} m_1 &\simeq \frac{m_D^2}{m_R} \\ m_2 &\simeq m_R \end{aligned} \tag{1.11}$$

In Eq. 1.11, m_1 would be a light neutrino mass and there exists a heavy neutrino with mass $m2$.

Therefore, lighter neutrino mass also opens a window for unprobed high-energy physics in a See-Saw model.

1.3 Implication of Majorana Neutrinos

A confirmation of neutrinos to be a Majorana fermion could answer some of the fundamental questions in particle physics:

- It is possible to answer why neutrino mass is very tiny compared to other spin-1/2 fermions in the Standard Model.
- It could shed light on the mystery of matter-antimatter asymmetry in the universe. The possibility of the existence of very heavy neutrinos gives the idea of a process called *leptogenesis*, which refers to the generation of lepton-antilepton asymmetry in the early universe. Through the Sphaleron process [37], net lepton number can be transferred into net baryon number as a from of baryogenesis, *i.e.* the generation of baryon-antibaryon asymmetry Sakharov proposed the three conditions for *baryogenesis* [38].
  - Violation of Baryon number
  - Violation of C and CP
  - Violation out of thermal equilibrium

  Leptogenesis is an attractive solution to the baryogenesis. Therefore, if neutrinos were proven to be a Majorana fermion, the missing anti-matter in the current universe could be explained. One of the practical methods to test whether neutrinos are Majorana fermions is called neutrinoless double beta decay, which will be discussed in the next section.

1.4 Neutrinoless Double-Beta Decay

In some nuclei with even number of protons and neutrons, single β-decay might be forbidden due to the excess mass of their daughter nuclei. In 1935, Goeppert-Mayer pointed out that such nuclei, however, could undergo a second-order weak interaction process, $2\nu\beta\beta$, and calculated the probability of such process [39]. In such decay, two bound neutrons in the nucleus decay to two protons emitting two electrons and two anti-neutrinos as:

$$(A, Z) \rightarrow (A, Z + 2) + 2e^- + 2\bar{\nu}_e \tag{1.12}$$

Such decay is extremely rare and has been measured in 11 isotopes so far (with half lives on the order of 10^{18} - 10^{24} year) as listed in Table 2 of Ref. [40]. The first direct measurement was performed with ^{82}Se in 1987 [41].

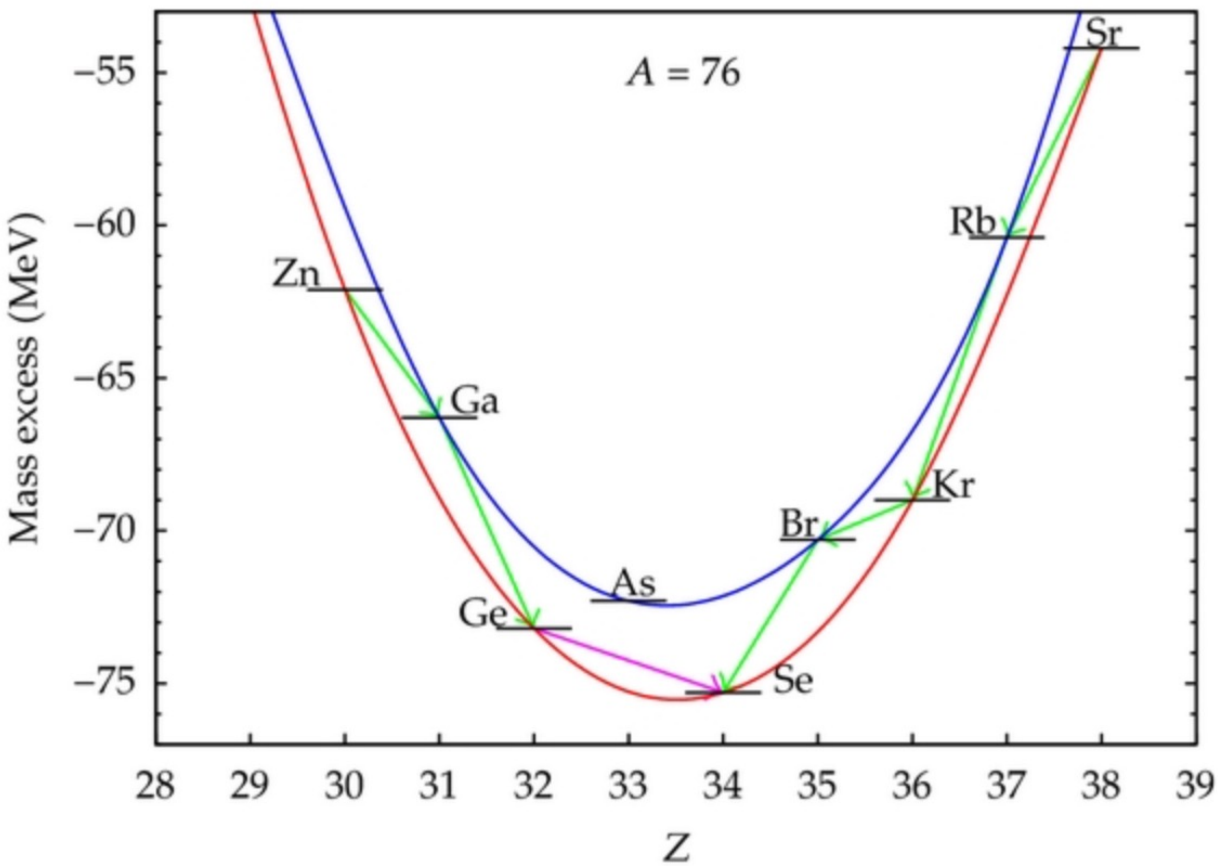

FIGURE 1.6: A mass parabola for A = 76 isobar representing allowed single β-decay by the green arrow and double β-decay by the pink arrow. The nuclei on the blue parabola have odd-odd A and Z numbers, while the orange parabola nuclei have even-even. A single β-decay is forbidden for ^{76}Ge, so the $\beta\beta$ to ^{76}Se is the only allowed decay. The diagram is adapted from J. Menendez's Ph.D. thesis.

In 1937, Giulio Racah pointed out that if neutrinos are Majorana particles, then it is possible to undergo double beta decay without emitting neutrinos [42, 43], a process known as neutrinoless double-beta decay. This is a SM-forbidden process as it violates lepton number conservation (before decay $L = 0$, after decay $L = 2$). In 1939, Wendell H. Furry calculated the approximate rate of

$0\nu\beta\beta$ [44] for the first time.

$$(A, Z) \to (A, Z + 2) + 2e^- \tag{1.13}$$

1.4.1 Modeling

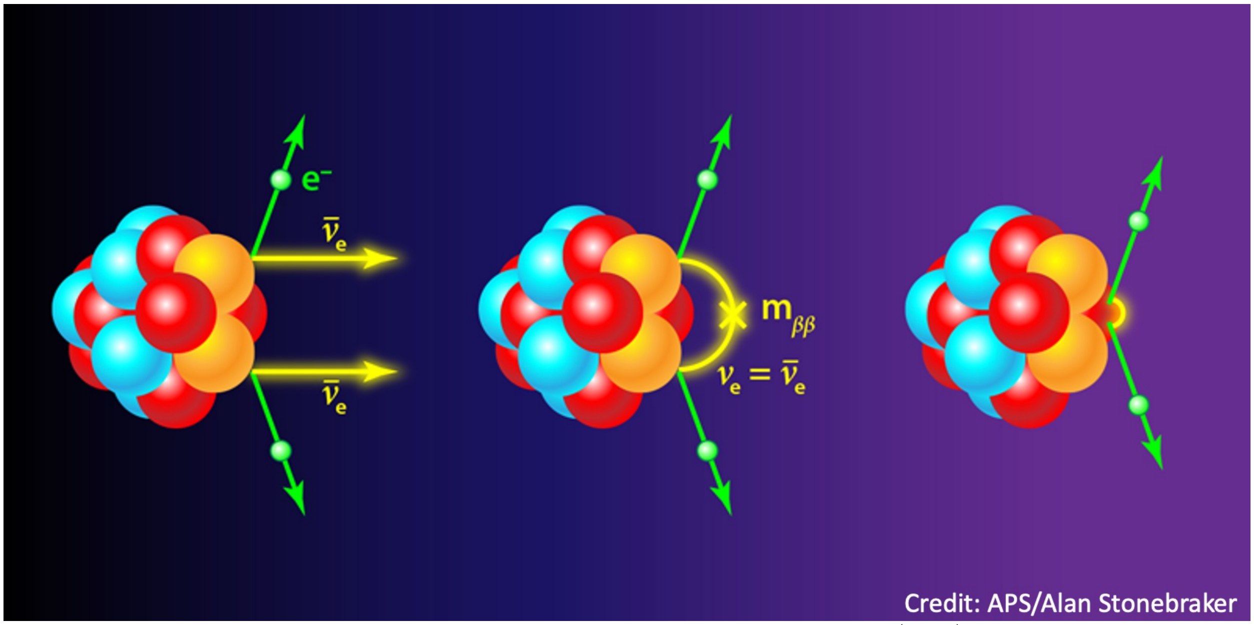

FIGURE 1.7: A depiction of three possible double-beta decay modes. (Left): $2\nu\beta\beta$ mode in which two anti-neutrinos are emitted with two electrons. (Middle): $0\nu\beta\beta$ decay mode in which no neutrinos are produced. The diagram shows $0\nu\beta\beta$ decay via light neutrino exchange, which is possible if neutrinos are Majorana particles. (Right): $0\nu\beta\beta$ decay mode via a short-range mechanism in which all exchanged particles are heavy.

Several models could potentially mediate $0\nu\beta\beta$, including the simplest one; light neutrino exchange (See [45], [46] for other models in detail). However, the observation of this decay will undoubtedly prove the neutrinos as Majorana particles in a model-independent manner. A simple depiction of light neutrino exchange and short-range mechanism are shown in Fig. 1.7.

Figure 1.8 is a Feynman diagram of the light neutrino exchange model, which is expected to be one of the dominant mechanisms for $0\nu\beta\beta$. A pair of W^- bosons exchange light neutrino mass eigenstates and produce two outgoing electrons. The whole process can be regarded to complete in two steps, where one of the light neutrino emitted together with an electron is re-absorbed at another vertex to give a second electron. The process is possible only when neutrinos are Majorana particles, *i.e* $\bar{\nu}_i = \nu_i$.

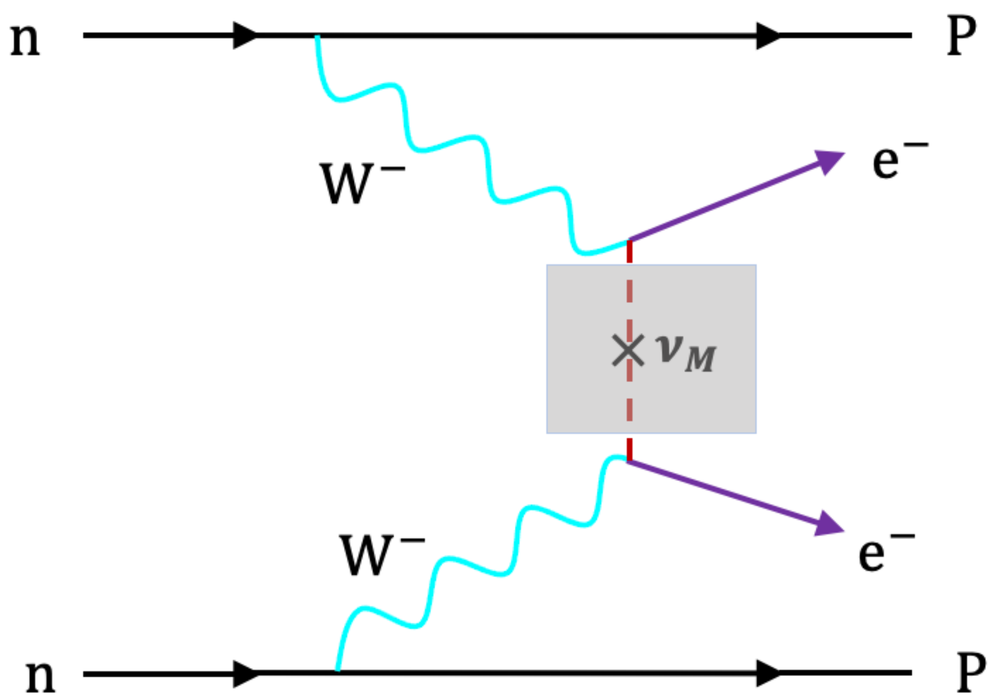

FIGURE 1.8: Feynman diagram of $0\nu\beta\beta$ via light neutrino exchange process. Two neutrons decay by emitting a pair of virtual W^- bosons, which exchange light neutrinos to produce two outgoing electrons.

The $0\nu\beta\beta$ process also generates the Majorana mass [47] referred to effective Majorana neutrino mass, and the contribution comes from all light neutrino mass eigenstates [26].

$$\langle m_{\beta\beta}\rangle = \left|\sum_i U_{ei}^2 m_i\right| \tag{1.14}$$

Here, $\langle m_{\beta\beta}\rangle$ is the effective Majorana mass of electron neutrino, m_i is the mass of mass eigenstate ν_i and U_{ei} is the component of PMNS matrix for electron neutrino flavor with Majorana CP-violating phases included as given in Eq. 1.9.

The half-life of $0\nu\beta\beta$ is related with $\langle m_{\beta\beta}\rangle$ and it can be expressed as:

$$T_{1/2}^{0\nu} = \frac{1}{G_{0\nu}(Q_{\beta\beta}, Z)|\mathcal{M}_{0\nu}|^2\langle m_{\beta\beta}\rangle^2} \tag{1.15}$$

The other terms appearing in Eq. 1.15 are described below.

- $G_{0\nu}(Q_{\beta\beta}, Z)$: It is a phase space factor that primarily depends on $Q_{\beta\beta}$. It determines the kinematics of electrons emitted from the parent nucleus. The phase-space factor can be calculated precisely using different approaches (See Review article [48] for more detail).

- $\mathcal{M}_{0\nu}$: It refers to the Nuclear Matrix Element (NME), which describes the actual decay and depends on the nuclear physics of parent and daughter nuclei. It can be expressed as:

$$\mathcal{M}_{0\nu} = \mathcal{M}_{0\nu}^{GT} - \frac{g_V^2}{g_A^2}\mathcal{M}_{0\nu}^{F} + \mathcal{M}_{0\nu}^{T} \tag{1.16}$$

  Here, g_V and g_A are vector and axial coupling strengths, $\mathcal{M}_{0\nu}^{GT}$ and $\mathcal{M}_{0\nu}^{F}$ refers to transition probabilities from Fermi and Gamow-Teller components and $\mathcal{M}_{0\nu}^{T}$ is a tensor form of NME. It is difficult to calculate the total NME without making some assumptions, especially since the exact contribution of g_A to the decay is unknown. Therefore, significant uncertainty is associated with the calculation of total NME (See the Review article [49] for the status of current and future NME calculations).

1.4.2 Experimental Requirements

In the $0\nu\beta\beta$, the transition energy (Q-value) is shared entirely by two outgoing electrons because no neutrinos are emitted. Consequently, the summed energy of two electrons is equal to the Q-value of decay, $Q_{\beta\beta}$, in the given isotope. Ideally, the summed energy spectrum would be delta function at Q-value. Conversely, the summed energy spectrum of $2\nu\beta\beta$ is continuous as in single β decay. Experimentally, other effects such as the detector's energy resolution affect peak shape in the spectrum. Therefore, a tiny peak at the tail of the $2\nu\beta\beta$ spectrum (at $Q_{\beta\beta}$), as shown in Fig. 1.9 is expected for the discovery of $0\nu\beta\beta$.

The measurement of $Q_{\beta\beta}$ of the given isotope that can undergo $0\nu\beta\beta$ can be measured precisely. Therefore, the number of signal events of $0\nu\beta\beta$ are counted based on the region of interest (ROI) around $Q_{\beta\beta}$ value. The ROI is defined based on the energy resolution of detectors. The number of signal events (N) found in the ROI is given by:

$$N = ln(2)\frac{N_A}{W}\Big(\frac{a\epsilon Mt}{T_{1/2}^{0\nu}}\Big) \tag{1.17}$$

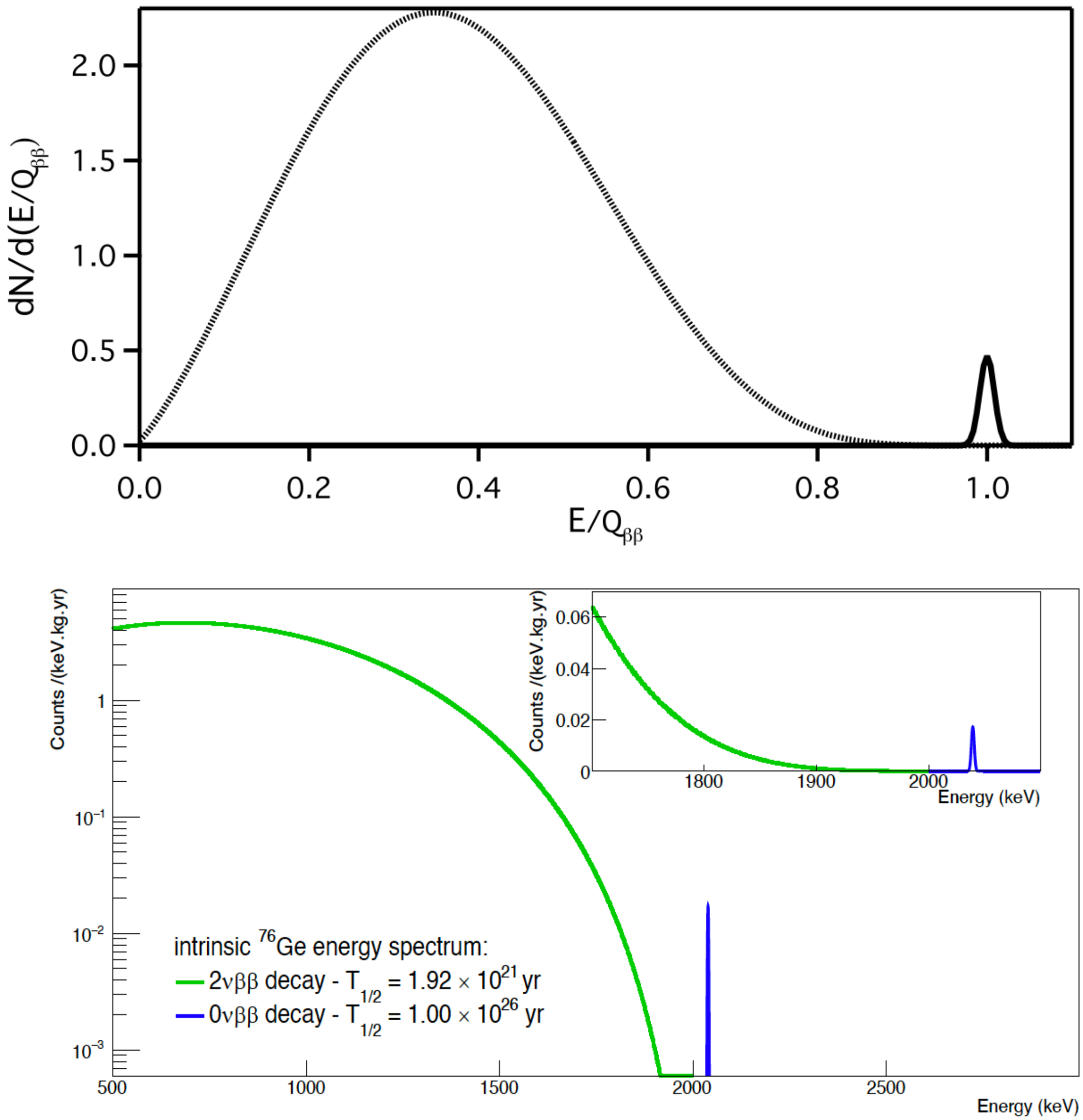

FIGURE 1.9: (Top): Summed energy distribution of two emitted electrons in double-beta decays. The dotted curve corresponds to $2\nu\beta\beta$ and the solid curve corresponds to $0\nu\beta\beta$. The curves were drawn assuming that the $0\nu\beta\beta$ rate is suppressed by a factor of 2 compared to $2\nu\beta\beta$. Also, the 1σ energy resolution of 2% was assumed. Figure is taken from Ref. [50]. (Bottom): A similar spectrum expected in ^{76}Ge assuming the given half-life values for the corresponding decays and normalized with exposure. Figure is adapted from Y. KERMAIDIC, Neutrino 2020.

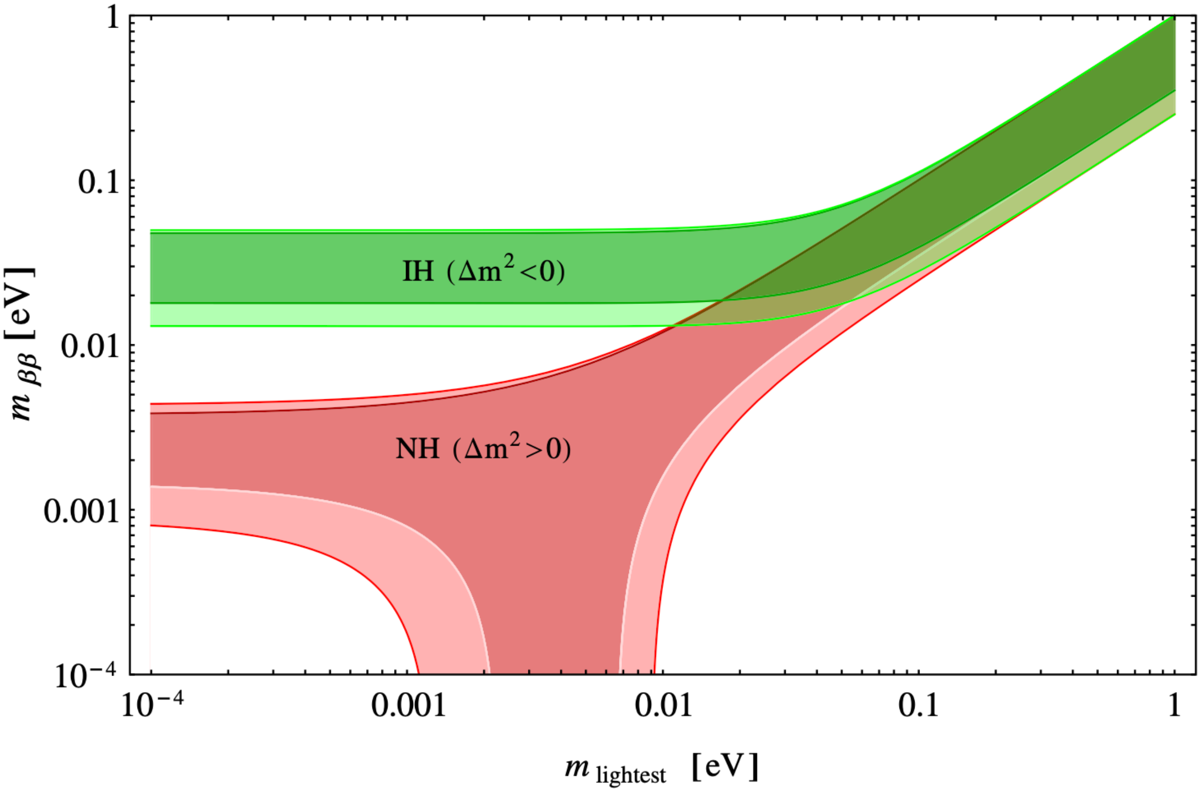

FIGURE 1.10: Allowed regions of $m_{\beta\beta}$ in the case of inverted-hierarchy (IH) and normal-hierarchy (NH) as a function lightest neutrino mass. The $m_{\beta\beta}$ value is calculated based on the parameters from neutrino oscillation experiments, and the bands refer to 3σ regions due to propagation of uncertainties in those parameters. Figure adapted from [51].

Here, N_A is Avogadro constant, W is the molar mass of the isotope, a is an isotopic abundance of the given isotope, M is an active mass of the detector, and t is the life-time. Not all observed events in the ROI might be true signal events. The above relation holds true only for a background-free experiment. The sensitivity to $T^{0\nu}_{1/2}$ for an experiment with some background index b at ROI (usually expressed in counts/(keV.kg.yr)) drops from background-free experiment as:

$$T^{0\nu}_{1/2} \propto \begin{cases} a\epsilon M t & \text{for zero background} \\ a\epsilon\sqrt{\frac{Mt}{b\Delta E}} & \text{for non-zero background} \end{cases} \tag{1.18}$$

In an experiment with background index b, an additional term ΔE, which refers to the energy resolution of the experiment at $Q_{\beta\beta}$ also suppresses the sensitivity as given in Eq. 1.18.

There are various factors to consider for the direct searches of $0\nu\beta\beta$, including isotope selection, background suppression, and detection technology. Equation 1.18 clearly demonstrates that the

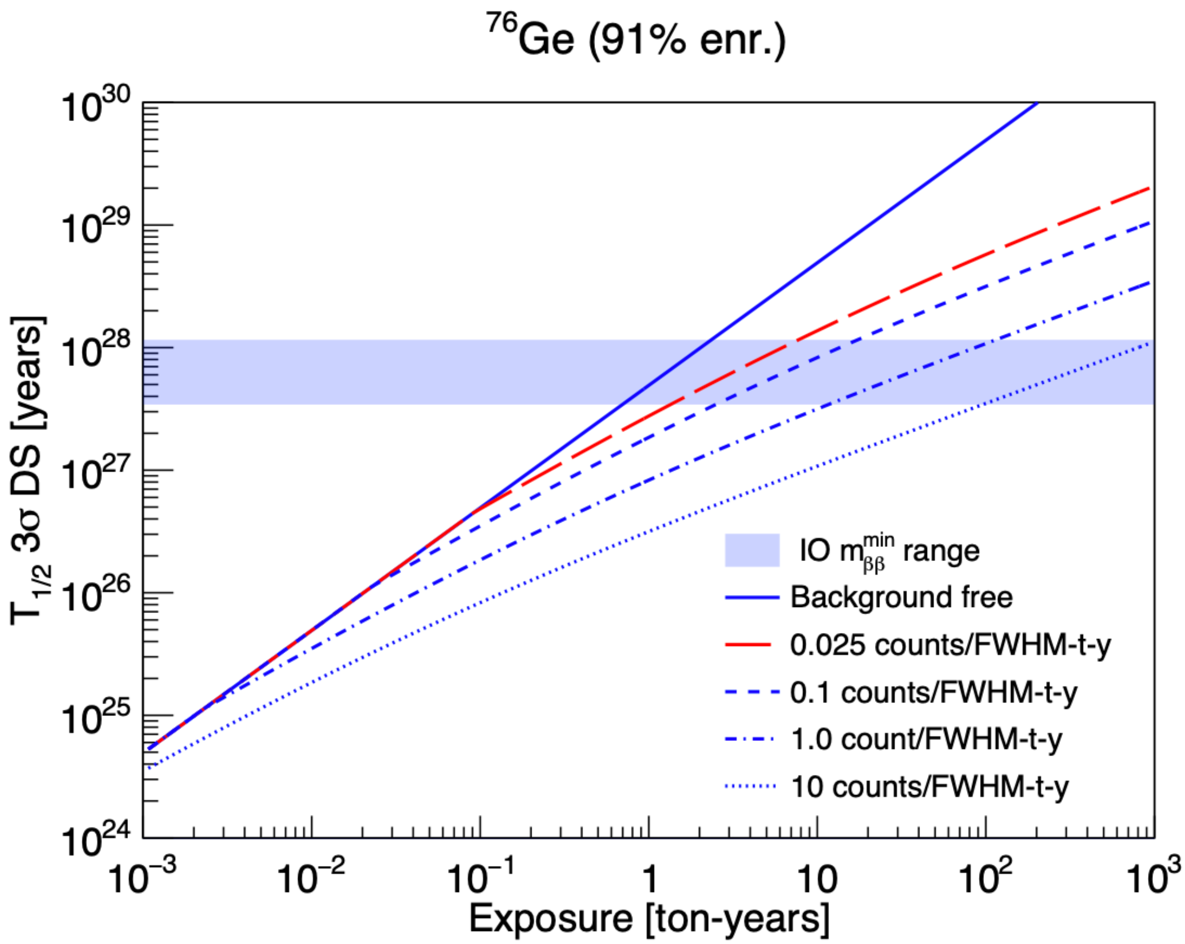

FIGURE 1.11: The Discovery sensitivity of $0\nu\beta\beta$ in ^{76}Ge as a function of exposure with different background indexes at the ROI. The band in the plot is the goal of the next-generation experiment to achieve the half-life sensitivity. The background rates are normalized to 2.5 keV Full Width at Half Maximum (FWHM). Plot is adapted from Ref. [52].

condition required for each parameter to achieve higher sensitivity. Some of the criteria for ideal experiment are described briefly below.

- Isotope Selection: An isotope with higher $Q_{\beta\beta}$, slower rate of $2\nu\beta\beta$ decay, and intrinsically radio-pure is an ideal choice. However, there does not exist an ideal isotope that satisfy all the criteria mentioned. There are about 35 isotopes reported that can undergo double-beta decay [53] among them, some isotopes currently used in the $0\nu\beta\beta$ experiments are ^{76}Ge, ^{136}Xe, ^{130}Te, ^{128}Te, ^{150}Nd,^{100}Mo etc.

- Background Suppression: Suppression of background at the ROI is one of the vitally important things for $0\nu\beta\beta$ searches. In addition to the intrinsic background in the detector materials, various other background sources exist, for example, background from nearby parts of the detector and cosmic-ray muons. Since this is an extremely rare process, an extremely stringent background index should be achieved.

- Detection Technology: The detection technology depends on the type of isotope selected. Five types of technology are adopted: semiconductors, bolometers, time projection chambers, organic scintillators, and tracking calorimeters (See Review article [54] for further details). One key feature is the detector's energy resolution, which is best achieved in a semiconductor-based experiment by the MAJORANA DEMONSTRATOR [55]. The other important thing is the discrimination ability of the experiment between signal and background events that could fall in the ROI. Therefore, an ideal experiment should be able to reject all other types of backgrounds while preserving $0\nu\beta\beta$ signal events by developing techniques; for example, one is the pulse shape analysis technique described in 2.3.

It is almost impossible to build an experiment in a background-free environment. Eq. 1.18 indicates how important it is to reduce the background and improve the energy resolution to achieve a higher sensitivity. Figure 1.10 shows allowed region of $m_{\beta\beta}$ based on the oscillation parameters for two mass ordering cases. Since $m_{\beta\beta}$ is related with half-life of the decay by Eq. 1.15, one can calculate approximately the expected value of $T^{0\nu}_{1/2}$ which is $\sim 10^{28}$ year at $m_{\beta\beta} \sim 0.01$ eV [54]. The band in Fig. 1.11 represents the half-life at 3σ discovery sensitivity for the best-case scenario of inverted mass ordering. To probe this region a tonne-scale experiment is required even in the lowest background considered as in Fig. 1.11. The next-generation experiment has a goal of probing the inverted mass ordering [52].

1.4.3 Current Status of $0\nu\beta\beta$ Measurement

As described earlier, tonne-scale experiment is required to probe the inverted mass ordering parameter space. Table 1.1 summarizes the latest results from some $0\nu\beta\beta$ experiments, where KamLAND-Zen has set the leading limit for effective neutrino mass. Many of the current generation experiments successfully finished their data-taking and moving toward the tonne-scale experiment. For example, MAJORANA DEMONSTRATOR and GERDA collaborations are jointly building a the Large Enriched

Germanium Experiment for Neutrinoless Double-Beta Decay (LEGEND) by using the best technologies of the two experiments [52].

Table 1.1: Recent results of some experiments are shown. The lower limit of $T_{1/2}^{0\nu}$ and upper limit of $m_{\beta\beta}$ are given at 90% C.L.

Experiment	$T_{1/2}^{0\nu}$ ($\times$ 10^{26} year)	$m_{\beta\beta}$ (meV)	Reference
GERDA	> 1.8	< 97-180	[56]
MAJORANA	> 0.83	< 113-269	[57]
CUPID-0 (^{82}Se)	> 0.046	< 263-545	[58]
KamLAND-Zen	> 1.07	< 61-165	[59]
CUORE	> 0.17	< 75-350	[60]
EXO-200	> 0.35	< 78-239	[61]
NEMO-3 (^{82}Se)	> 0.0025	< 1200-3000	[62]

1.5 Summary

Neutrinos are the yet least understood particles in the Standard Model. The observation of neutrino oscillation confirmed that they have non-zero mass, unlike predicted in Standard Model. Furthermore, the mass mechanism and the particle's nature, whether Majorana or Dirac, are unknown. Neutrinoless double-beta decay is a most compelling test for the Majorana nature of neutrinos. There are various models to explain how this process could occur, all beyond the Standard Model, where the light neutrino exchange model is one of the dominant. However, if this decay is observed, an observed symmetry in Standard Model (lepton number conservation) would be violated in a model-independent manner and also provide the neutrino's mass. The violation of the lepton number has fundamental implications in particle physics. It could answer the mystery behind matter-antimatter asymmetry in the universe through a process called leptogenesis.

The observation of $0\nu\beta\beta$ is, however, very challenging as it is an extremely rare process. Some of the critical parameters for the experimental requirements include tonne-scale exposure, minimum possible background environment, and excellent energy resolution of the detectors. However, before building a tonne-scale experiment, the feasibility of achieving those parameters has to be demonstrated with a middle-scale experiment. Chapter 2 will explain one such experiment called Majorana Demonstrator, which has achieved the best-in-field energy resolution. The rest of the chapters describe multiple works, all based on the calibration data. Chapter 3 describes the energy calibration and systematic of the Majorana Demonstrator. Radiogenic neutrons from (alpha,n) reaction could be one potential source for the next-generation experiment. Chapter 4 and Chapter 5 discusses radiogenic (alpha,n) reactions and validation of TALYS-generated (alpha,n) cross-sections. Chapter 6 will describe the machine learning approach to discriminating signal and background.

2

Overview of the MAJORANA DEMONSTRATOR

The MAJORANA DEMONSTRATOR is a neutrinoless double-beta decay experiment operating at 4850-foot level underground at Sanford Underground Research Facility (SURF) in Lead, South Dakota [63]. The data-taking for the $0\nu\beta\beta$ search was completed in March 2021, and it continues taking data for other physics and background studies. The next-generation experiment aims to achieve a half-life discovery sensitivity of $\sim 10^{28}$ yr and beyond, which corresponds to the effective neutrino mass, $m_{\beta\beta}$ of $\sim$15 meV. The experiment capable of achieving this $m_{\beta\beta}$ sensitivity will probe the inverted mass ordering parameter space [64]. To achieve this sensitivity, a tonne-scale experiment with extremely good energy resolution and ultra-low background at a level of $\sim$ 0.1 count/(FWHM t yr) is required. Before building a tonne-scale experiment, it is crucial to develop technologies to achieve low background, excellent energy resolution, and detector operating techniques to be scaled up to future tonne-scale experiments. With these requirements under consideration, the MAJORANA DEMONSTRATOR experiment was built.

The MAJORANA DEMONSTRATOR is primarily searching for $0\nu\beta\beta$ in ^{76}Ge and sets the competitive limits on half-life sensitivity and effective neutrino mass. The latest result with the full dataset will be described in Sec. 2.4. In addition to the $0\nu\beta\beta$ search, the MAJORANA DEMONSTRATOR is able to probe some other BSM physics [65–69]. The wide range of physics analyses results from the low background, low analysis energy threshold, and superior energy resolution achieved in the MAJORANA DEMONSTRATOR.

This chapter will provide an overview of the experimental design and pulse-shape analysis techniques to reduce the backgrounds, and the latest $0\nu\beta\beta$ results.

2.1 Experimental Design

High Purity Germanium (HPGe) detectors with P-type Point Contact (PPC) geometry are used in the Majorana Demonstrator. The PPC geometry exhibits excellent energy resolution and allows robust pulse shape analysis over other geometries. It utilized 29.7 kg of enriched and 14.4 kg of natural germanium detectors, with a mass range $\sim$(0.5-1.1) kg, during its data-taking campaign from 2015 to 2021. Those detectors were divided into two modules, as shown in Fig. 2.3. The enriched detectors were enriched to 87% to ^{76}Ge, where 7% comes from the natural abundances. These enriched detectors are both source and detector for $0\nu\beta\beta$ searches, while the natural detectors are used to study background and some other physics. Additionally, the Majorana Demonstrator operated 6.7 kg Inverted Coaxial Point Contact (ICPC) enriched germanium in the final run configuration of the $0\nu\beta\beta$ search (DS8 data set). Those ICPC detectors were manufactured for LEGEND and also used in the Majorana Demonstrator for low background vacuum testing.

The experiment was built using ultra-clean materials. The materials were selected based on an extensive radioassay campaign [70]. The nearby components of the detector, for example, detector holders, cables, and connectors, were built with underground grown electroformed copper (UGEFCu). The experiment had a facility to fabricate UGEFCu at the 4850-foot level of SURF by electroforming. The copper was selected to make the components of the detector due to its higher mechanical strength and low radioactivity. UGEFCu is the purest form of copper ever produced [71]. The detector components were built in the underground machine shop with UGEFCu. The Demonstrator also focused on the low-mass design of the components, including front-end electronics, called LMFE [72]. Figure 2.1 shows the photos of the electroforming copper bath, some nearby components, and a detector unit. The detector units were installed in a modular array. A module refers to a cryostat and outer hardware components, for example, vacuum and cryogenics. The Demonstrator had two modules, each containing a cryostat and external hardware. A cryostat contains strings of detectors. The main advantage of the modular approach was that they run independently of each other so that data-taking was continuous from one module while installation or upgrades were done on the other. Figure 2.2 on the left is a photo during the installation of the detectors into the strings, and the right photo is before a module was moved into the main shield.

FIGURE 2.1: (Left): Underground electroforming for the fabrication of purest copper. (Middle): Detector nearby components made with UGEFCu. (Right): A detector unit with a LMFE board on top.

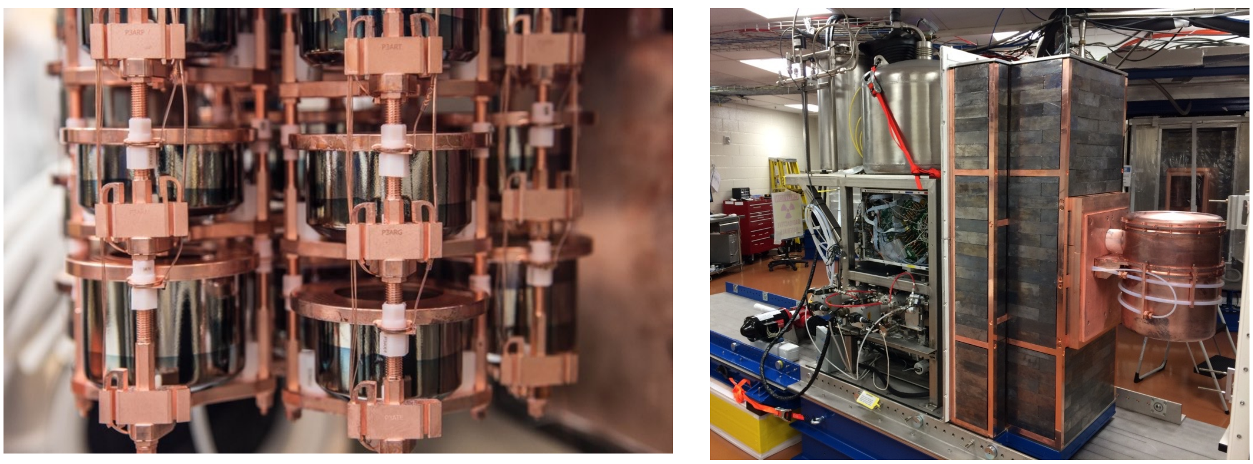

FIGURE 2.2: (Left): An array of detector units. (Right): A cryostat with a lead shield ready to be installed in the main shield.

The detectors were operated inside multiple layers of active and passive shielding in a class-1000 clean room environment at 4850-foot level of SURF. Figure 2.3 is the cross-sectional view of the Majorana Demonstrator. Each shielding layer is cleaner as it reaches closer to the center of the experiment where the detectors are installed. These shielding layers are briefly described below in order, with the outermost at first.

- Poly Shield: It has a thickness of 12-inches and consists of high-density polyethylene and borated polyethylene. The purpose of the layer is to moderate the environmental neutrons in the lab and is referred to as passive shielding.

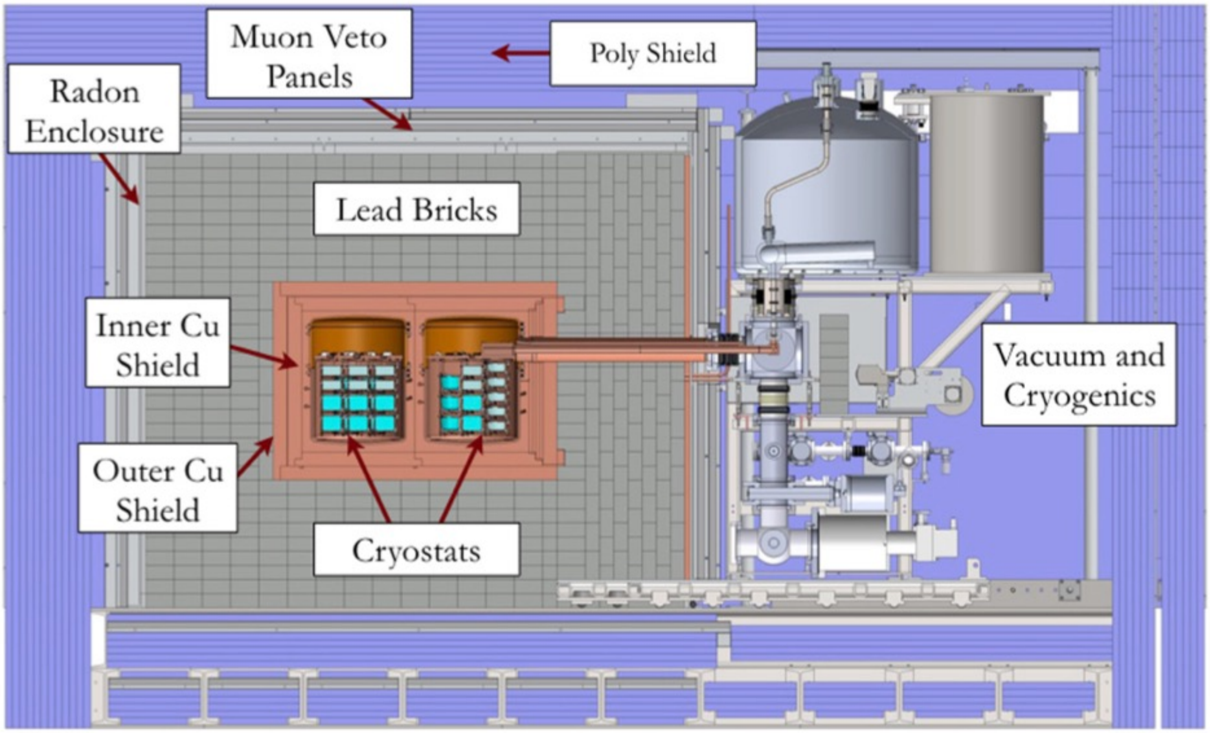

FIGURE 2.3: The diagram for the cross-sectional view of the MAJORANA DEMONSTRATOR. Detectors are divided into two modules, which are surrounded by passive and active shielding layers. Each module has its own vacuum and cryogenic systems. Diagram adapted from [65].

- Muon Veto Panels: This layer consists of a total of 32 muon veto panels that surround the inner layers from all directions. The bottom has 12 panels and each other remaining sides has 4 panels [73]. These panels are plastic scintillators used to tag the muons passing through the detectors. Any germanium events that are in coincidence with muons are removed from the analysis.

- Radon Enclosure: In an underground experiment, radon gas is one of the potential problems. ^{222}Rn and its progeny produce high energy α-particles, which could contribute to the background. The radon enclosure is aluminum box in which the normal air that might have radon gas is purged continuously by dry nitrogen gas.

- Lead Bricks: A 45cm-thick layer of lead bricks shields environmental γ-rays.

- Outer Cu Shield: It is a 5cm thick rectangular box made of pure commercial copper.

- Inner Cu Shield: It is the last and purest shielding layer made of UGEFCu and has 5cm thickness.

Finally, the detector modules sit at the heart of all these layers of shielding. These shielding layers and the use of detector components with ultra-pure materials helped reduce the background and demonstrated the scalability of this technology for the tonne-scale experiment.

2.2 Detector Signal

The cross-sectional view of a PPC detector unit used by the MAJORANA DEMONSTRATOR is shown in Figure 2.4. It has an outer n^+ contact created by lithium diffusion while a small p^+ contact is created by boron implantation. A dead layer with thickness ~1 mm is formed at the surface of the detector by the lithium diffusion process. However, there is no definite separation of the dead layer from the active bulk region. This is because the concentration of lithium ions drops from the dead layer's outer surface to its inner surface. Therefore, there exist two regions within the dead layer; the first region where charge collection efficiency is zero and the second where charge collection efficiency is non-zero [74]. The second region is called the transition region. The passivated surface is the region about 1μm thick which is created by amorphous germanium to separate the p^+ and n^+ contacts.

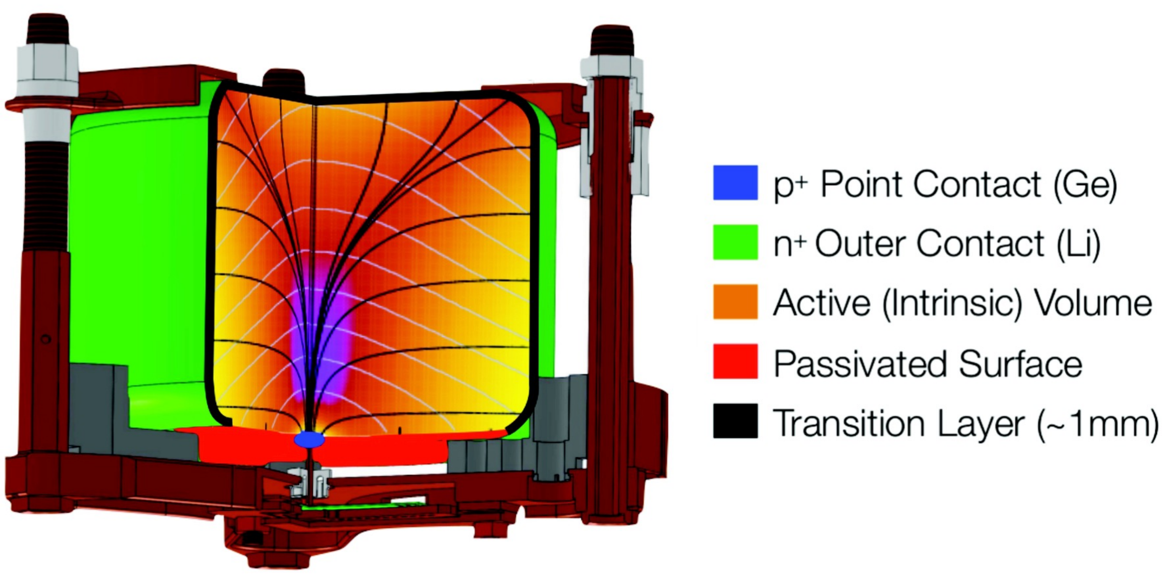

FIGURE 2.4: Cross-sectional view of a detector unit with its internal weighting potential, hole drift path (black), and loci of equal drift time (grey). Weighting potential is localized near the point contact and very low elsewhere.

In semiconductors, electron-hole pairs are created by the excitation of an electron from the valence band to the conduction band. The excitation of an electron occurs when sufficient energy is provided. For example, in germanium, one electron-hole pair is produced for every 0.7 eV energy deposition. Therefore, the induced charge signal is a measure of the initial energy deposited in the detector.

Electron-hole pairs are produced when more than 0.7 eV energy is deposited inside the detector. Energy might be deposited by external radiation or internal decays. The electrons and holes are then drifted towards n^+ and p^+ contact under the application of reverse bias voltage. The typical depletion voltage varies from 1-5 kV for the MAJORANA PPC detectors. Due to the motion of the charge carrier, current is induced at the contacts. The induced charge from such current at p^+ contact is collected by low-mass front end board (LMFE) [75]. A LMFE is a charge-sensitive preamplifier that is mounted on each detector at 1cm from the point contact. One end of a LMFE is electrically connected with the p^+ contact and the other with a second stage amplifier that sits outside the shield layer. To reduce the background from the electronics, only the LMFEs reside inside the shield layer. The second stage amplifier produces two signals differing in gain. Finally, two digitized charge signals are recorded from each interaction in the detector. Chapter 3 describes digital signal processing and energy determination in detail from these digitized charge signals. The MAJORANA electronics and readout system is describe in detail in Ref. [72].

2.3 MAJORANA Approach to Backgrounds

First of all, the detectors used by the MAJORANA DEMONSTRATOR are intrinsically very pure and were provided by two vendors. The natural detectors were manufactured by MIRION/CANBERRA [1] and the enriched were manufactured by AMETEK/ORTEC [2]. The dedicated method of enrichment, zone-refining, and crystal growth removes the radioactive impurities present inside the detector. Furthermore, to reduce cosmogenic activation, they were transported with additional shielding with a minimum time exposed above the ground after they were manufactured.

Muon-induced backgrounds are a key concern for a low-background experiment [76]. The exper-

[1] https://www.mirion.com

[2] https://www.ortec-online.com

iment runs at 4850-foot feet below the surface equivalent to a rock overburden of $\sim$ 4300 m.w.e [63] to attenuate muons and minimize muon-induced backgrounds. A muon-veto cut is developed by the collaboration to remove muons-related events with very high efficiency ($>$ 99.9%).

In addition, the experiment was built with extremely pure materials in a heavily shielded environment, as discussed in Sec. 2.1 to reduce external backgrounds from outside of the shield and internal backgrounds from the detector materials. Furthermore, the modular array form helped to develop a granularity cut to remove the events that occur in multiple detectors. An event that deposits energy in multiple detectors is a background for $0\nu\beta\beta$ search.

In addition to the above approach, the MAJORANA collaboration developed various pulse-shape-based analysis cuts to remove various types of backgrounds. Those analysis cuts are briefly described in the following subsections.

2.3.1 Multi-Site Event Rejections

The PPC detector technology provides robust pulse shape analysis (PSA) techniques. The weighting potential is strong in the vicinity of point contact and low elsewhere throughout the detector, due to which induced charge is collected during a short period during its arrival at the electrodes. Therefore, the rise time of the waveform is much shorter than the drift time of the charge carrier and carries information on whether the interaction occurred in multiple locations within the detector or in a single location. If the current pulse of the charge waveform is measured, the multi-site interaction has multiple peaks, while the single-site has a single peak. The current pulse amplitude (A) is smaller in multi-site interaction than in single-site interaction for the same initial interaction energy (E), as seen in Fig. 2.5. In neutrinoless double-beta decay, the energy released is carried out by two electrons which deposit energy within a short distance and produce single-site interaction. Therefore, single-site events are signal-like, while multi-site events are backgrounds.

A multi-site cut, AvsE, is developed [77] to remove multi-site events. The cut is tuned and the cut efficiency is estimated based on the calibration data. The double escape peak (DEP) and single escape peak (SEP) events are inherently single-site and multi-site events. These events are produced as a result of pair production of a 2615-keV γ-ray interaction in the detectors. When a 2614-keV γ-ray interacts with a germanium detector, an electron-positron pair is produced, which then annihilates and produces two 511-keV γ-rays. If both γ-rays escape from the detector, a single energy deposition occurs at 1593 keV, which refers to a DEP peak. Similarly, if only one 511-keV γ escapes from the detector, energy will be deposited in two locations totaling 2103 keV, which is refered to as a SEP peak. Hence, SEP events are backgrounds and DEP events are signal-like events. The recommended cut of multi-site event discriminator, $avse\_corr < -1$, is tuned to accept 90% single-site events. The AvsE cut reduces the Compton continuum background by 50% and suppresses events in the background estimation window by a factor of three [77].

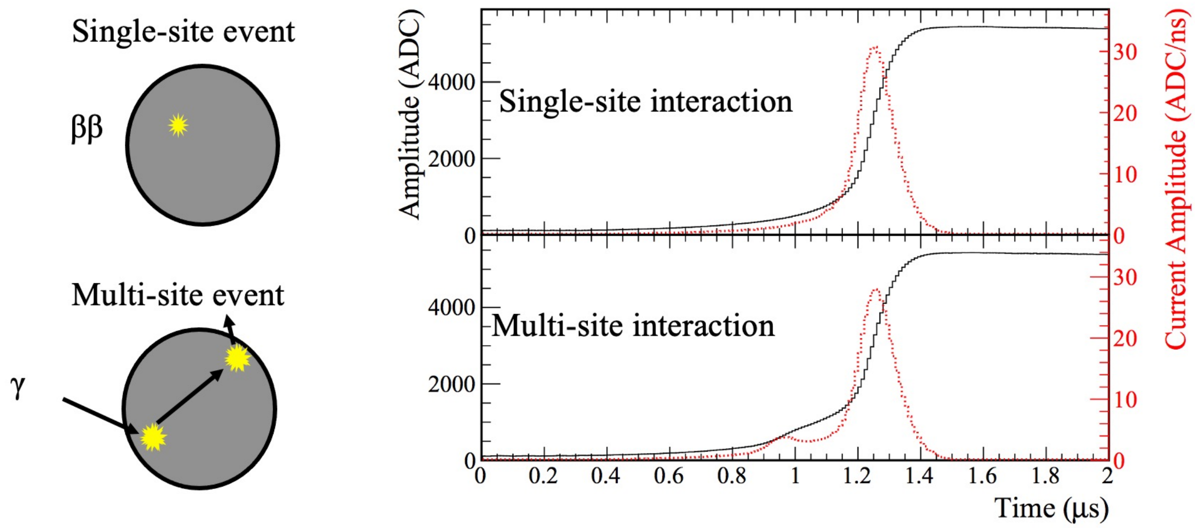

FIGURE 2.5: (Left): Schematic of single-site and multi-site interaction. $\beta\beta$ events are inherently single-site, and Compton scattering of external γ events are multi-site interactions. (Right) Charge waveforms (black) and corresponding current pulse (red) of single-site and multi-site events. Figure is adapted from [77]

2.3.2 Surface Alpha Rejection

High energy α-particles, a potential source from ^{222}Rn-progeny, may be incident at the detector surface. Most of the outer surface of a detector is a dead layer, where signals from the interaction can not penetrate the dead layer, and not a problem. However, an α-particle may be incident at the passivated surface and produce signals, which are highly degraded in energy. The signals with degraded energy can fall in the $0\nu\beta\beta$ ROI. The induced charge from such interaction can be trapped and slowly re-released, resulting in a waveform tail with a positive slope called Delayed Charge Recovery (DCR), as shown in Fig. 2.6. To remove such events, a DCR parameter is developed. The cut parameter $dcr\_corr < 2.326$ is used to remove the surface α-events while retaining 99% signal events. The recommended cut of the DCR discriminator removes the background at ROI by one order of magnitude [78].

An α-particle interaction near the point contact could, however, cause a sharp rise in the waveform resulting in a fast charge collection. Such waveform have high `AvsE` value and are removed by implementing a higher value of `AvsE`.

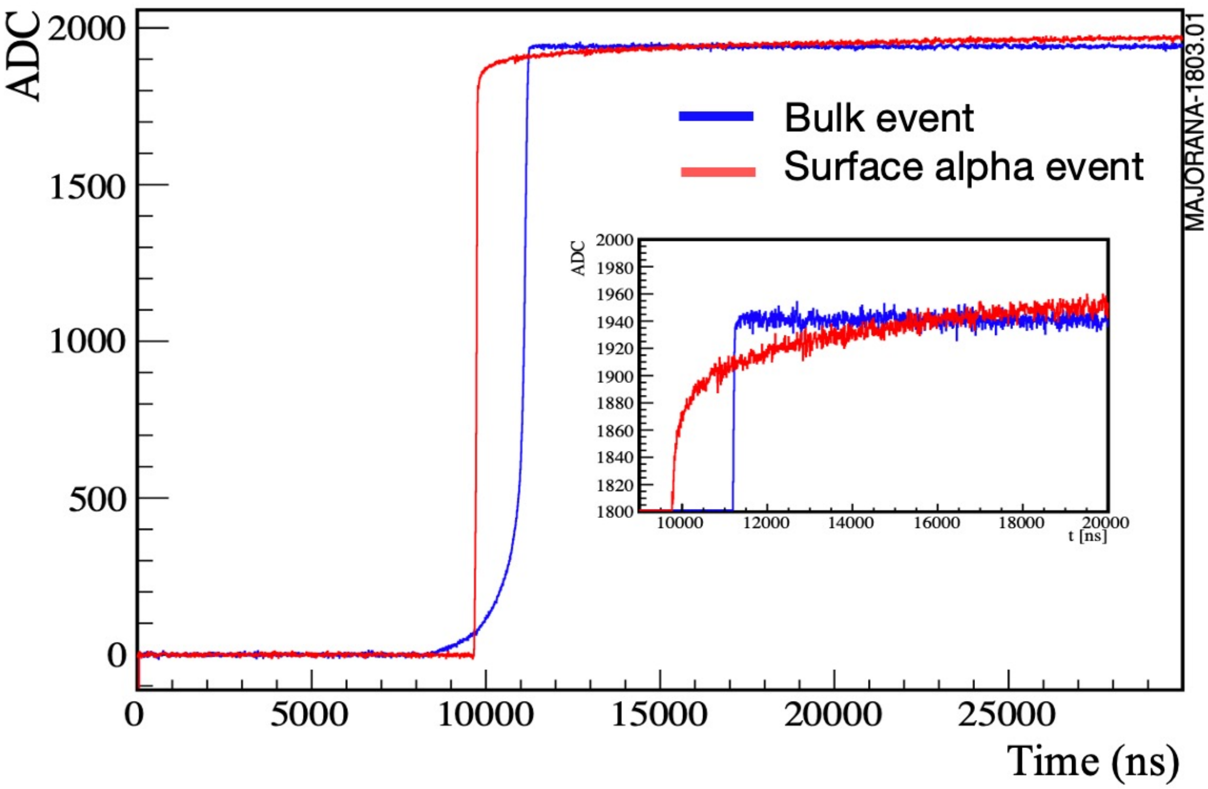

FIGURE 2.6: An example of a waveform for an interaction in the bulk of the detector(blue) and α event incident at the passivated surface (red). The waveform tail of the surface alpha interaction has a positive slope called DCR.

2.3.3 Late Charge Event Rejection

Some typical types of multi-site events, if their one site of interaction is near the point contact, might pass the regular AvsE cut. Such events are removed by applying a new cut called LQ 2.7. The recommended cut for such event discriminator is $LQ < 10$, which retains 99.9% single-site events [57].

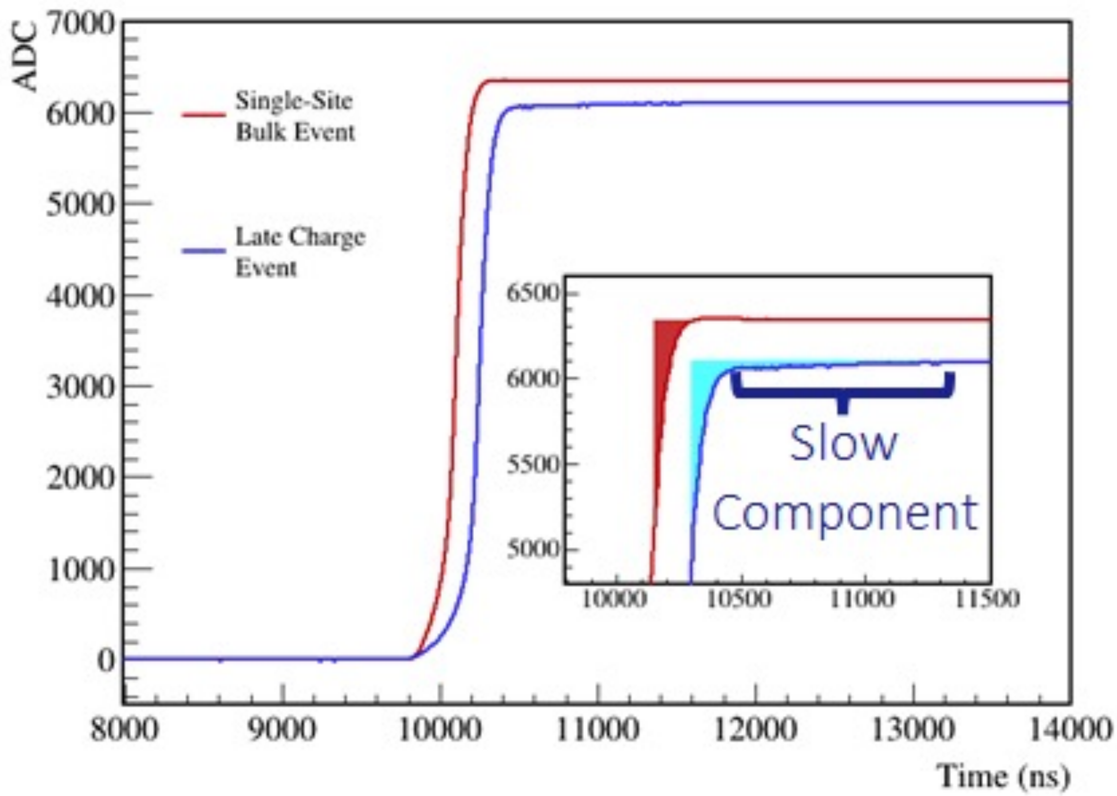

FIGURE 2.7: A waveform with the slow component (blue) and without (red). The highlighted region is the area based on which the LQ parameter is calculated.

2.4 MAJORANA Results and Summary

The MAJORANA DEMONSTRATOR started data-taking with one module in 2015 and both modules in 2016. The changes in detector configurations over time are shown in Fig. 2.8. The exposure from enriched and natural detector data-taking over time is shown in Fig. 2.9. The MAJORANA DEMONSTRATOR has published two results regarding the $0\nu\beta\beta$ searches. The first result was published with $\sim$10 kg-yr of enriched Ge exposure [79] and the second result with $\sim$26 kg-yr of enriched Ge exposure [55].

The final result with 64.5 kg-yr exposure has been released recently [57]. Figure 2.10 is the energy spectrum from total exposure. The MAJORANA DEMONSTRATOR measured $15.3^{+1.4}_{-1.3}$ cts/(FWHM t y), which is higher than assay-based projections [70]. However, a careful investigation, which will be published soon, shows that excess background is not from the nearby components of the detectors.

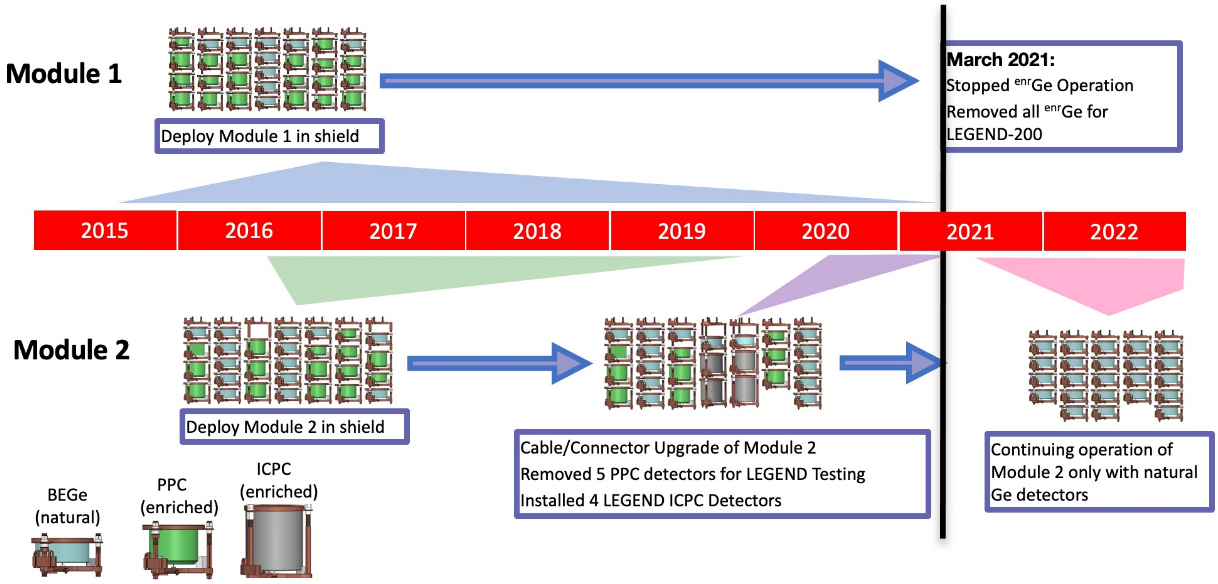

FIGURE 2.8: Schematic of MAJORANA DEMONSTRATOR run configuration and timeline since 2015.

The MAJORANA DEMONSTRATOR final result sets a lower limit of $0\nu\beta\beta$ in ^{76}Ge to be 8.3×10^{25} yr (90% C.L.), and an upper limit of effective neutrino mass to be (113-269) meV (90% C.L.)

The MAJORANA DEMONSTRATOR was not limited only for $0\nu\beta\beta$ searches in ^{76}Ge. The excellent energy resolution, low energy threshold, and low background achieved in the DEMONSTRATOR resulted in a wide-range of physics program. The DEMONSTRATOR probed variety of physics including Standard Model physics [80, 81], exotic physics [66, 82], tests of fundamental symmetries and conservation [67, 68, 83], and some additional BSM physics [67, 84, 85].

The MAJORANA DEMONSTRATOR and GERDA [56] are the most sensitive germanium-based experiments for $0\nu\beta\beta$ search. These experiments adapted different techniques for background suppression and concluded their data-taking. The two collaborations are combined to form the LEGEND collaboration, a next-generation tonne-scale germanium-based experiment. The best of the two experiments will be adapted for LEGEND. For example, MAJORANA demonstrated the technology to use extremely pure nearby components and low-noise electronics, while GERDA demonstrated low background by using active liquid argon veto and low-mass shielding without the use of lead. These proven technologies are key assets for LEGEND [52].

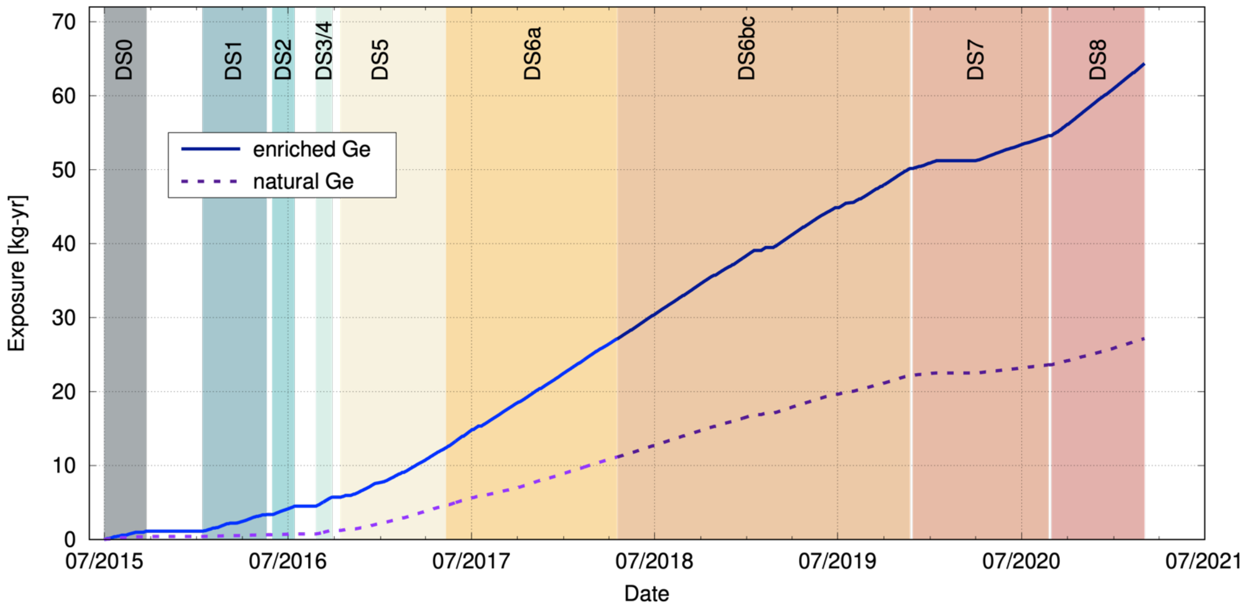

FIGURE 2.9: Cumulative exposure of data-taking with enriched and natural detectors over time. The enriched data-taking is completed with 64.5 kg-yr exposure from enriched detectors. The data is divided into data sets DS0 through DS8 based on the detector configurations, as shown in Fig. 2.8 and slight changes in the DAQ system.

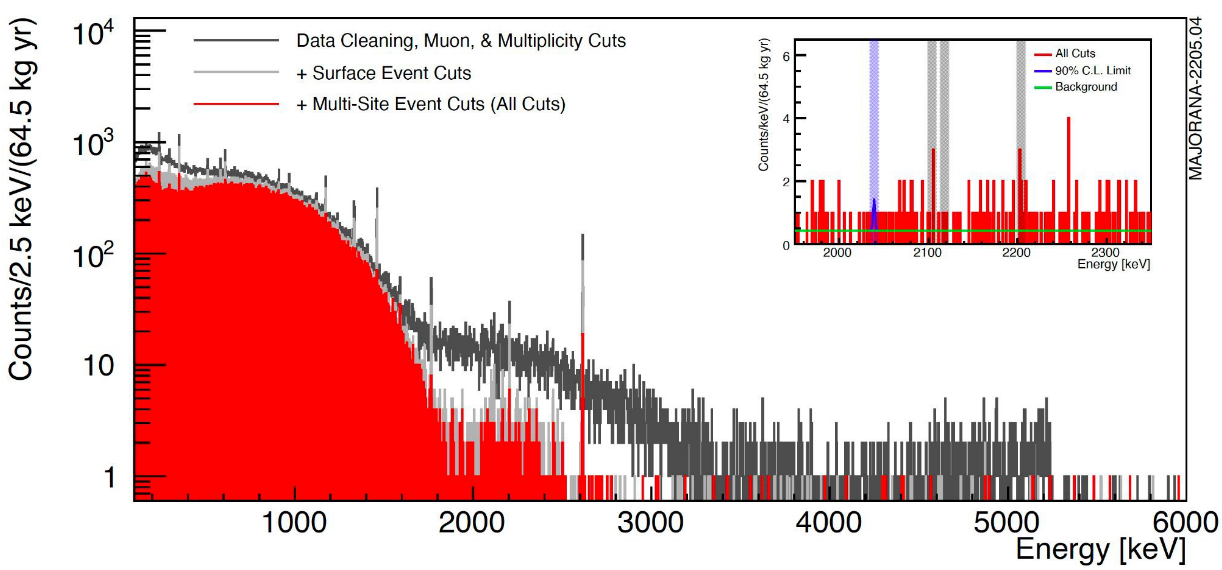

FIGURE 2.10: Energy spectrum above 100 keV for all data sets with only data cleaning and muon veto applied (black), after applying the background cuts targeted at surface events, such as DCR, high AvsE, and LQ (gray), as well as multi-site cut, low AvsE (red). The inset shows the 400 keV region used to compute the background index; the gray regions contain known gamma peaks, and the shaded blue region is the 10 keV region around $Q_{\beta\beta}$ for setting the half-life limit [57].

3

Energy Determination in the Majorana Demonstrator Experiment

Energy resolution is a critical parameter that affects the sensitivity to the half-life, $T_{1/2}^{0\nu}$, of $0\nu\beta\beta$ experiments. A smaller energy resolution value provides a higher half-life sensitivity and better rejection of $2\nu\beta\beta$-decay backgrounds. The excellent energy resolution is the result of detector selection as well as energy calibration. Majorana Demonstrator experiment has achieved the best energy resolution among all current-generation $0\nu\beta\beta$ experiments. This chapter will discuss the mechanism of raw energy extraction, energy calibration, and systematic study in the Majorana Demonstrator.

3.1 Raw Energy Estimation

In Majorana Demonstrator, each signal from a detector is amplified to produce two outputs which differ in gain by a factor of ~ 3 so-called low-gain and high-gain outputs. The outputs are then digitized by using GRETINA digitizer modules [86] with a sampling frequency of 100 MHz with 14 bits of precision and records 2020 samples per waveform. A typical digitized raw waveform is shown in Fig. 3.1. The digitized raw waveforms are then subjected to trapezoidal filters to estimate the corresponding raw offline energy. However, two effects have been considered and applied to improve the energy estimation prior to the application of trapezoidal filters.

3.1.1 ADC Nonlinearity Correction

Periodic non-linearity present in the digitizer modules may cause the deviation in energy estimation up to 0.8 keV in high-gain and 2.8 keV in low-gain channels near the $Q_{\beta\beta}$. Such deviations, if not corrected, degrade the energy resolution and affect the aspect of pulse shape analysis. Therefore, non-linearity is measured in each digitizer channel, and correction is applied to the digitized waveforms prior to further signal processing [87].

The non-linearity in each digitizer channel is measured using two external signal generators. The slow ramp signal with a higher amplitude covers the entire ADC range, while the fast ramp with a lower amplitude modulates the signal from the slower ramp. Figure 3.2 shows the measured non-linearity in one of the digitizer channel in the DEMONSTRATOR. The measured non-linearities are used to correct each waveform sample with 10 ns sampling period.

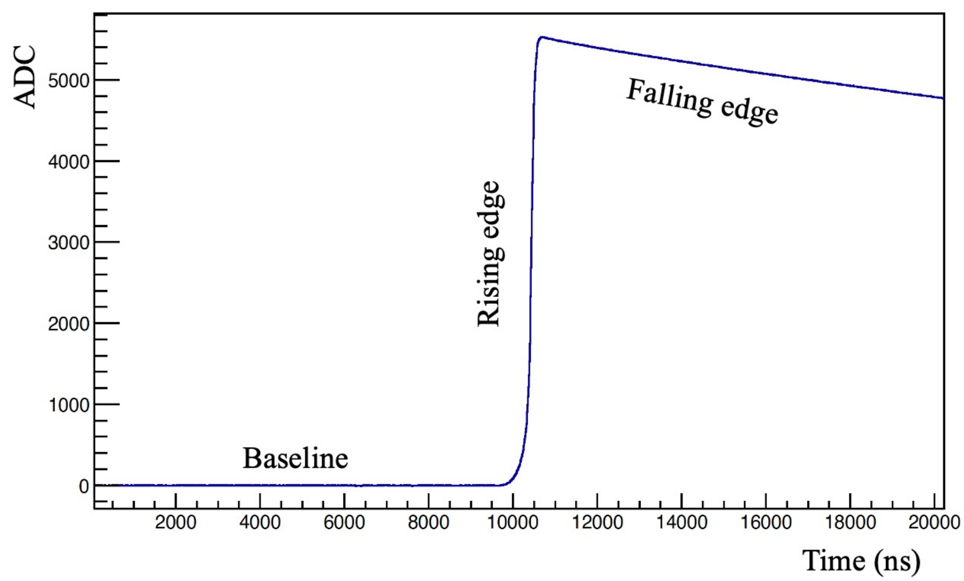

FIGURE 3.1: A typical digitized raw waveform shaped by signal electronics. The waveform baseline is the electronic response prior to the collection of charge. The sharp rising edge is the period during which the charge drifts near the point contact of the detector. The exponential falling edge is due to the discharge of the capacitor in the preamplifier through the resistance feedback network. The DEMONSTRATOR uses the preamplifier with the decay constant of ≈ 72 μs.

3.1.2 Charge Trapping Correction

Charge trapping is the phenomenon in which charge carriers are trapped and released by the local impurities present in the detector as they drift towards the charge collection electrodes. In the case of PPC detectors, charge collection due to the drift of holes is reduced near the point contact; consequently, the height of the waveform is reduced. The loss of charge causes attenuation in recorded energy, produces the low-energy tail in the γ-peak shape, and degrades the energy resolution. This effect is linearly related to the drift time of the charge carriers, which is dependent on the initial location of the charge carriers produced. A slower signal is attenuated to a greater extent than the fast signal waveform.

The exponential decay tail of the waveform shown in Fig. 3.1 is mainly due to the signal shaping by the preamplifier. In the pulse-height analysis, this tail can be corrected by applying a pole-zero correction [88]. Such correction would flatten the exponentially decaying tail of the non-linearity corrected waveforms with a different extent of charge trapping effect as shown in Fig 3.3 to the left plot of Fig. 3.4. The pulse amplitude can be extracted, which would be the uncalibrated energy that

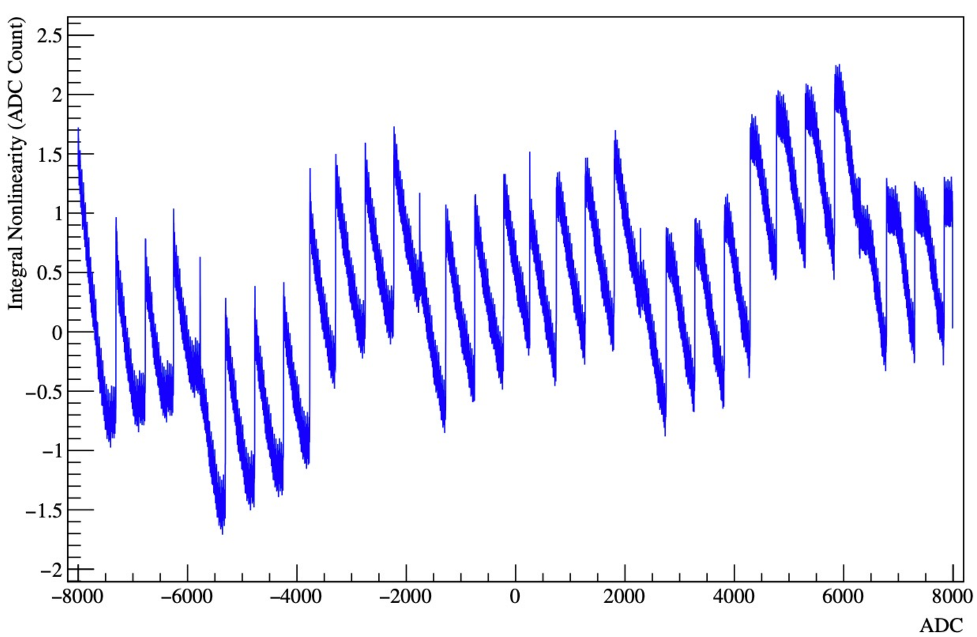

FIGURE 3.2: An example of measured non-linearity in a digitizer. The zig-zag patterns show the deviation due to non-linearity at each ADC bin. The X-axis is the ADC channel due to the scan of the slow ramp, and Y-axis is the deviation measured by the fast ramp at a given ADC channel referred to as integral non-linearity. Plot adapted from [55].

is proportional to the initial energy of the interaction. However, the pulse height might differ for waveforms generated by the same initial interaction energy due to charge trapping. For example, a signal with a longer drift time would experience more charge trapping, which reduces its pulse height.

The exponential loss of charge carriers along the drift path due to the effect of charge trapping from the initial charge amplitude, Q_0, can be described by:

$$Q(t) = Q_0 e^{-\frac{t}{\tau}} \tag{3.1}$$

Where τ is the effective pole-zero time constant. The charge trapping effect affects the rising edge

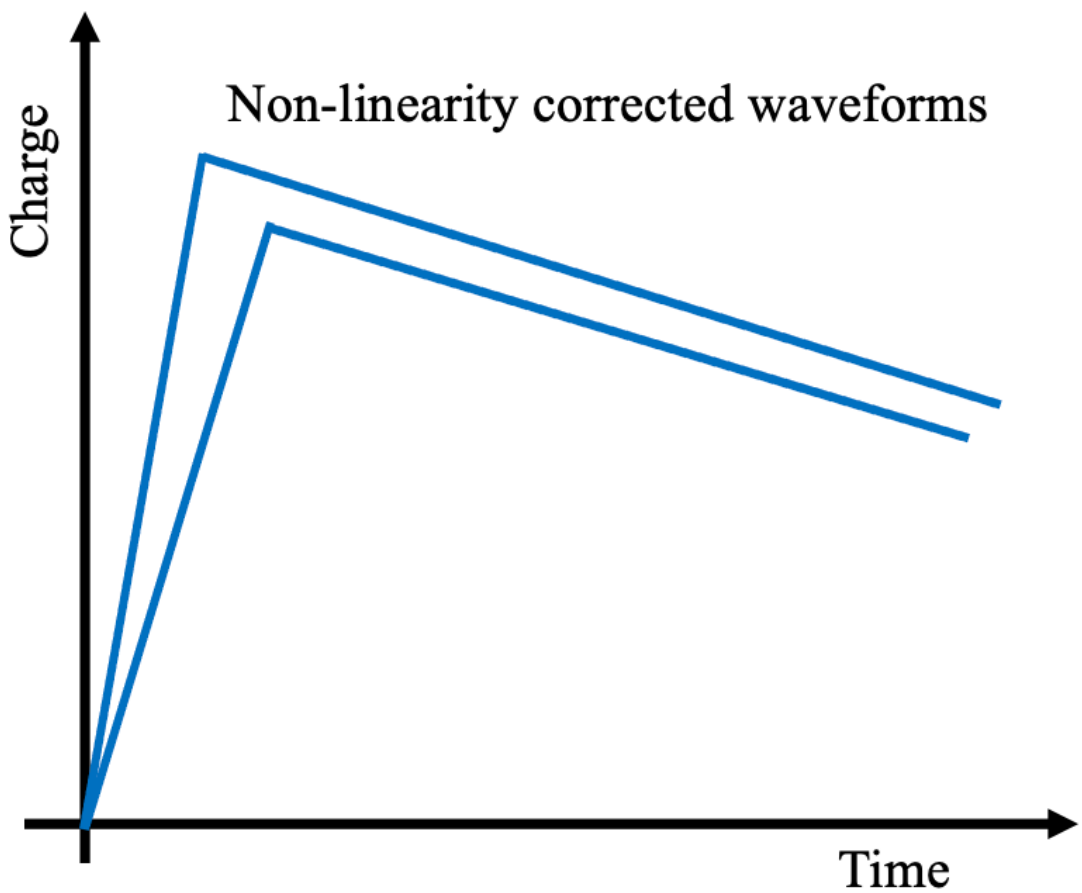

FIGURE 3.3: A schematic of two non-linearity corrected waveforms corresponding to the same initial interaction energy with different charge trapping effects.

of the waveform during the drift of the charges, while the falling edge is due to the decay time constant of the preamplifier. The effective pole-zero constant has an extra term of charge trapping constant, τ_{CT}, in addition to the standard pole-zero constant, τ_{RC}, described by:

$$\frac{1}{\tau} = \frac{1}{\tau_{RC}} - \frac{1}{\tau_{CT}} \tag{3.2}$$

In Eq. 3.2, τ_{RC} is approximately 70 μs [55] but τ_{CT} is unknown and depends on each detector. Therefore, in practice, the assumed value of τ is varied until the minimum FWHM value of the detector is achieved. Based on the optimum value of τ that minimizes the energy resolution as seen in Fig. 3.5, τ_{CT} is ≈ 100 μs. The value of τ is estimated for each detector for each data set based on the energy resolution at 2614 keV γ-peak in the calibration data. After applying optimized pole-zero correction, the falling edge of the waveforms that correspond to the same initial interaction energy aligned with each other as in Fig. 3.5.

3.1.3 Uncalibrated Energy Estimators

The energy of each event is estimated based on the height of the waveform at a fixed pick-off time relative to the start time, t_0, of the waveform by applying a recursive trapezoidal filter [89]. The

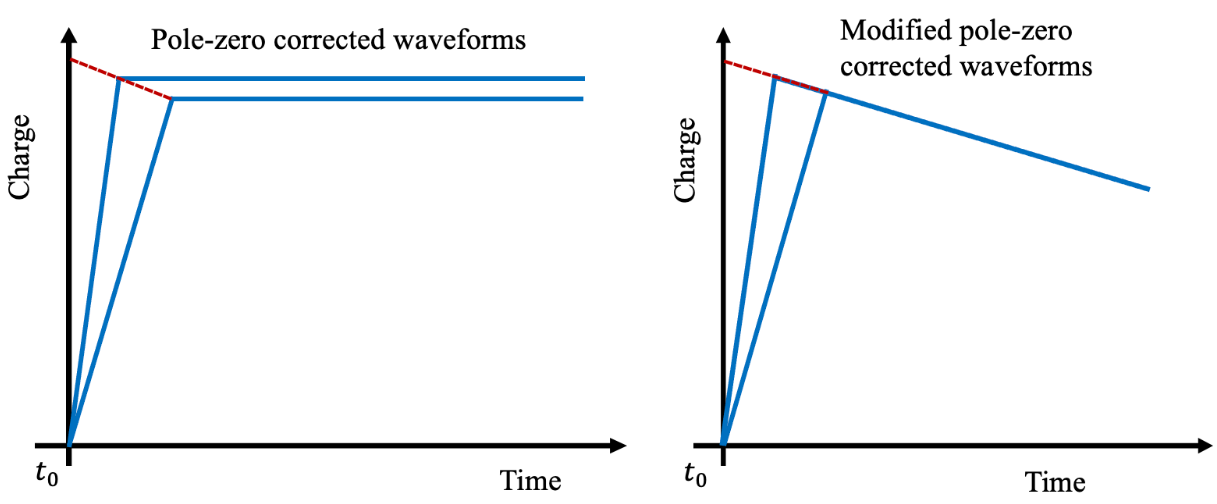

FIGURE 3.4: (Left): A schematic of two waveforms corresponding to the same initial interaction energy. The falling edge of the waveforms becomes flat after applying the pole-zero correction. (Right): The same waveforms after the modified pole-zero correction, which takes into account the standard pole-zero and charge trapping corrections.

fixed pick-off time is the same for all events and is set to 0.5 μs so that height is calculated along the overlapping falling edges of the waveforms. A precise calculation of t_0 is necessary to correctly calculate the pick-off time. The t_0 of each waveform is evaluated by using a leading-edge algorithm. The waveform is first smoothed by applying a short trapezoidal filter called a trigger trapezoidal filter with a ramp time of 1 μs and flat-top of 1.5 μs to reduce high-frequency noise. The maximum of the trapezoidal filter output is found between the time window of 4-14 μs. Then the t_0 is found by walking backward from the maximum of trapezoidal filter output until a threshold crossing of 2 ADC units, then interpolating between the samples before and after the threshold crossing. Once t_0 is obtained, a trapezoidal filter is applied by combining fixed-time pick-off with optimized pole-zero correction as described in Sec. 3.1.2 to estimate the uncalibrated energy of the event. The symmetrical trapezoidal filter has a ramp time of 4 μs and a flat-top of 2.5 μs. The t_0 and hence the energy estimation technique is illustrated in Fig. 3.6. The uncalibrated energy of the waveform estimated in this way is called `trapENF`.

The Majorana Demonstrator has achieved the best energy resolution and the excellent energy linearity of any current generation $0\nu\beta\beta$ experiments by using the `trapENF` energy estimator [55]. However, it was possible to further improve it, especially in the low-energy region, by

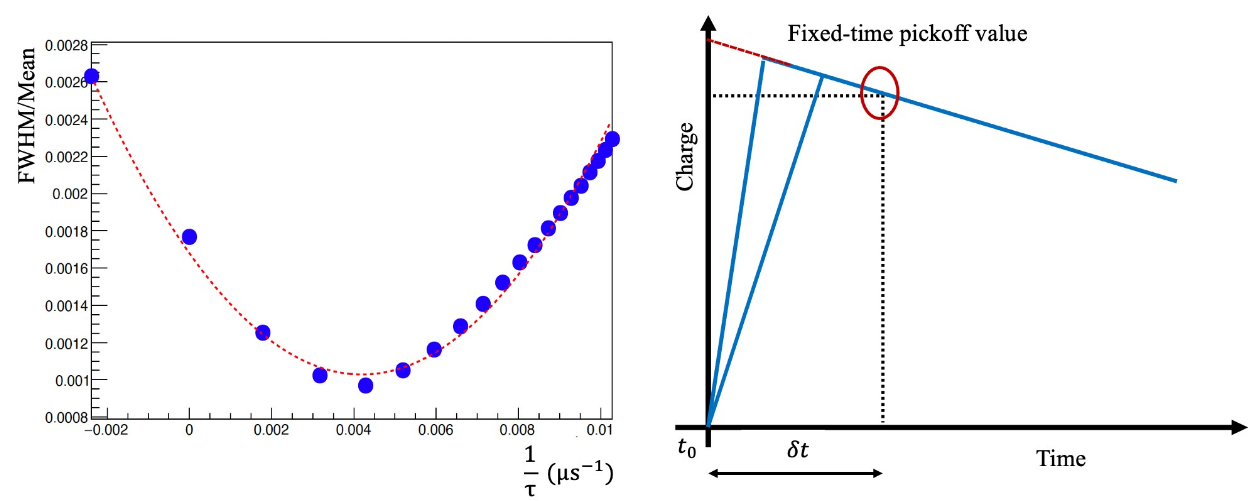

Figure 3.5: ((Left): Variation of FWHM/Mean verses $\frac{1}{\tau}$ with the quadratic fit function which shows the minimum resolution at $\tau_{CT} \approx 100$ μs. (Right): The falling edge of the waveforms overlaps after optimized pole-zero correction is applied. Uncalibrated energy is estimated as a fixed-time pickoff value relative to the t_0 of the waveform where $\delta t = t_{ramp} + t_{flat}$ - 0.5 μs. Here, t_{ramp} and t_{flat} are the ramp time and flat time of the longer trapezoidal filter shown in Fig. 3.6.

improving the t_0 estimation. Improvement is possible because at lower energy, a small energy-dependent systematic drift in t_0 was observed with `trapENF`. Therefore, a new energy estimator is developed with improvement in the t_0 estimation. We improved the estimation by using ^{228}Th calibration data by looking at the time difference between two hits, 583 keV, and a second γ-ray, that are in coincidence. The average time difference between two hits in an event should be close to zero. Therefore, the energy-dependent correction to the time difference is applied empirically to make the difference close to zero, as shown in the right plot of Fig. 3.7. The energy estimator obtained after improvement in t_0 estimation is `trapENFC`.

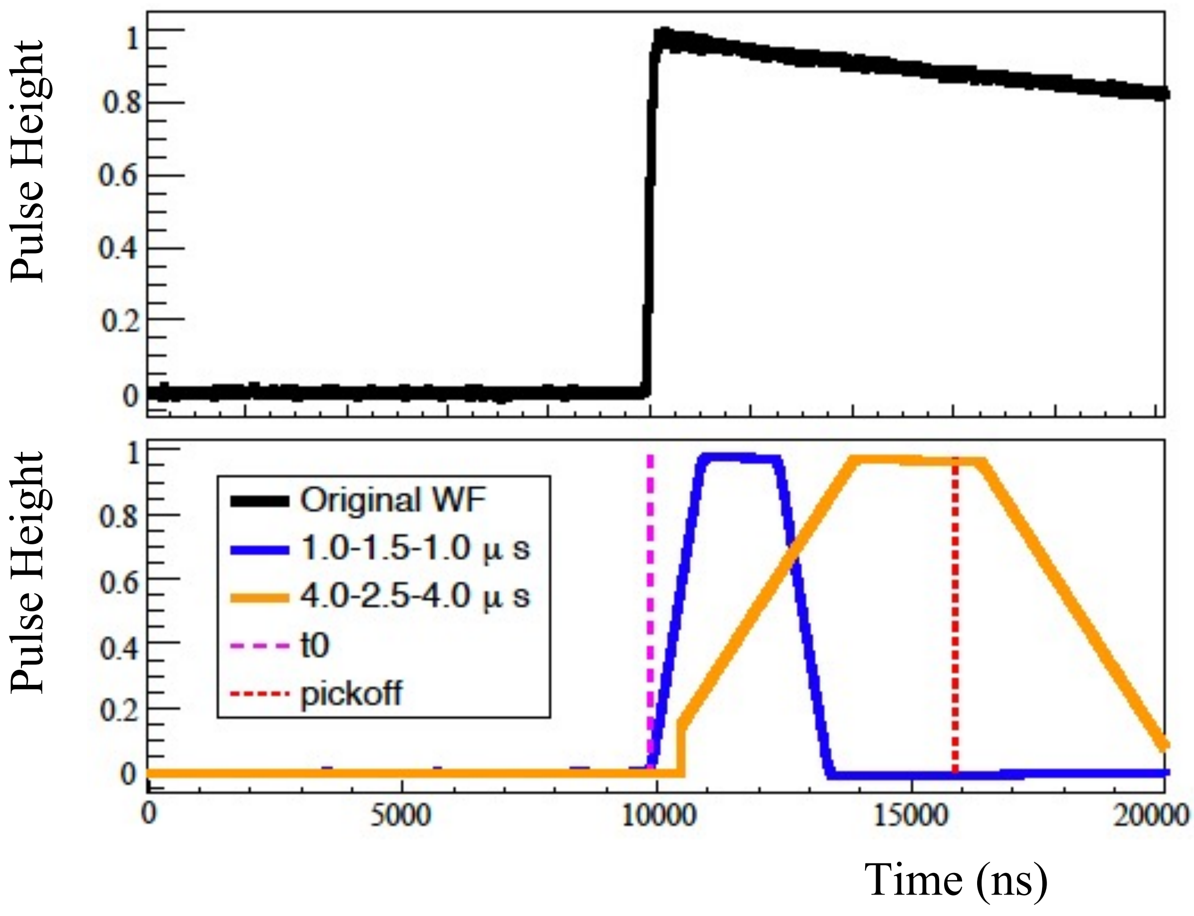

FIGURE 3.6: An illustration of a fixed-time pick-off technique to estimate the uncalibrated energy of the waveform. (Top): A normalized raw waveform. (Bottom): A short trapezoidal output for the $t0$ estimation and a long trapezoidal filter to estimate the uncalibrated energy of the waveform.

3.2 Energy Calibration

In the Majorana Demonstrator, custom-build ^{228}Th calibration line sources manufactured by Eckert & Ziegler Analytics, Inc[1] are used for energy calibration. Each calibration source is 4.7 m long with an integrated activity of 10.36±0.6 kBq measured on May 1, 2013, along the last 2 m of the source. During background data-taking, these sources remain seated outside the shield layers. They were inserted in the calibration track made of polytetrafluoroethylene (PTFE) that surrounds the cryostat in a helical path, as shown in Fig. 3.8 during the calibration data-taking. The calibration system is described in detail in Ref. [90]. ^{228}Th source was chosen since its decay chain provides a large number of prominent γ-rays from 238 keV to 2615 keV that spans the $Q_{\beta\beta}$. These γ-rays are used to calibrate and characterize the detectors. Table 3.1 summarizes some of the most prominent γ-rays from the decay chain used in characterizing the detectors in the Majorana Demonstrator.

For each module, calibration data is taken every week with a source deployed in the track for approximately 60 to 120 min. The calibration time is increased in later data sets to compensate for the decaying activity of the sources. Also, an approximately 17-hour long calibration data is taken about once every two months. The long calibration data have enough statistics for tuning pulse

[1] https://www.ezag.com/home/

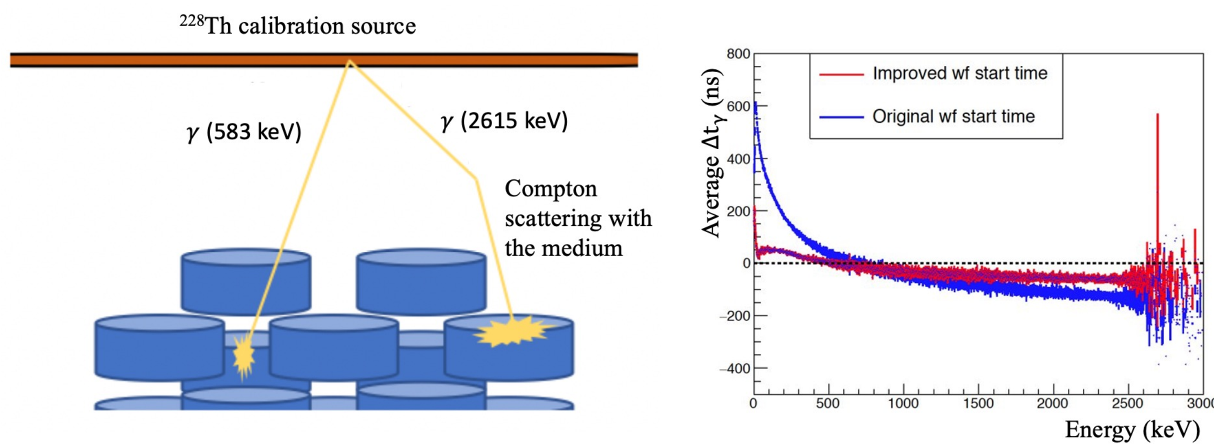

Figure 3.7: (Left): A schematic showing a coincidence hit of 583 keV γ and a second γ from the Compton scattering of a 2615 keV γ-ray from the calibration source in the detectors. (Right): Time difference between two hits of the signal with correction (red) and without correction (blue) in t_0 estimation.

Table 3.1: The overview of some most prominent γ-rays from the decay chain of ^{228}Th that are used in the MAJORANA DEMONSTRATOR energy calibration.

Energy (keV)	Isotopes	Intensity per ^{228}Th decay
238.63	^{212}Pb	0.433
240.99	^{224}Ra	0.041
277.36	^{208}Tl	0.023
300.09	^{212}Pb	0.032
583.19	^{208}Tl	0.304
727.33	^{212}Bi	0.065
785.37	^{212}Bi	0.011
860.56	^{208}Tl	0.044
2614.53	^{208}Tl	0.356

shape analysis parameters such as *avse* [77] and *dcr* [78]. In addition, calibration data with a ^{56}Co source deployed in each track for one week at a time was taken in January 2019. ^{56}Co source emits a large number of γ-rays above 1.5 MeV and hence produces several double escape peaks, which were used for the systematic study of pulse shape analysis parameters.

The DEMONSTRATOR puts a dedicated efforts to convert raw energies, `trapENF`, and `tapENFC`, to the calibrated energies which are used for the physics analysis. The spectrum is calibrated by comparing the real energies of known γ-peaks in the ^{228}Th decay chain to their positions in the uncalibrated energy spectrum. Figure 3.9 shows the high-level flow chart for the energy calibration

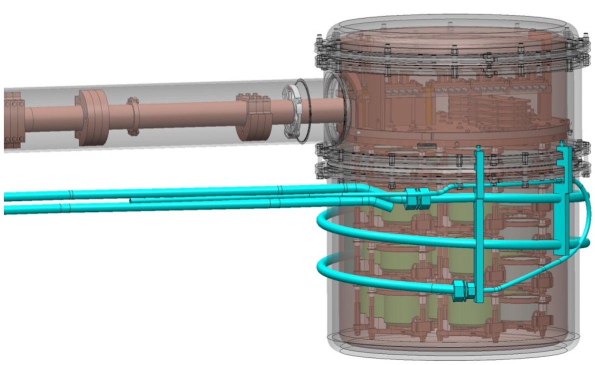

FIGURE 3.8: (Left): A drawing of a module and calibration track. (Right): A photo of a module and its calibration track inside the shielding. Calibration sources sit outside the shield layers during background data-taking and are deployed through the track during calibration data-taking. Adapted from [90].

and systematic study in the MAJORANA DEMONSTRATOR.

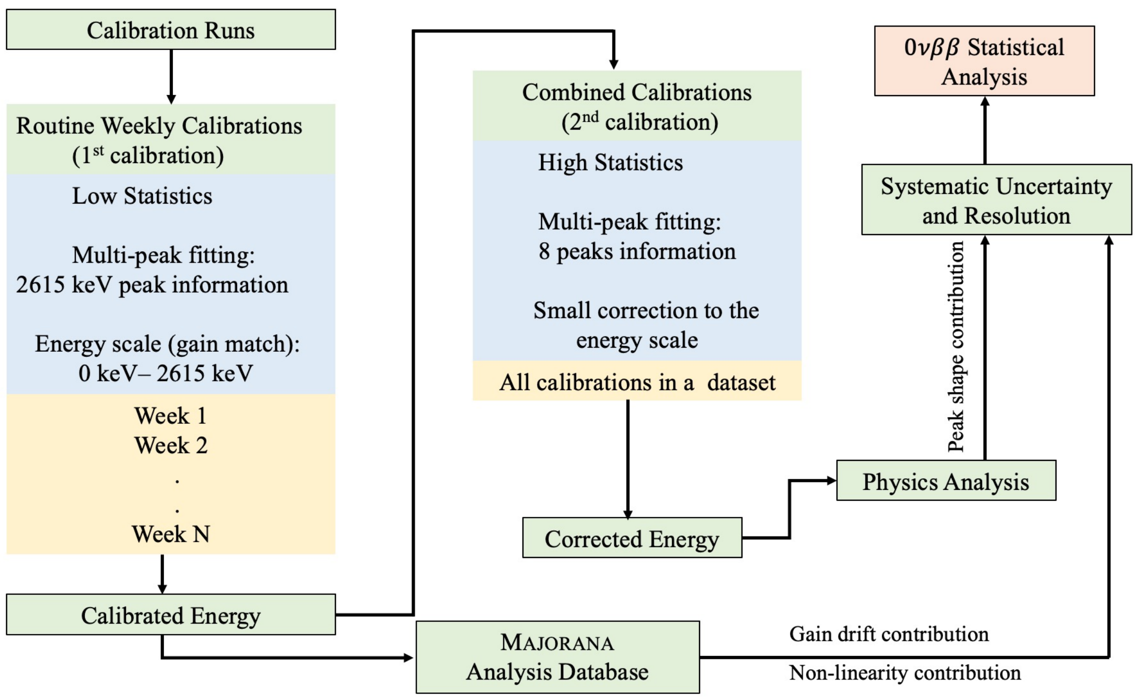

FIGURE 3.9: A flowchart depicting the energy calibration procedure and energy systematic study in MJD. The whole procedure can be divided mainly into three steps; weekly calibration, combined calibration, and systematic.

The γ-ray peaks from the ^{228}Th decay chain are fitted with an analytical peak shape function as shown in Fig. 3.10. The details about the peak shape fitting are described in 3.2.1. The parameters from the fit result, such as gain, offset, and energy resolution of each high-gain and low-gain channel, are extracted from each weekly calibration. Gain matching of these peaks is used to calibrate the detectors. Subsections 3.2.2 and 3.2.3 describe the automatic procedure of weekly and combined calibrations, respectively.

3.2.1 Single and Multi-peak Fitting

A simple energy calibration can be done by fitting the γ-ray peaks with a simple Gaussian function. However, this simple method does not account for other possible features in HPGe detector peaks, such as the low-energy tail and background underneath the peak. Furthermore, any imperfection in the model to fit the peaks would ultimately affect the $0\nu\beta\beta$ peak search. Therefore, a typical peak shape function which consists of different individual functions to model the γ-ray peak that accounts for those effects [91–93] is used in the MAJORANA DEMONSTRATOR. The different components in the peak shape function are given in Eq. 3.3.

$$\mathrm{PS}(E) = \mathrm{G}(E) + \mathrm{T_{LE}}(E) + \mathrm{T_{HE}}(E) + \mathrm{S_B}(E) \tag{3.3}$$

- $\mathrm{G}(E)$ in Eq. 3.3 is a Gaussian function with low-energy and high-energy tail contributions to the peak.

$$\mathrm{G}(E) = \frac{A(1 - f_{LE} - f_{HE})}{\sqrt{2\pi}\sigma} \exp\left(-\frac{(E-\mu)^2}{2\sigma}\right) \tag{3.4}$$

  where,

  A = Total area of the peak; number of counts in the Gaussian and tail functions

  μ = mean of Gaussian function

  σ = standard deviation of Gaussian function

  f_{LE} and f_{HE} = fraction of the total area contained in LE/HE tail where, $0 \leqslant f_{LE} \leqslant 1$; $0 \leqslant f_{HE} \leqslant 1$; $0 \leqslant f_{HE} + f_{LE} \leqslant 1$

- The presence of a low-energy tail in the peak shape is mainly due to incomplete charge collection, resulting in loss of energy. The loss of charge collection occurs due to the effect of charge trapping and interaction at the transition layers of the detector. The low-energy tail function, $\mathrm{T_{LE}}(E)$, is the exponentially modified Gaussian function that shares three same parameters that are in a normal Gaussian function.

$$\mathrm{T_{LE}}(\mathrm{E}) = \frac{Af_{LE}}{2\tau_{LE}} \exp\left(\frac{\sigma^2}{2\tau_{LE}^2} - \frac{E-\mu}{\tau_{LE}}\right) \times \mathrm{erfc}\left(\frac{\sigma}{\sqrt{2}\tau_{LE}} - \frac{E-\mu}{\sqrt{2}\sigma}\right) \tag{3.5}$$

  where τ_{LE} is the decay constant of the tail exponential or length of the LE tail

- $\mathrm{T_{HE}}(\mathrm{E})$ is generally not used due to negligible contributions of the high-energy tail in the peak shape by setting $f_{HE} = 0$. However, it is required if unusual peak shapes are observed. For example, the unusual peak shape is possible due to imperfect setting of the energy filter parameters or fitting of energy peaks other than full energy γ-ray peaks from the ^{228}Th decay chain.

$$\mathrm{T_{HE}(E)} = \frac{Af_{HE}}{2\tau_{HE}} \exp(\frac{\sigma^2}{2\tau_{HE}^2} + \frac{E-\mu}{\tau_{HE}}) \times \mathrm{erfc}(\frac{\sigma}{\sqrt{2}\tau_{HE}} + \frac{E-\mu}{\sqrt{2}\sigma}) \tag{3.6}$$

Here, τ_{HE} is the decay constant of the tail exponential or length of the HE tail.

- The step background function, $\mathrm{S_B}(E)$, in the peak shape model is due to low-angle scattering of γ-rays before being captured in the bulk or the transition layers of detectors which results in slight energy loss. This is possible because those γ-rays originate from the calibration track outside the copper cryostat.

$$\mathrm{S_B}(E) = \frac{H_s}{2} \mathrm{erfc}(\frac{E-\mu}{\sqrt{2}\sigma}) \tag{3.7}$$

where,

H_s is the height of the step background as the fraction of the peak amplitude defined as

$$H_s(E) = \frac{h_0}{E^2} + h_1 E^{-0.88} \tag{3.8}$$

The first term in Eq. 3.8 is due to the low-angle scattering of γ-rays, and the second term represents their interaction at the transition layers of detectors. The power term -0.88 was chosen based on the measurement from simulation and data [94].

The fitting is performed by adding a quadratic background function to the peak shape function as described in Eq. 3.3. The quadratic component of background function, $\mathrm{BG}(E)$, is described as

$$\mathrm{BG}(E) = q\frac{1}{2}(E^2 - 1) + mE + b \tag{3.9}$$

where,

q = quadratic component of background

m = linear component of the background

b = flat portion of the background

These components are independent of the fitting energy region. The background model is referred to as a quadratic; however, it depends on the energy region where the fitting is performed. It is often used just a flat background by fixing $q = 0$, and $m = 0$ or a linear background by fixing just $q = 0$. The amount of statistics mainly constrains the choice. For example, a fit of the 2614-keV peak assumes only the flat portion of the background due to low statistics to consider linear or quadratic components.

In Majorana Demonstrator, multiple approaches were adopted for energy calibration over time with the improvements on the newer approach. Each approach completes in two steps of calibration, referred to as weekly calibration and combined calibration. These two steps of calibration are described in Subsections 3.2.2 and 3.2.3. Initially, the fit was performed on individual γ-peaks separately using an algorithm named `GATPeakShape::EZFit`, which uses the analytical peak fitting functions described earlier. This algorithm fits using MINUIT minimization packages, MIGRAND, [95, 96].

The fitting with `GATPeakshape::EZFit` function worked well with some limitations. For example, when two γ-peaks are very close to each other, the result of individual peak fittings might be inaccurate. A possible case is fitting of 238-keV and 240-keV γ-peaks. In addition, the fitting fails for the low statistics γ-peaks. To overcome the limitations, a global fitting function, `GATMultiPeakFitter::GATMultiPeakFitter` (multi-peak-fitter), was developed. This function fits multiple γ-peaks in the calibration data simultaneously. The spectrum is divided into different energy regions containing single or multiple γ-peaks. There are eight peak shape parameters and three background parameters in each energy region. The peak shape parameters are determined based on the physical energy of γ-peak and corresponding hyper-parameters, while the background parameters are constant for the same energy region. Those issues are resolved since larger peaks mainly determine the peak shape parameters. The successful fitting of a smaller peaks helps reduce the effect of systematics such as non-linearity in the digitizer.

The fitting function for each energy region, F_j, is given by

$$F_j = \sum_i \mathrm{PS}_i(A_i, \mu_i, \sigma_i, \tau_{LE,i}, f_{LE,i}, \tau_{HE,i}, f_{HE,i}, H_{s,i}) + \mathrm{BG}_j(q_j, m_j, b_j) \tag{3.10}$$

The eight peak shape parameters are described below.

- $A_i = A_i$

  A is independent of energy and it depends only on the relative amplitude of each γ-peak

- $\mu_i = \mu_0 + \mu_1 E_i$

  μ appears to be linearly proportional to energy. However, to avoid systematic errors in the peak shape parameter due to non-linearities, it is considered as independent.

- $\sigma_i = \sqrt{\sigma_0^2 + \sigma_1^2 E_i + \sigma_2^2 E_i^2}$

  σ_0 arises from electron noise, σ_1 is arises from Fano factor F, and electron-hope production

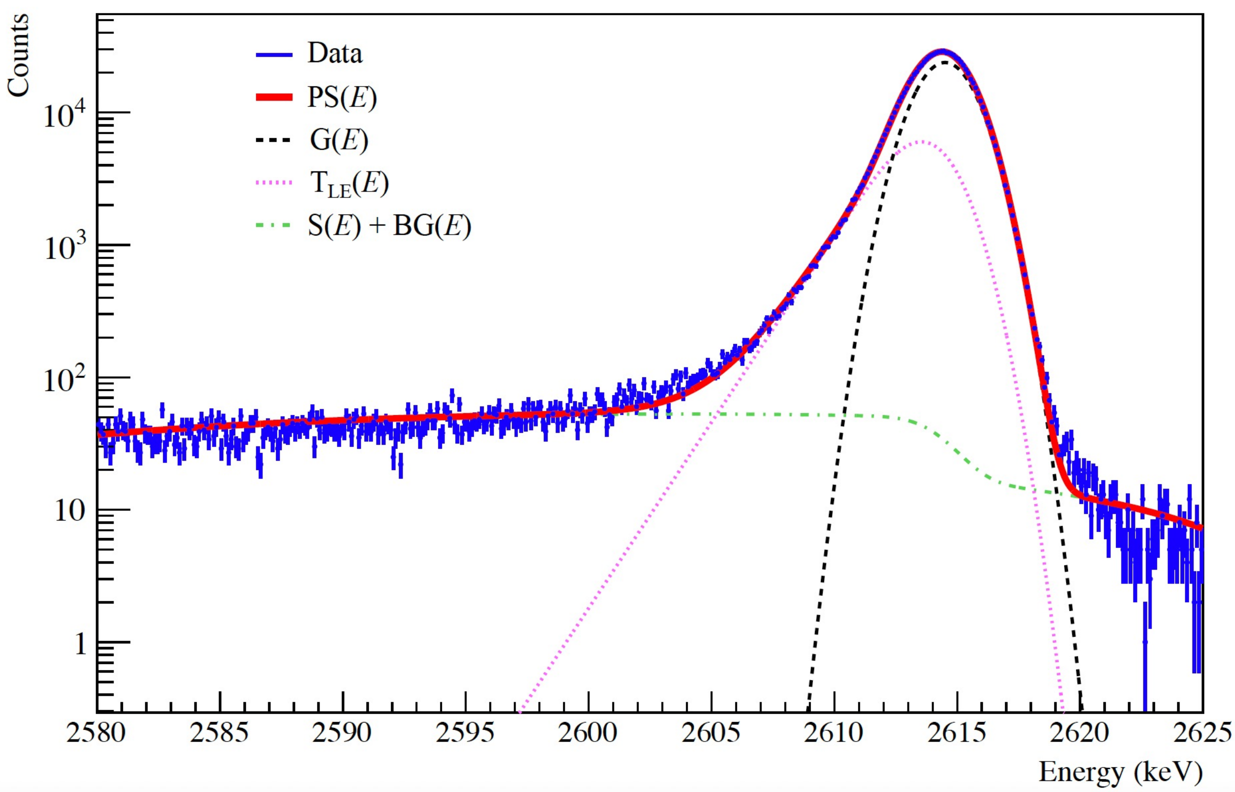

FIGURE 3.10: The peak shape model fitted with `GATPeakShape::EZFit` algorithm applied to 2615-keV γ-peak. Fit is performed to the same data as in Ref. [55]. The peak shape function (red) includes Gaussian (black), low-energy tail (magenta), step, and quadratic background (green). The FWHM of the peak is 2.95 keV.

energy given by $\sigma_1 = (2.35)^2 F\epsilon E$ and σ_2 arises from various energy systematic uncertainties including charge trapping and gain drift between calibrations.

- $\tau_{LE,i} = \tau_{LE,0} + \tau_{LE,1} E_i$ and $\tau_{HE,i} = \tau_{HE,0} + \tau_{HE,1} E_i$

  τ depends linearly with energy.

- $f_{LE,i} = f_{LE,0}$ and $f_{HE,i} = f_{HE,i}$

  $f_{LE/HE,0}$ arise from electronic noise.

- $H_{s,i} = \frac{H_{s,0}}{E_i^2} + H_{s,1} E_i^{-0.88}$

  This is equivalent to Eq. 3.8 and re-written for i^{th} peak.

- q, m and b are the different components in the background function as described in Eq. 3.2.1

A large number of fitting parameters is required to fit multiple regions and γ-peaks simultaneously, with many of the parameters in high correlation. Therefore, successful fits are heavily dependent on the initial parameters guess. However, manual parameter tuning is not feasible due to a large number of detectors in the Majorana Demonstrator. Therefore, a Hamiltonian Monte Carlo (HMC) [97, 98], a gradient-based Markov Chain Monte Carlo (MCMC) technique, was first used to enable successful convergence of MIGRAD fits with coarsely generated initial parameters. In addition, to increase the rate of convergence of fits, a mass scale matrix based on the Riemann Manifold Hybrid Monte Carlo (RMHMC) technique [99] is adapted. Adapting the various methods in the multi-peak-fitter algorithm resulted in quick and reliable convergence. Figure 3.11 shows the fitting of multiple energy regions simultaneously using this multi-peak-fitter.

3.2.2 Weekly Calibration

In Majorana Demonstrator, weekly calibration provides parameters for the first step of conversion of uncalibrated energy to calibrated energy. Then, those parameters are used for the corresponding calibration runs and following background runs before the next calibration runs. This helps to monitor any electronic variation and detector behavior on a weekly basis.

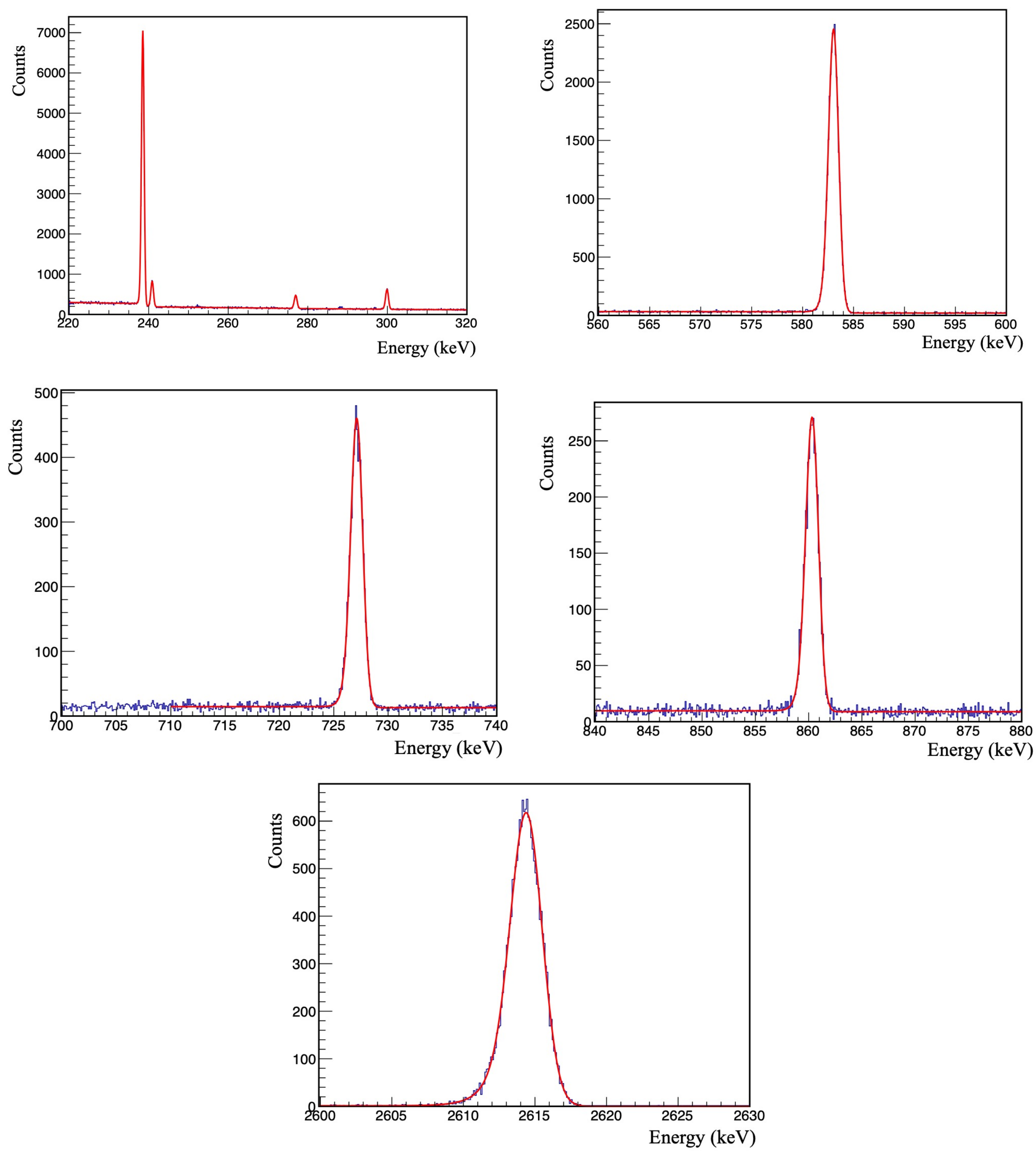

FIGURE 3.11: An example of a simultaneous fit of four energy regions containing eight γ-ray peaks of a single detector in the DS8 dataset. Fit is performed with $f_{HE} = 0$, and different background in each region; quadratic background in 220-320 keV ($b \neq 0$, $m \neq 0$, $q \neq 0$), linear background ($b \neq 0$, $m \neq 0$, q=0) in 560-600 keV and flat background ($b \neq 0$, m=0, q=0) in higher remaining energy regions.

E = 0 calibration

In this approach, four γ-peaks in the calibration data were used and fitted individually using `GATPeakShape::EZFit` algorithm. The selected γ-peaks for the fitting were 238.6 keV, 283.2 keV, 727.3 keV and 2614.5 keV. In addition to these physical γ-peaks, an additional peak called E=0 was also used. At first, the most prominent 2614.5 keV peak is identified based on the highest energy peak in the uncalibrated energy spectrum. Then the locations of the other peaks were estimated based on the 2614.5 keV peak. The E = 0 peak refereed to the events which deposit no energy in the detector. This peak can be found by applying a trapezoidal filter to the waveform produced in the forced-trigger runs or delayed-trigger runs. The detail procedure is given in [100]. The fitting parameters, peak positions, and uncertainties in terms of ADC values were stored in the database. The parameters of the linear fitting of peak positions were used to convert uncalibrated energy to calibrated energy.

$$E_{calibrated} = a_0 + a_1 E_{uncalibrated} \tag{3.11}$$

where a_0 and a_1 are the offset and energy scale of the calibrations. Initially, this approach of the weekly calibration was applied and implemented in [79].

Gain Match Calibration

This new approach to calibration is applied to calibrate both energies: `trapENF` and `trapENFC` energies. The multi-peak-fitter algorithm is used to fit γ-peaks in the calibration spectrum simultaneously; however, only the information of the most prominent peak, 2614 keV, is used. The fitting may fail in some low statistics γ-peaks, but the parameters of other lower energy γ-peaks are not used in the weekly calibration. Additionally, a summary document was created for each weekly calibration to review any fitting failures. The peak position and corresponding uncertainty of 2614 keV peak from each high-gain and low-gain channels are extracted. Then, the linear fitting is performed with no offset as described in Eq. 3.12 for gain matching. This linear scale conversion gives the corresponding calibrated energy. The weekly calibration with this approach has been used since the 2019 $0\nu\beta\beta$ analysis [55].

$$E_{calibrated} = a_1 E_{uncalibrated} \tag{3.12}$$

Here, a_1 is the calibration scale or gain.

After each calibration, all the plots of fits are reviewed before saving the calibration parameters in the database. Although only the 2614-keV peak fitting is used in the weekly calibration, the document provided a summary of the calibration of the 238.6-keV, 241-keV, 277.4-keV, 300.1-keV, 583.2-keV, 727.3-keV, 763.1-keV, 785.4-keV, 860.6-keV and 2614.5-keV peaks in the uncalibrated energy spectrum of each high-gain and low-gain channel. A manual check of the plots is necessary to ensure calibration has been done successfully. For example, the fit of 2614-keV γ-peak as shown in Fig. 3.12. Some other plots that were checked in each weekly calibration are shown in Fig. 3.13, Fig. 3.14, and Fig. 3.15. In addition, any instability or upgrade of electronics (digitizer) may drift the peak positions in the uncalibrated energy spectrum. Such drift is monitored every week. Suppose the drift of the peak position of the 2614-keV γ is more than 2 keV between consecutive calibrations. The corresponding channel in the background period between the calibrations is not used for any analysis.

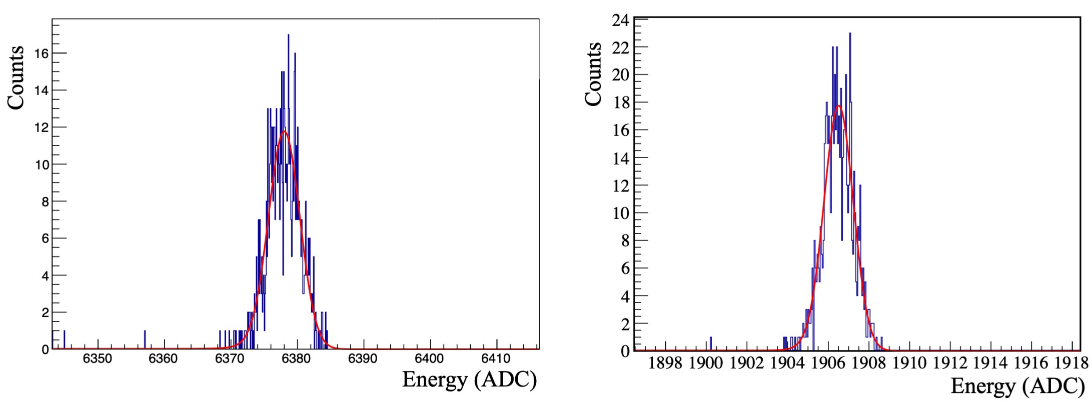

FIGURE 3.12: Fit of 2614-keV γ-peak in the high-gain channel (left) and low-gain (right) of detector C2P4D1 in a weekly calibration of the DS8 dataset.

3.2.3 Combined Calibration

The weekly calibration in both approaches explained in 3.2.2 relies on either fitting some peaks individually or a multi-peak fitting, but only the 2614-keV peak fit parameters are used. Those

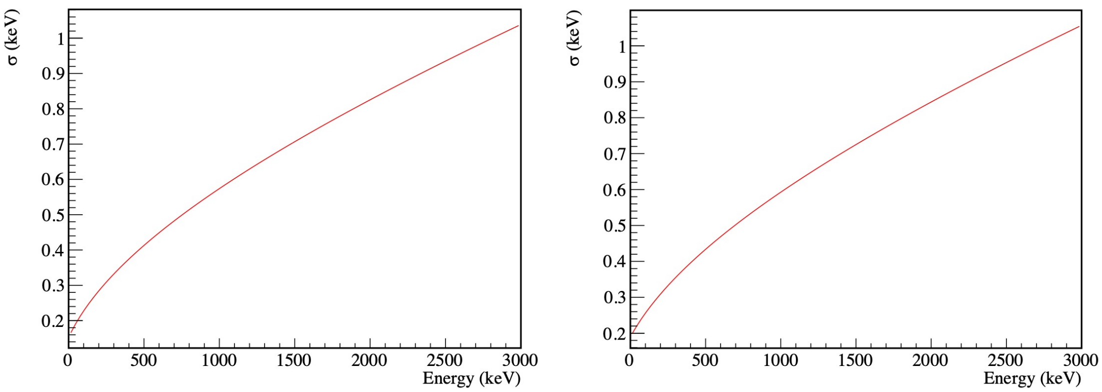

FIGURE 3.13: Energy resolution curve of high-gain and low-gain channel of detector C2P4D1 in a weekly calibration in DS8 dataset.

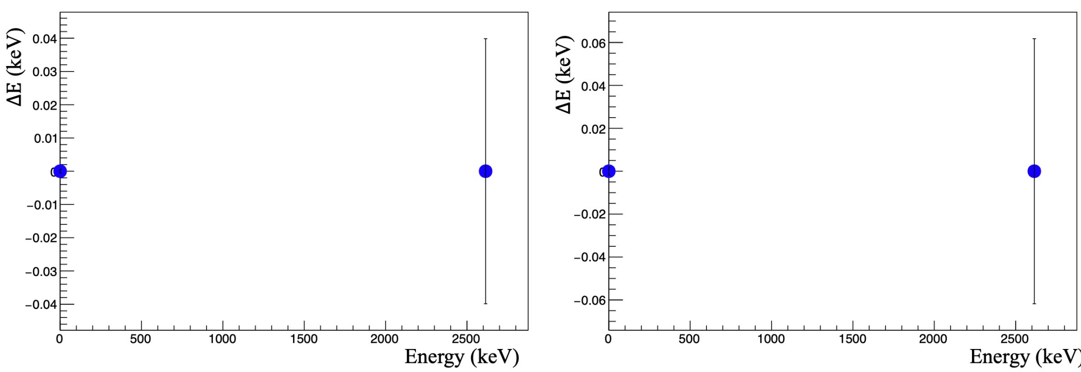

FIGURE 3.14: Energy uncertainty of high-gain and low-gain channel of detector C2P4D1 in a weekly calibration in DS8 dataset.

approaches are great as they provide some early monitoring of the detectors; however, the energy performance is not as robust as MAJORANA DEMONSTRATOR experiment desired. In the low energy region, below 1 MeV, there existed non-linearities up to 0.15 keV compared to the actual energy of a γ from the ^{228}Th decay chain. After the end of each dataset, a calibration for more-finely tuned parameters is obtained by combining all weekly calibrations. Doing so, there is enough statistics to apply multi-peak-fitter, which gives finely tuned calibration parameters to correct over previously calibrated energies. Figure 3.16 is a sample plot for energy residual and energy scale from 8 γ-peaks used in the combined calibrations. The linear energy correction is performed over previously calibrated energy obtained from `trapENF` estimator as given by,

$$E_{corrected} = b_0 + b_1 E_{calibrated} \tag{3.13}$$

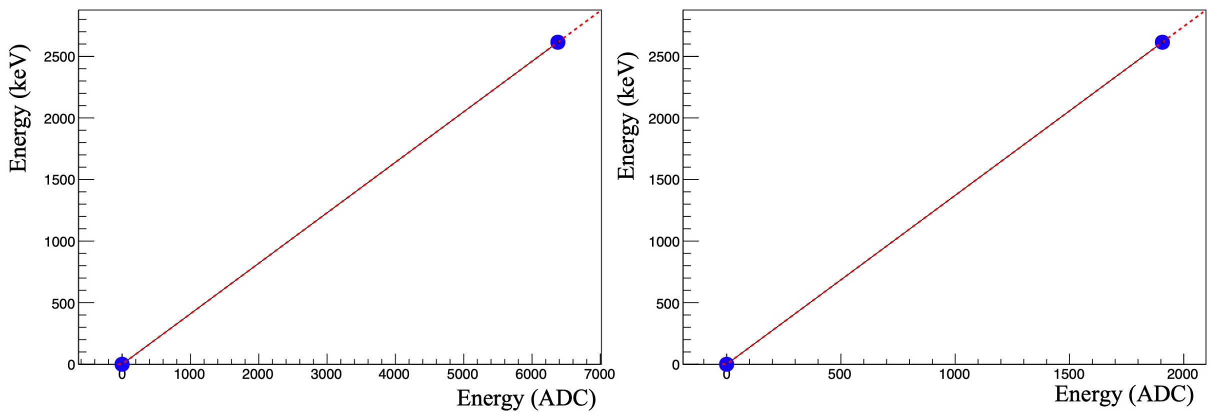

FIGURE 3.15: Linear energy scale of high-gain and low-gain channel of detector C2P4D1 in a weekly calibration DS8 dataset.

Here, b_0, b_1 are offset and slope of linear scale calibration.

The weekly calibration of the new energy estimator, `trapENFC` is done with a similar approach as in `trapENF`. However, quadratic calibration is done instead of a linear one for a combined calibration. The quadratic correction to the energy obtained from the improved energy estimator further improves the linearity in the low-energy region. This new energy has been used in the final result of the DEMONSTRATOR.

$$E_{corrected} = c_1 E_{calibrated} + c_2 E^2_{calibrated} \tag{3.14}$$

Here, c_1 and c_2 are the quadratic components parameters.

3.3 Energy Systematic

The statistical analysis of $0\nu\beta\beta$ needs to define the region of interest (ROI) where the corresponding events can be detected. The ROI is determined based on the systematic study of energy resolution and energy uncertainty at the nominal $0\nu\beta\beta$ energy position. The section describes the summary of the energy systematic of the MAJORANA DEMONSTRATOR. One can found a detail summary of energy systematic in Ref. [101]. Here, only a brief description is provided.

3.3.1 Energy Resolution

The final energy resolution, $\sigma(E)$, at any energy, E, is calculated based on Eq. 3.15. It has two components where $\sigma_{fit}(E)$ represents the resolution obtained by the spectral fit of multiple γ-peaks and $\sigma_{drift}(E)$ represents the contribution of energy drift observed between the weekly calibrations to the energy resolution.

$$\sigma(E) = \sqrt{\sigma_{fit}^2(E) + \sigma_{drift}^2(E)} \tag{3.15}$$

Energy Resolution from Spectral Fit ($\sigma_{fit}(E)$)

The energy resolution from the spectral fit as a function of energy is estimated based on the fitting function given by Eq. 3.15. The function is used to fit the energy resolution values obtained from simultaneous fit of multiple γ-peaks in the ^{228}Th calibration data. For example, the simultaneous fit of 24 γ-peaks, fit on FWHM energy resolution values, and residuals in energy resolution are shown in Fig. 3.17.

$$\sigma_{fit}(E) = \sqrt{p_0^2 + p_1^2 E + p_2^2 E^2} \tag{3.16}$$

Where P_0, P_1 and P_2 account for electronic noise, Fano noise and charge trapping respectively.

Energy Resolution from Energy Drift ($\sigma_{drift}(E)$)

The drift of γ-peak position also affects the energy resolution. The contribution of energy drift to the energy resolution at energy E is estimated based on Eq. 3.17.

$$\sigma_{drift}(E) = \sigma_{drift}(2615)\frac{E}{2615} \tag{3.17}$$

Here, $\sigma_{drift}(2615)$ is the contribution to the energy resolution at 2615-keV γ-peak position due to energy drift of 2615-keV peak between the weekly calibrations. The $\sigma_{drift}(2615)$ value is estimated based on Eq. 3.18.

$$\sigma_{drift}(2615) = \frac{1}{2}\sigma_{\Delta_c} = \frac{1}{2}\sqrt{\frac{1}{N}\sum_{ij}^{N}(\Delta_{ij}^c - \bar{\Delta}_c)^2} \tag{3.18}$$

where,

N = Total number of weekly calibrations,

index i = Weekly calibrations,

index j = Total number of detectors,

Δ^c_{ij} = Energy drift of 2615-keV γ-peak between consecutive weekly calibrations, and

$\bar{\Delta}_c$ = Average energy drift of 2615-keV γ-peak considering all weekly calibrations and all detectors

Uncertainty in Energy Resolution

Different sources of uncertainties contribute to the uncertainty in energy resolution. The individual uncertainty sources and how they are addressed in the MAJORANA DEMONSTRATOR are described in the following points.

- Statistical uncertainty: The statistical uncertainty in the energy resolution at energy E is estimated based on Eq. 3.19.

$$\delta_{\sigma,stat}(E) = \sqrt{J_\sigma \Sigma_\sigma J_\sigma^T} \tag{3.19}$$

  where,

  J_σ = Jacobian of Eq. 3.16 with respect to the parameters, and

  Σ_σ = covariance matrix of the fit

- Uncertainty due to energy drift: Any uncertainty in the drift variance, $\sigma^2_{\Delta_c}$, given in Eq. 3.18 contribute to the uncertainty in energy resolution. This uncertainty is estimated by Eq. 3.20.

$$\delta_{\sigma^2_{\Delta_c}}(E) = \sqrt{\frac{1}{N}\left(\mu_{4\Delta_c}(E) - \frac{N-3}{N-1}\sigma^4_{\Delta_c}(E)\right)} \tag{3.20}$$

  where,

  the $\mu_{4\Delta_c}(E)$ is the fourth central moment estimated by

$$\mu_{4\Delta_c}(E) = \frac{1}{N}\sum_{i=1}^{N_d}\sum_{j=1}^{N_c}\left(\Delta^c_{ij}(E) - \overline{\Delta}_c(E)\right)^4 \tag{3.21}$$

- Uncertainty due to ADC non-linearity: The local ADC non-linearity shifts the whole γ-peak in approximately the same amount without affecting the peak width and shape. Therefore, its contribution is not considered in the uncertainty.

3.3.2 Energy Scale Uncertainty

The total uncertainty in the energy scale at mean value μ with the actual energy deposition E is estimated by Eq. 3.22.

$$\delta_{\mu}(E) = \sqrt{\delta^2_{\mu,stat+NL_{global}}(E) + \delta^2_{\mu,drift}(E) + \delta^2_{\mu,NL_{local}}(E)} \tag{3.22}$$

The three different sources of uncertainties that contribute to the uncertainty in the energy scale are described in the following points.

- Uncertainty due to statistical and global non-linearity: The uncertainty in energy scale due to statistical and global non-linearity was computed by fitting multiple peaks in the ^{228}Th calibration data by `GATMultiPeakFitter`. Figure 3.18 shows the energy spectrum and 24 γ-peaks used for the systematic study of uncertainty. The peak positions and errors from the multi-peak fitter are extracted. A linear fit given in Eq. 3.23 is used to fit the peak positions to their nominal energy.

$$\mu(E) = \mu_0 + \mu_1 E \tag{3.23}$$

If the calibration is ideal, the parameters μ_0 and μ_1 take the values 0 and 1, respectively, within the corresponding errors. The uncertainty in those parameters is then propagated to the energy scale. The statistical uncertainty as a function of energy, $\delta_{stat}(E)$, due to uncertainties in those parameters is computed based on Eq. 3.24.

$$\delta_{stat}(E) = \sqrt{\delta^2_{\mu_0} + \delta^2_{\mu_1} E^2 + 2E * cov(\mu_0, \mu_1)} \tag{3.24}$$

where,

δ_{μ_0} = uncertainty in μ_0

δ_{μ_1} = uncertainty in μ_1

cov(μ_0, μ_1) = covariance of μ_0 and μ_1

However, we observed a non-statistical spread of the difference between μ and nominal energy E around 0, which is due to ADC non-linearities. These uncertainties affect the global energy scale. Therefore, uncertainty contribution due to global non-linearity is added to the statistical contribution so that the combined uncertainty is computed based on Eq. 3.25.

$$\delta_{stat+NL_{global}}(E) = \delta_{stat}(E)\sqrt{\frac{1}{N_p - 2}\sum_{k=1}^{N_p}\frac{\Delta_k^2}{\delta_{stat,k}^2}} \tag{3.25}$$

where,

N_p = Number of γ-peaks used for the calculation

Δ_k = Difference between $\mu(E)$ and E of k^{th} γ-peak

$\delta_{stat,k}$ = $\delta_{stat}(E)$ at the nominal energy E of k^{th} γ-peak

- Uncertainty due to energy drift: There might be energy drift between weekly calibrations so that the peak position get slightly shifted in uncalibrated energy spectrum. However, this type of energy drift is not a systematic drift. Therefore, we do not correct for the energy drift in μ but we include the uncertainty in the energy scale due to such type of possible drifts. The energy drift is calculated based on the 2615-keV peak position in uncalibrated energy spectrum in terms of ADC units.

$$\Delta_{i,j}\,(keV) = (E_{i,j} - E_{i,j+1})\,a_{i,j} \tag{3.26}$$

where,

$\Delta_{i,j}$ = Energy drift of 2615-keV peak in terms of ADC unit between consecutive weekly calibrations j and $j+1$ on detector i

$E_{i,j}$ = Peak position of 2615-keV peak in terms of ADC unit in weekly calibration j on detector i

$a_{i,j}$ = Gain match parameter in calibration j on detector i as given in Eq. 3.12

We calculate the energy drift of the 2615-keV peak between consecutive weekly calibrations on both high-gain and low-gain channels of all detectors. The global effect of energy drift is accounted for in the energy uncertainty and resolution. However, the effect in each background period and the channel is different and depends on the two closest calibrations. Therefore, the drift between calibration j and $j+1$ is more than 2 keV in either of the uncalibrated energies. In that case, we reject all the data from that channel between the calibrations for any physics analysis. For example, Fig. 3.19 shows a stable channel 592 and a channel 1110 with permanent energy drift. The whole data of channel 592 is reliable for analysis, but some period of data where the drift was more than 2 keV was rejected. After rejecting the channel with more than 2 keV energy drift, we accounted for the effect of the remaining drift into the uncertainty of the energy scale.

$$\delta_{\mu,drift}(E) = \sqrt{\left(\frac{1}{2}\overline{\Delta}_{i,j}\right)^2 + \frac{\sigma^2_{drift}}{N}} \tag{3.27}$$

where,

$\overline{\Delta}_{i,j}$ = Average value of energy drift calculated based on all detectors in all weekly calibrations, and the σ^2_{drift} is calculated using Eq. 3.17.

- Uncertainty due to local non-linearity: The non-linearity present in the digitizer is corrected in the first order before digital signal processing. However, any residual non-linearity present might affect the immediate vicinity of the γ-peaks and is accounted for in energy systematics in the Majorana Demonstrator. The uncertainty in energy scale due to such residual non-linearities is computed based on Eq. 3.28.

$$\delta_{\mu,NL_{local}}(E_{i_b}) = \begin{cases} \frac{1}{2}\overline{\Delta}_{NL_{local}}(E_{i_b}), & \text{high-gain} \\ \sqrt{1+\left(\frac{1}{3}\right)^2}\,\overline{\Delta}_{NL_{local}}(E_{i_b}), & \text{low-gain} \end{cases} \tag{3.28}$$

where $\overline{\Delta}_{NL_{local}}(E_{i_b})$ is the average difference between high-gain and low-gain value for energy E_{i_b} in bin i_b computed based on Eq. 3.29

$$\overline{\Delta}_{NL_{local}}(E_{i_b}) = \frac{1}{N}\sum_{i=1}^{N_d}\sum_{j=1}^{N_c}\frac{1}{N_{i_b}}\sum_{E \text{ in bin}}^{N_{i_b}}\left(E^{lg}_{ij} - E^{hg}_{ij}\right) \tag{3.29}$$

where index i, j, and N_{i_b} represent detector, calibrations, and number of events in bin i_b

respectively.

3.4 Energy Performance and Summary

High purity germanium has intrinsically good energy resolution. In Majorana Demonstrator, we applied a dedicated method to further improve the energy performance and achieve the best energy resolution and linearity. The improvement after ADC non-linearity correction can be observed by computing the difference between high-gain and low-gain channel energy. The ADC non-linearity correction results in a significant improvement in energy difference, as shown on the left of Fig. 3.20.

The charge trapping correction resulted in significant improvement in the energy resolution. For example, Fig. 3.20 on the right shows the energy resolution at different γ-peaks before and after the charge trapping correction of a detector. This correction was necessary to achieve the best energy resolution in Majorana Demonstrator.

The ADC non-linearity and charge trapping correction resulted in the best energy performance among current generation experiments. We further improved the energy estimation by improving start time estimation of the waveform. The waveform start time correction reduced the non-linearity in the energy scale, improving the energy parameter, including both low energy and also at higher energy, where the $0\nu\beta\beta$ peak is expected. Figure 3.21 shows the peak position obtained by multi-peak fitting and corresponding residuals in old and new energy estimations. There is a noticeable improvement in the lower energy region.

An excellent energy performance achieved in the Majorana Demonstrator is the result of different analysis efforts and techniques mentioned earlier. These techniques will play an essential role in future experiments like LEGEND to maintain similar energy performance.

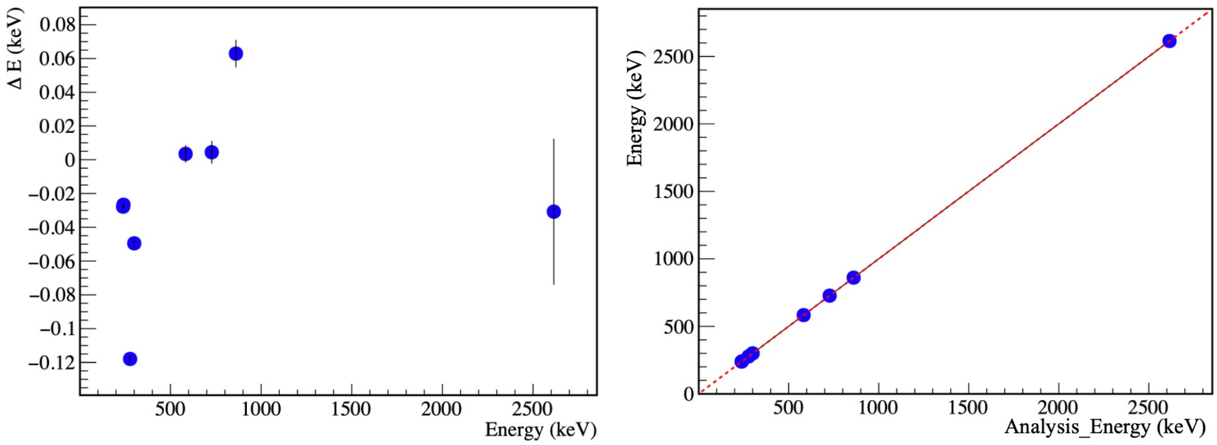

FIGURE 3.16: A combined calibration of a detector in DS5 dataset with quadratic correction to the energy. (Left) Residual in energy between actual energy and energy from the fit. (Right) Linearity between actual energy and energy from the fit.

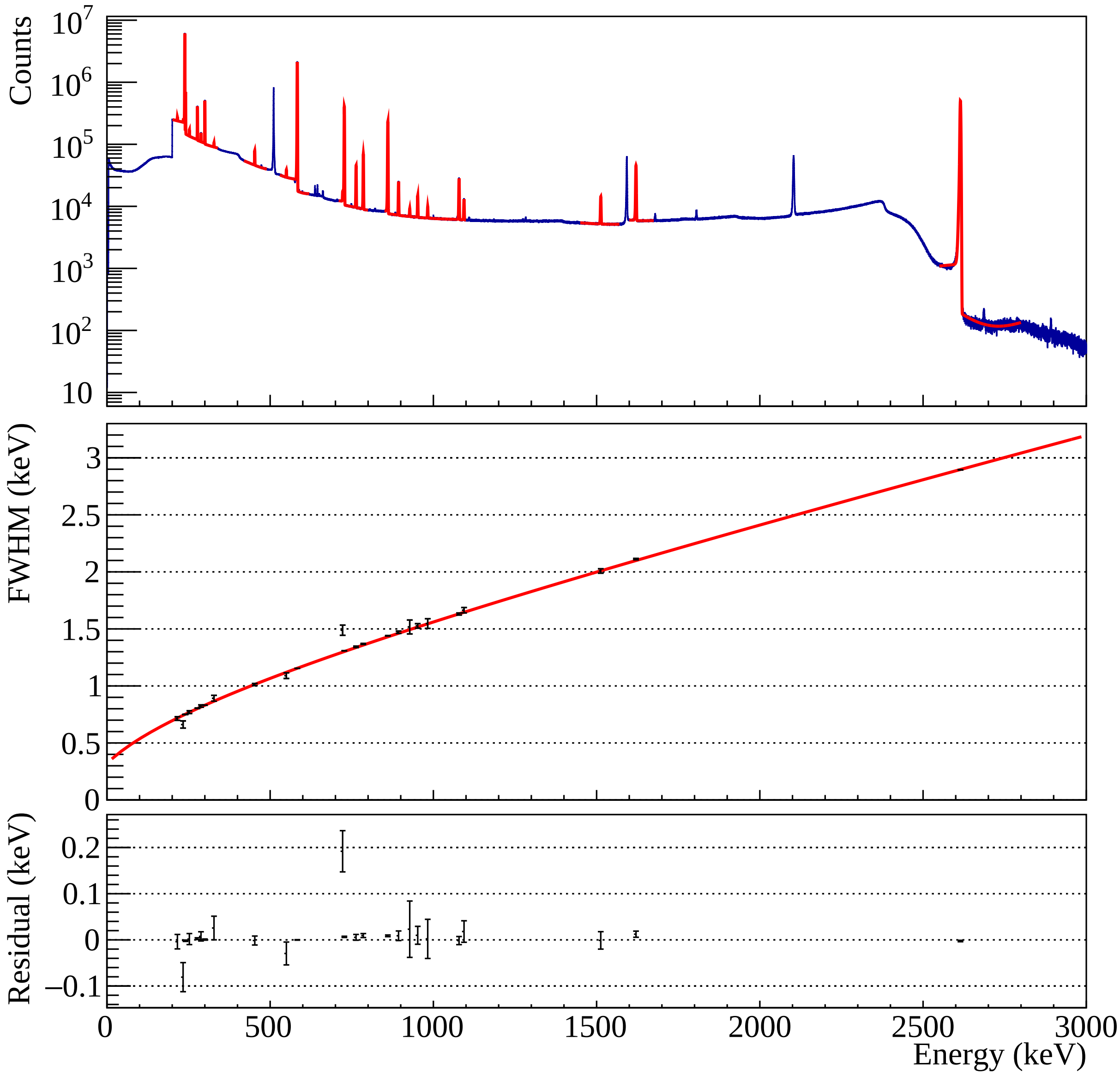

FIGURE 3.17: (Top): The combined energy spectrum of all detectors in dataset DS8. The spectrum shows fits of 24 γ-peaks that were fitted simultaneously. (Middle): FWHM energy resolution fit obtained from the spectral fit of 24 γ-peaks. The fitting function in Eq. 3.15 calculates the FWHM at $Q_{\beta\beta}$ value for $0\nu\beta\beta$ analysis. (Bottom): A second fit was performed on each 24 γ-peaks keeping peak widths parameters floating. The residual values of FWHM energy resolution and uncertainties were calculated. These values were used for the systematic study of errors in energy estimation.

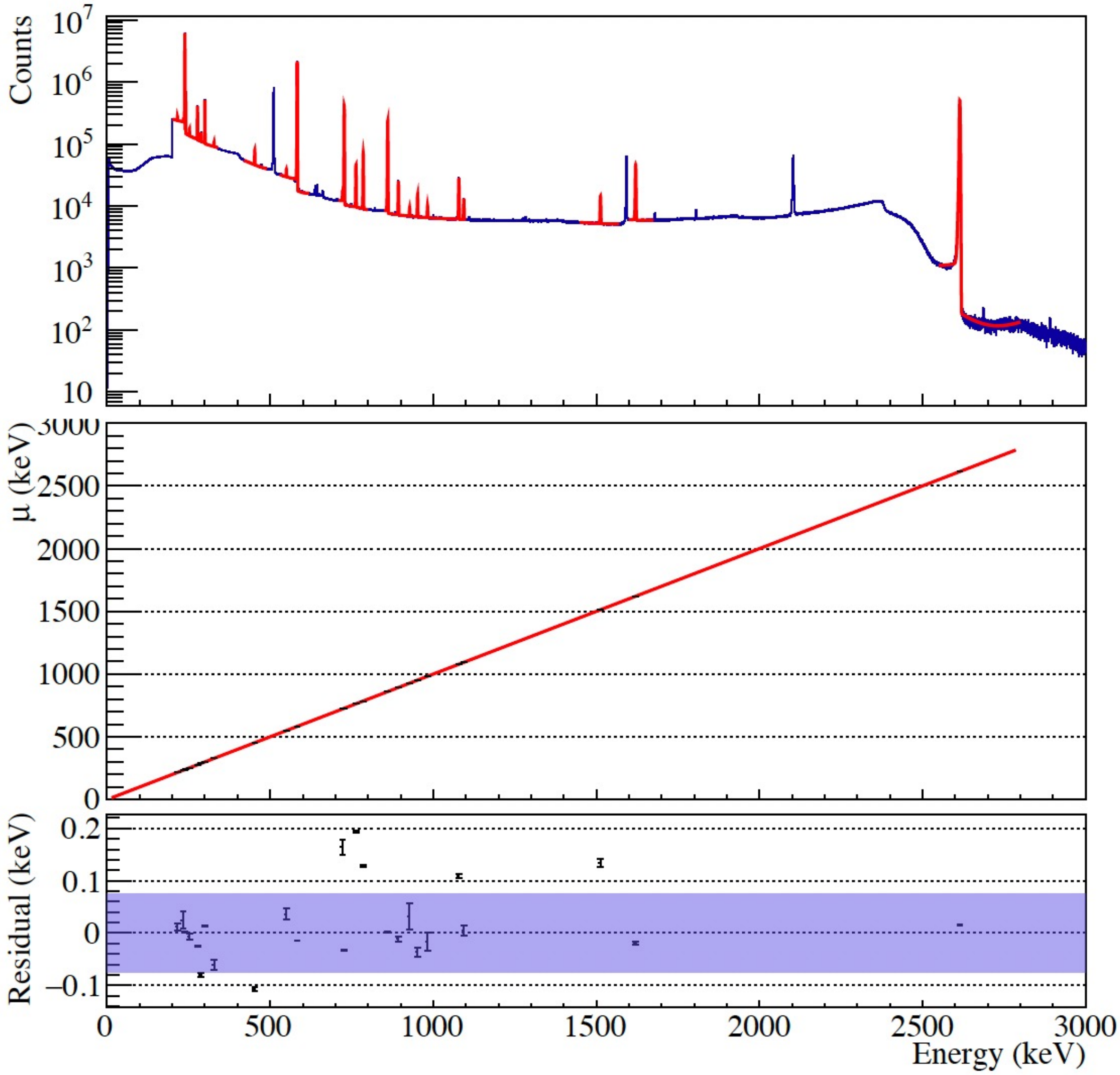

FIGURE 3.18: (Top): The combined energy spectrum of all detectors in the DS8 dataset. The spectrum shows fits of 24 γ-peaks in red that were fitted simultaneously. (Middle) The peak position of 24 γ-peaks from the multi-peak fitting. The function was used to compute each peak's peak position (μ) and at the $Q_{\beta\beta}$ value of $0\nu\beta\beta$ in ^{76}Ge. (Bottom) A second fit was performed, keeping the peak position floating, and computed the residuals and uncertainty in each peak position.

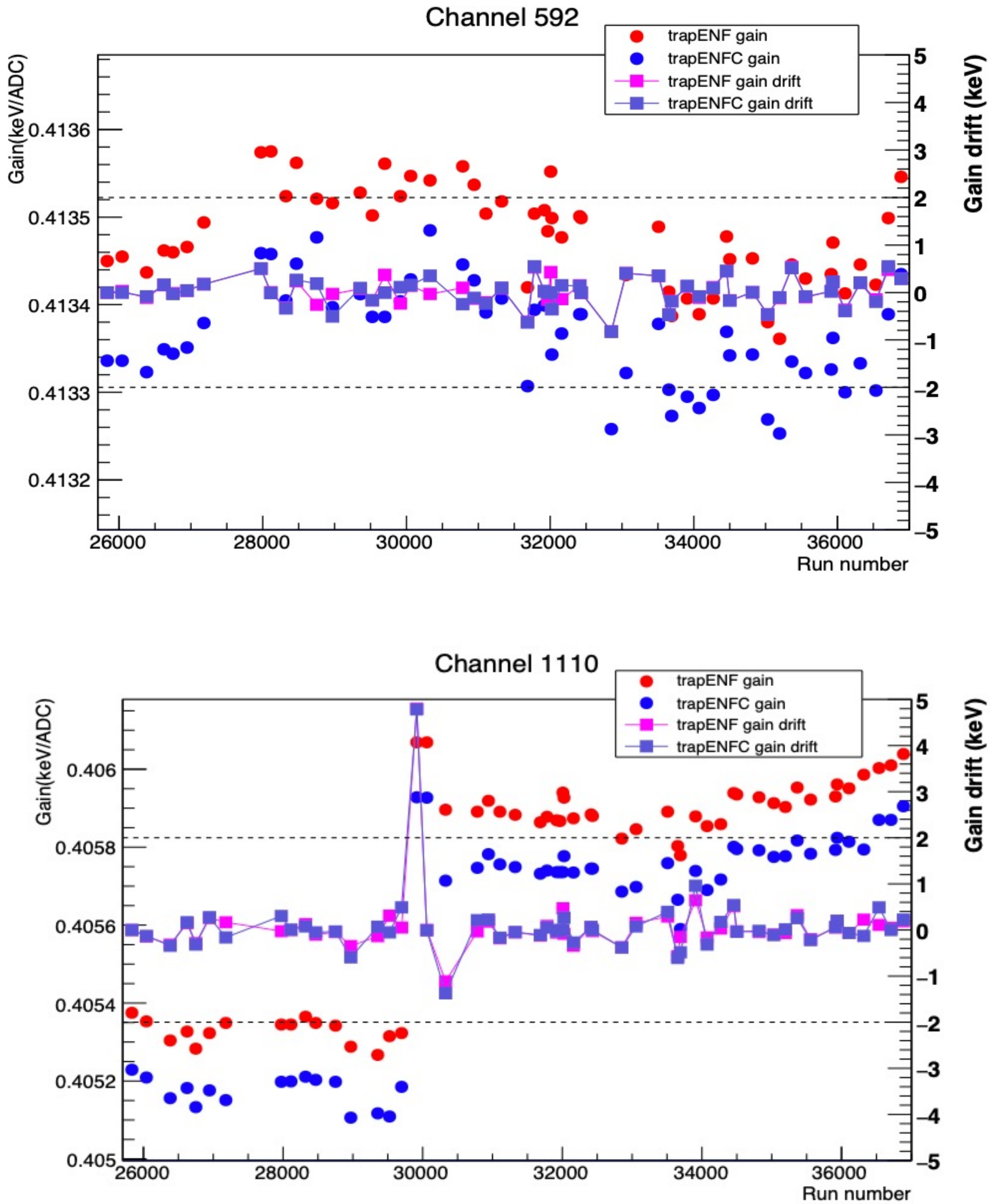

FIGURE 3.19: (Top): The scale parameter and gain drift between weekly calibrations of 2615-keV peak in channel 592 in the DS6a dataset in uncalibrated energies trapENF and trapENFC. Since the gain drift in both energies is smaller than 2 keV, it is regarded as a stable channel for that dataset. (Bottom) A similar plot for channel 1110. It is regarded as a channel with permanent drift in energy observed before and after approximately run 30000. The period where it had drifted more than 2 keV between consecutive calibrations was rejected from the analysis.

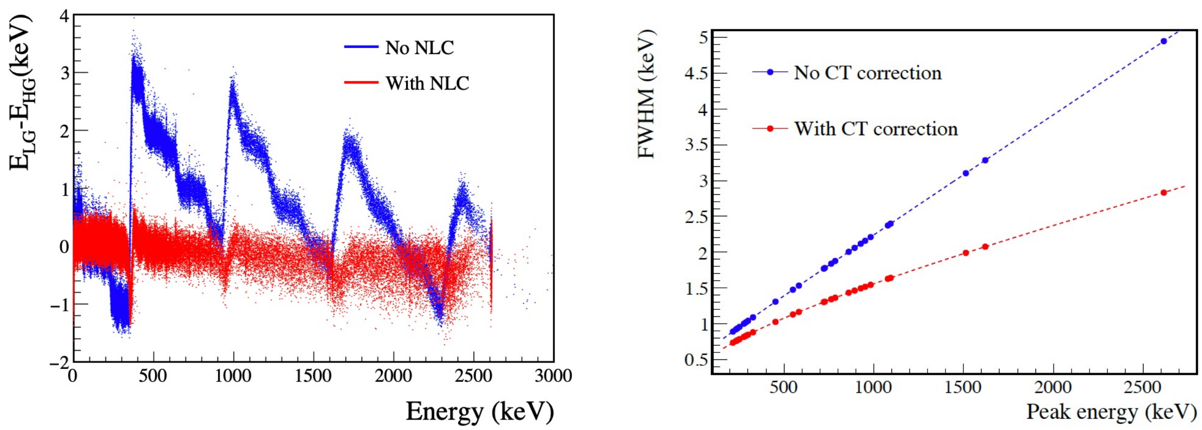

FIGURE 3.20: (Top): Energy difference between high-gain and low-gain channels in a detector before and after non-linearity correction. The significance of this correction is seen in the considerable reduction in the energy difference. (Bottom). After applying charge trapping correction, the energy resolution was improved significantly. On average, the energy resolution was improved by 31%. Adapted from [102].

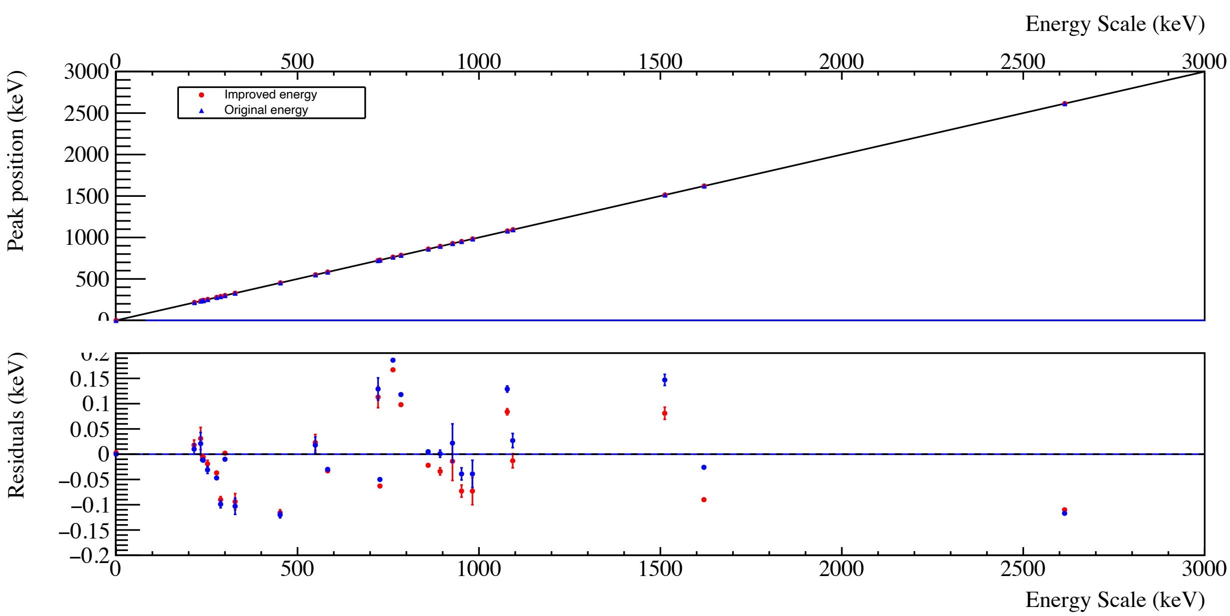

FIGURE 3.21: (Top): Peak position of 26 γ-peaks from the ^{228}Th sources versus energy scale of MAJORANA DEMONSTRATOR for the original energy (blue) and improved energy (red) for the DS6b dataset. (Bottom) Residual of the peak position for the same energy parameters. The improved energy has a mean residual of 0.003 ± 0.02, and the original energy has a residual mean of 0.03 ± 0.02.

4

Study of (alpha, n) Reactions in the MAJORANA DEMONSTRATOR

4.1 Introduction

Neutrons are one of the potential background sources in ultra-rare event search experiments [103–106]. In dark matter experiments looking for WIMPs (Weekly Interacting Massive Particles), neutrons could produce signals that mimic the WIMP signature. In $0\nu\beta\beta$ experiments, neutron captures and delayed decays of reaction products could produce signals in the ROI (region of interest) of $0\nu\beta\beta$. For example, in germanium-based $0\nu\beta\beta$ experiments, neutron captures on ^{76}Ge create ^{77}Ge and ^{77m}Ge isotopes. The β-decay of these isotopes could potentially produce signals similar to $0\nu\beta\beta$ near the $Q_{\beta\beta}$ value of ^{76}Ge.

Radiogenic (α, n) reactions is one common source of neutrons. The reaction may occur within the materials used in the experiments because α-particles are produced from the natural decay of radioisotopes, typically ^{238}U and ^{232}Th, present within the materials. These naturally-occurring isotopes present in detector materials contain several α-emitters, and various α-particles with energies up to 9 MeV are emitted, initiating a range of (α, n) reactions. Even though the cleanest material can be assayed and selected in the experiments, the precise understanding of background contribution due to such neutrons is crucial for the next-generation experiments with a stringent background goal.

α-particles produced from the radioactive decay of radio-isotopes may interact within the materials. Generally, energy of those α-particles should have enough kinetic energy to overcome the

Coulomb barrier of the target nucleus given by Eq. 4.1. The total potential between α-particle and target nucleus is by Eq. 4.1.

$$V = k\frac{2Ze^2}{r_0A^{1/3} + r_\alpha} \tag{4.1}$$

where,

Ze = total charge of the target nucleus

A = atomic mass number of the target nucleus

k = Coulomb's constant

r_0 = constant value

r_α = radius of the alpha particle

Coulomb potential mainly depends on the isotope's atomic number (Z) and atomic mass number (A). However, it is controlled mainly by the Z value implying lighter nuclei are more likely to undergo (α,n) reactions.

α-particles with enough kinetic energy can be captured in the target nucleus and form a compound nucleus. The compound nucleus is an unstable nucleus that might decay to daughter nuclei with probabilities that depend on the compound nucleus's energy state and the daughter nucleus's nuclear structure. In this process, neutrons might be emitted.

The neutron energy spectrum of outgoing (α, n)-neutrons can be explained with simple two-body classical mechanics as given in the SOURCES4C manual [107]. A similar derivation based on two-body kinematics is provided in [108]. Here, we derive an equation to calculate the initial kinetic energy required to excite the compound nucleus to generate excited states of the daughter nucleus using two-body kinematics in classical mechanics based on similar derivations. Figure 4.1 is the schematic of (α, n) reaction seen through a two-body kinematics in classical mechanics.

In Fig. 4.1, applying the conservation of momentum, the velocity of the center of mass, v_c, which is equivalent to velocity of the compound nucleus in the laboratory frame is,

$$v_c = \frac{m_\alpha v_0}{m_\alpha + m_t} \tag{4.2}$$

where,

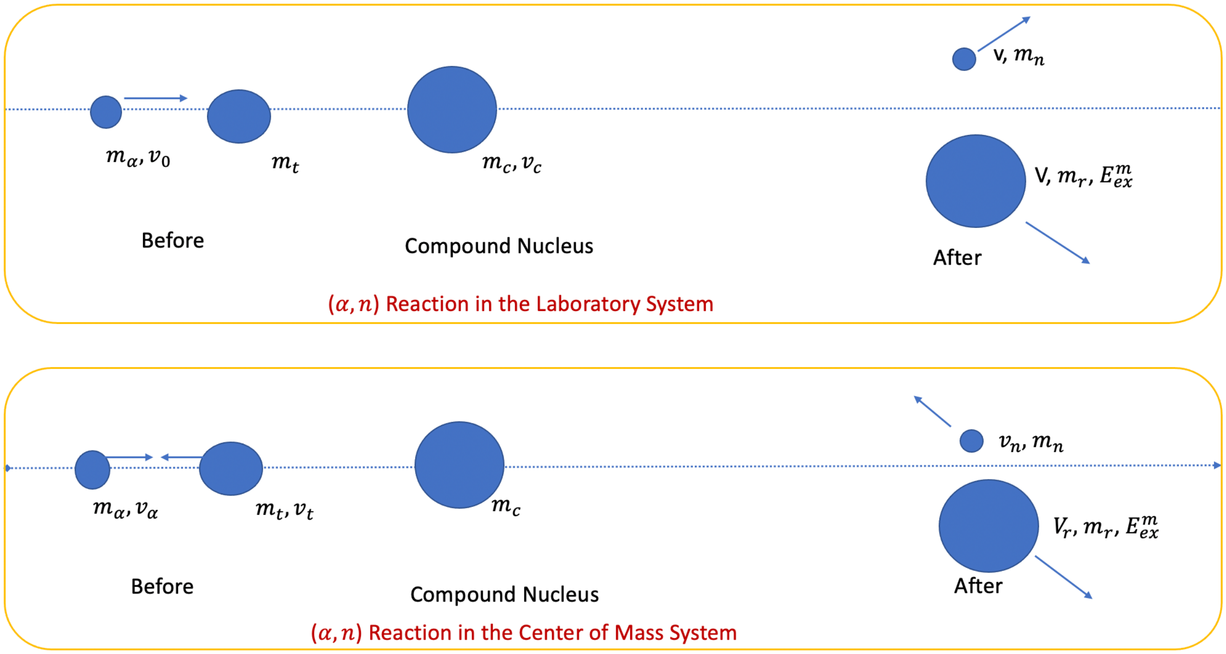

FIGURE 4.1: A schematic of two-body diagrams for the (α, n) reaction in the laboratory frame of reference (Top). The stage before the α-particle is captured and forms a compound nucleus and the decay of compound nucleus to daughter nucleus and neutron. (Bottom) The same decay in the Center of Mass (COM) frame.

m_α = mass of the α-particle

m_t = mass of target nucleus.

v_0 = velocity of α-particle in the laboratory frame of reference, which can be expressed in terms of the kinetic energy of α-particle in laboratory frame, T_α, given as $v_0 = \sqrt{\frac{2T_\alpha}{m_\alpha}}$

The velocity of the α-particle in the COM frame can be derived by subtracting velocity of COM from velocity of α-particle in the laboratory frame of reference.

$$v_\alpha = v_0 - v_c = \frac{m_t v_0}{m_\alpha + m_t} \tag{4.3}$$

and hence the velocity of target in COM is

$$v_t = -\frac{m_\alpha v_0}{m_\alpha + m_t} \tag{4.4}$$

Now, from the conservation of energy in the COM, the kinetic energy of emitted neutron is

$$E_n = (Q - E^m_{ex}) + E_\alpha + E_t - E_r \tag{4.5}$$

where Q is the reaction Q-value, E_{ex}^{m} is the excited state energy level of the recoil nucleus, T_t is the energy of the target, and T_r is the energy of recoil nuclei in COM. Again, the conservation of momentum in the vertical direction gives $v_n = \frac{m_r}{m_n} V_r$. Also, applying energy conservation yields Eq. 4.6.

$$E_\alpha + E_t = T_\alpha \frac{m_t}{m_\alpha + m_t} \tag{4.6}$$

Now putting all in Eq. 4.5, the velocity of neutron in COM becomes

$$v_n = \pm\sqrt{\frac{Q_m}{m_n}\frac{2m_r}{m_r + m_n} + \frac{2T_\alpha}{m_n}\frac{m_t}{m_t + m_\alpha}\frac{m_r}{m_r + m_n}} \tag{4.7}$$

Where, Q_m = (Q - E_{ex}^{m}) is the Q-value of the (α, n) reaction in which the compound nucleus decays to the m^{th} excited state of daughter nucleus. Now, the velocity of neutron in the laboratory frame is

$$v = \left[\frac{m_\alpha}{m_\alpha + m_t}\sqrt{\frac{2T_\alpha}{m_\alpha}} \pm \sqrt{\frac{Q_m}{m_n}\frac{2m_r}{m_r + m_n} + \frac{2T_\alpha}{m_n}\frac{m_t}{m_t + m_\alpha}\frac{m_r}{m_r + m_n}}\right] \tag{4.8}$$

Since the kinetic energy of neutron should be a real number, the radicals of the second term in Eq. 4.8 should be positive, which gives Eq. 4.9.

$$T_\alpha > (E_{ex}^{m} - Q) \times \left(\frac{m_t + m_\alpha}{m_t}\right) \tag{4.9}$$

Equation 4.9 can be used to calculate the minimum initial kinetic energy of α-particle needed to interact with the target nucleus such that the compound nucleus decays to the m^{th} excited state of the daughter nucleus.

4.2 (α, n) Reactions in Calibration Source

The detailed information of the calibration source used in the Majorana Demonstrator is described in Chapter 3. Those calibration sources were made of thoriated epoxy encapsulated in a tube made of PTFE [90]. The epoxy resin and hardener materials, mainly containing carbon, were used to manufacture the calibration line sources. In a private communication, the vendor provided the elemental composition of epoxy resin and hardener needed for the (α, n) analysis.

The calibration source produces several γ-rays, which is very important for the energy calibration, detector characterization, and development of the analysis cuts in the Majorana Demonstrator. However, they also produce several α-particles from the decay chain of ^{228}Th until it reaches a stable isotope ^{208}Pb. Table 4.1 shows some major α-particles in terms of their intensity per ^{228}Th decay which lie between 5.42 MeV and 8.79 MeV. The data in Table 4.1 were taken from Nuclear structure & decay Data (NuDat 3.0)[1].

Table 4.1: Primary α-particles from the decay chain of ^{228}Th in terms of their corresponding intensity normalized with each ^{228}Th decay.

α-particle energy (MeV)	Parent isotope	Intensity (per ^{228}Th decay)
5.423	^{228}Th	0.734
5.340	^{228}Th	0.260
5.685	^{224}Ra	0.949
5.449	^{224}Ra	0.051
6.288	^{220}Rn	0.999
6.778	^{216}Po	0.999
6.050	^{212}Bi	0.090
6.089	^{212}Bi	0.035
8.785	^{212}Po	0.641

Every (α, n) reaction have their associated Q-value and threshold energy needed for α-particle. The α-particle from the decay chain of ^{228}Th can have energy up to 8.78 MeV. Those α-particles can initiate several (α, n) reactions within the calibration source. Some possible (α, n) reactions are ^{13}C$(\alpha, n)^{16}$O, ^{17}O$(\alpha, n)^{20}$Ne, ^{18}O$(\alpha, n)^{21}$Ne, ^{35}Cl$(\alpha, n)^{38}$K, and ^{14}N$(\alpha, n)^{17}$F. Among them the major reaction within the calibration source is ^{13}C$(\alpha, n)^{16}$O based on the percentage and natural abundance of ^{13}C.

4.2.1 $^{13}C(\alpha, n)^{16}O$ Reaction

In ^{13}C$(\alpha, n)^{16}$O reactions, an α-particle from the calibration source can be captured in ^{13}C to form the compound nucleus ^{17}O*. The compound nucleus of ^{17}O then decays to the ground state or excited states of ^{16}O by emitting a neutron. Figure 4.2 shows the simplified level scheme of different states of ^{16}O that can be populated. If any excited state of ^{16}O is populated, they deexcite to the ground state by giving secondary particles depending on the selection rule. For example, the decay

[1] https://www.nndc.bnl.gov/nudat3/

of first excited state ($J^\pi = 0^+$) deexcites with e$^+$e$^-$ pair while the second excited state ($J^\pi = 3^-$) decays to the ground state via 6129-keV γ-ray emission.

$$
\begin{aligned}
{}^{13}\mathrm{C} + \alpha &\rightarrow {}^{17}\mathrm{O}^* \\
&\rightarrow {}^{16}\mathrm{O}^*(3^-) + \mathrm{n} \qquad (4.10)\\
&\rightarrow {}^{16}\mathrm{O(g.s.)} + \gamma\ (6129\ \mathrm{keV}) + \mathrm{n}
\end{aligned}
$$

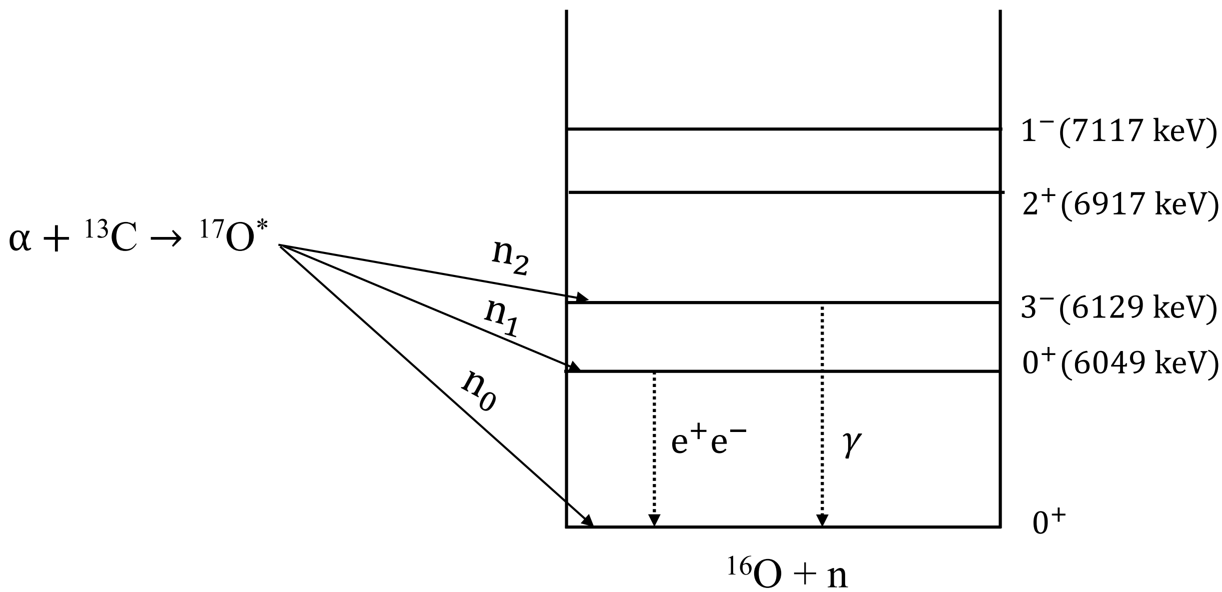

FIGURE 4.2: The ^{16}O level scheme as populated in the ^{13}C$(\alpha, n)^{16}$O reaction (energy not to scale) simplified from Figure 1 of Ref. [106]. The numerical index of the emitted neutrons n_0, n_1, n_2 represents which state in ^{16}O is populated. Due to selection rules, the 0^+ (6049 keV) state deexcites via the emission of an e$^+$e$^-$ pair, while the 3^- (6129 keV) state deexcites through γ-ray emission. Data from [106, 109].

.

In low-background experiments, different plastics are widely used, *e.g.*, for neutron shielding and electrical insulation. In such experiments, ^{13}C$(\alpha, n)^{16}$O is the primary source of neutrons. Furthermore, in liquid scintillator-based neutrino experiments, this reaction is the primary source of background [106, 110]. For example, in KamLAND, this reaction can mimic inverse beta decay signals where the α's come from the decay of ^{210}Po, and the neutrino oscillation parameters extracted require detailed knowledge of the ^{13}C$(\alpha, n)^{16}$O cross-section. Therefore, a precise cross-section measurement is needed to understand the background contribution in such low-background experiments.

Besides its role as a background in low-background rare-event searches, $^{13}C(\alpha,\ n)^{16}O$ is important in nuclear astrophysics. This reaction is considered the most important neutron source for developing the s-process nucleosynthesis in low-mass asymptotic giant branch stars [111–114]. Direct measurements of $^{13}C(\alpha,\ n)^{16}O$ reaction have been a focus of many experimental efforts, and there have been many studies performed in the α-particle energy range less than about 5 MeV. These cross-section measurements at lower energy agree reasonably well between different efforts [115–119]. With a 3.5 MV accelerator upgrade, LUNA (Laboratory for Underground Nuclear Astrophysics) plans to study $^{13}C(\alpha,\ n)^{16}O$ in a wide energy range that is critical for the s-process [120]. However, at higher α energies above 5 MeV, precise cross-section measurements are sparse and have some disagreement [119, 121]. Therefore, a precise cross-section measurement until 9 MeV is necessary to understand and estimate the radiogenic neutron background in low-background experiments.

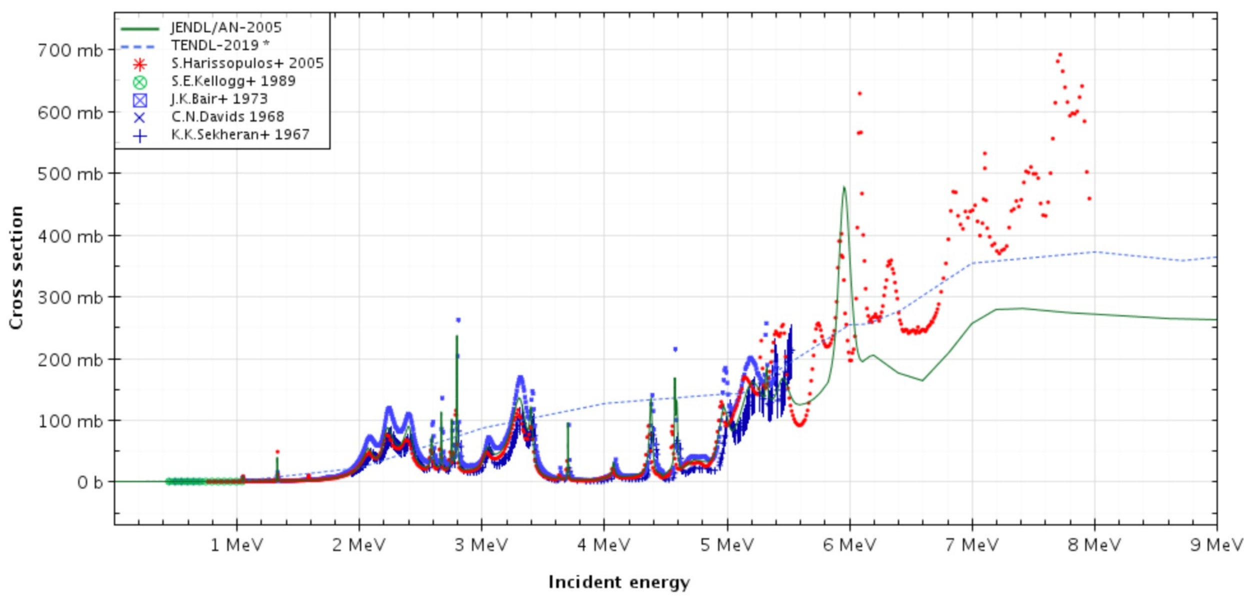

FIGURE 4.3: cross-section measurement of $^{13}C(\alpha,\ n)^{16}O$ reaction between different efforts. At lower energy, approximately below 5 MeV, the measurements agree reasonably well. This plot is adapted from JANIS database (`https://www.oecd-nea.org/janisweb/book/alphas/C13/MT4/renderer/14`).

In addition to the measured data, one can rely on a statistical model approach such as nuclear reaction code TALYS [122] which links to the TALYS-generated Evaluated Nuclear Data Libraries (TENDL) database to merge the nuclear model with data available in the Japanese Evaluated Nuclear Data Library (JENDL) [103] and Evaluated Nuclear Data File (ENDF) [123]. However, such a statistical model lacks resonance structure in the cross-section, as pointed out by Ref. [106] and provides only the approximate result. Therefore, TALYS-calculated cross-section could be more valuable for understanding radiogenic neutron background in low-background experiments, especially when the direct measurement is unavailable when their validity is studied with the experimental measurement.

Figure 4.4 shows the partial cross-section, (α, n_j), where j identifies the neutrons associated with different states of ^{16}O and the total cross-section of (α, n) reaction as a function of initial kinetic energy of α-particle. If the energy of α-particle is approximately above 5 MeV, the higher energy states of ^{16}O are populated, among which the second excited state ($J^\pi = 3^-$) is favored most. Also, approximately above 6 MeV of α-particle energy, the second excited state is favored among all possible states. Since the α-particle from the ^{228}Th decay chain can have energy up to 8.78 MeV, all four excited states can be populated, and the 6129-keV γ is the signature to look in the calibration data.

The neutron yield from the (α, n) reactions can be estimated with the NeuCBOT (Neutron Calculator Based On TALYS) [124, 125]. It accumulates the ENSDF (Evaluated Nuclear Structure Data Files) [126] for the nuclear decay information and SRIM-generated stopping powers of α particles for each element in the material [127]. TALYS uses the nuclear structure of the target and the daughter nucleus to predict the cross-section of forming different possible excited states. It assumes the thick target such that α-particles are captured within the materials they produce. The detail derivations of how neutron yield is calculated is described in Ref. [124] which we have briefly summarized here. The neutron yield with energy E$_n$ from a given α-particles with initial energy E$_\alpha$ from the i^{th} isotope in the composite material is calculated based on Eq. 4.11.

$$Y_i^\alpha(E_n) = C_i \frac{S_i(E_\alpha^{'})}{S(E_\alpha^{'})} y_i^\alpha \tag{4.11}$$

where,

N_A = Avogadro's number

C_i = mass fraction of i^{th} isotope in the composite material

A_i = mass number of the i^{th} isotope

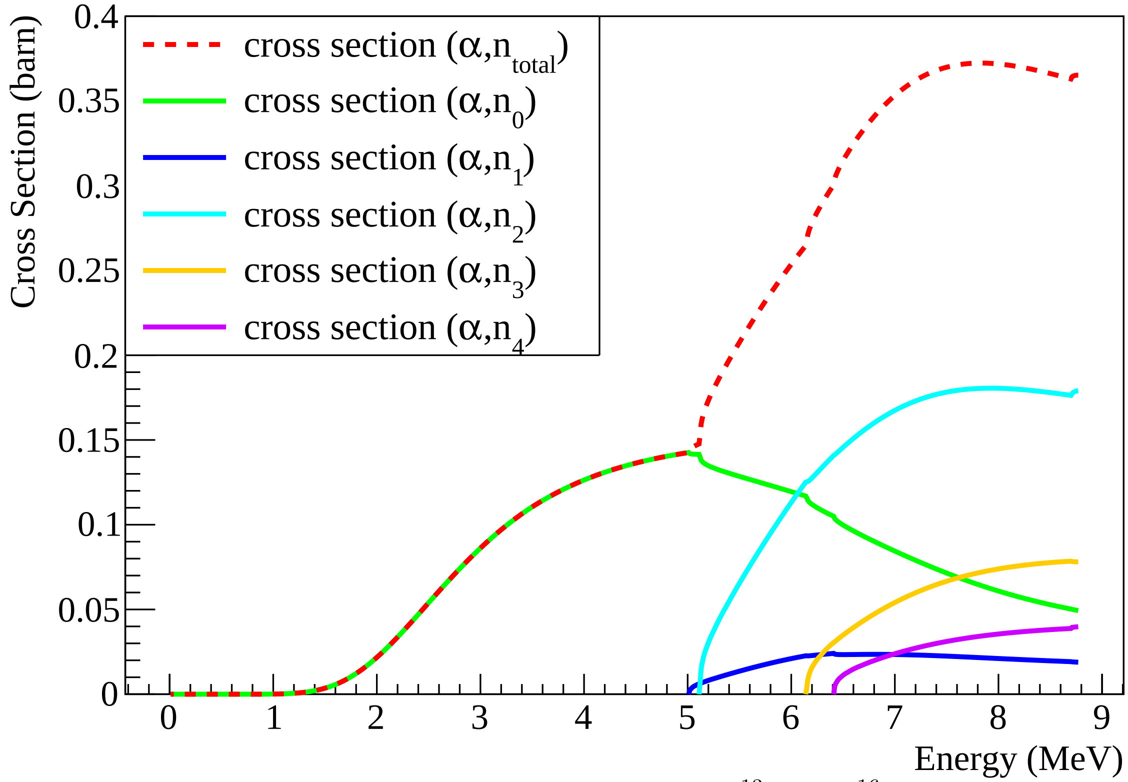

FIGURE 4.4: Partial and the total cross-sections of the ^{13}C$(\alpha, n)^{16}$O reactions as a function of incident α-particle energy available from the decay chain of ^{228}Th for different (α, n_j) channel as shown in Fig. 4.2. The cross-sections These cross-sections are generated by TALYS-1.95 and show that higher excited states of ^{16}O are populated when the initial kinetic energy of α-particle is approximately above 5 MeV. The results of this new TALYS version are consistent with branching ratios obtained from Ref. [109] that used TALYS-1.8.

$S_i(E_\alpha^{'})$ = stopping power of i^{th} isotope for an α-particle with energy $E_\alpha^{'}$

$S(E_\alpha^{'})$ = total stopping power from all isotopes present in the material for an α-particle with energy $E_\alpha^{'}$

y_i^α is the neutron yield if the material purely contains i^{th} isotope which is given by Eq. 4.12

$$y_i^\alpha = \frac{N_A}{A_i} \int_0^{E_\alpha} \frac{\sigma_i(E_\alpha^{'}, E_n)}{S(E_\alpha^{'})} dE_\alpha^{'} \tag{4.12}$$

If multiple α-emitters are present in the materials, the total neutron yield with energy E_n is based on the branching ratios of each α-decay within the materials. In NeuCBOT, Eq. 4.13 is used to calculate the neutron yield and the neutron energy spectra.

$$Y(E_n) = \sum_{\alpha}\sum_{i} P_\alpha Y_i^\alpha(E_n) \tag{4.13}$$

P_α is the probability of the α-particle appearing in the decay chain of the α-emitter.

4.3 Background Estimation for $0\nu\beta\beta$ Search

In germanium-based $0\nu\beta\beta$ experiments, neutrons from the (α, n) reactions can be captured in ^{76}Ge and produce ^{77}Ge isotopes. The cross-section of neutron capture in ^{76}Ge is well measured in Ref. [128]. The excited states then decay to either ground state of ^{77}Ge, or metastable state, *i.e.* ^{77m}Ge. Both ground state and metastable states undergo β decay and produce ^{77}As. Figure 4.5 shows the decay scheme of ^{77}Ge and ^{77m}Ge. Since the Q-value of these decay is greater than the $Q_{\beta\beta}$ of germanium, the decay can produce events that span over ROI of $0\nu\beta\beta$. Furthermore, the β decay can produce events that look similar to $0\nu\beta\beta$ and could result in a false positive. The signatures of such events have been studied in Refs. [80, 129].

In Majorana Demonstrator, calibration sources are parked entirely out of the shield after finishing the weekly calibration data-taking. Therefore, only the neutrons produced from the (α, n) reactions in the source during the calibration data-taking period could contribute to the background for $0\nu\beta\beta$ search. The calibration data-taking period is around 1.5 to 2 hours in weekly calibrations. Therefore, the production of short-lived isotope ^{76}Ge (half-life: 53.7 s) is less of a concern. However, the long-lived isotope of ^{77}Ge (half-life: 11.3 h) decays entirely in the $0\nu\beta\beta$ data-taking following the calibration. Therefore, the main concern is the production of the ground state of ^{77}Ge. The background contribution for the $0\nu\beta\beta$ search is estimated based on the combination of NeuCBOT and MaGe tools.

4.3.1 Neutron Yield using NeuCBOT

The neutron yield from all possible (α, n) reactions in the calibration source is estimated using NeuCBOT. The chemical composition of epoxy resin and hardener is used according to the vendor-reported values provided in private communication. The NeuCBOT gives the energy and corresponding yield of outgoing neutrons with 100 keV binning. Figure 4.6 is the outgoing neutron

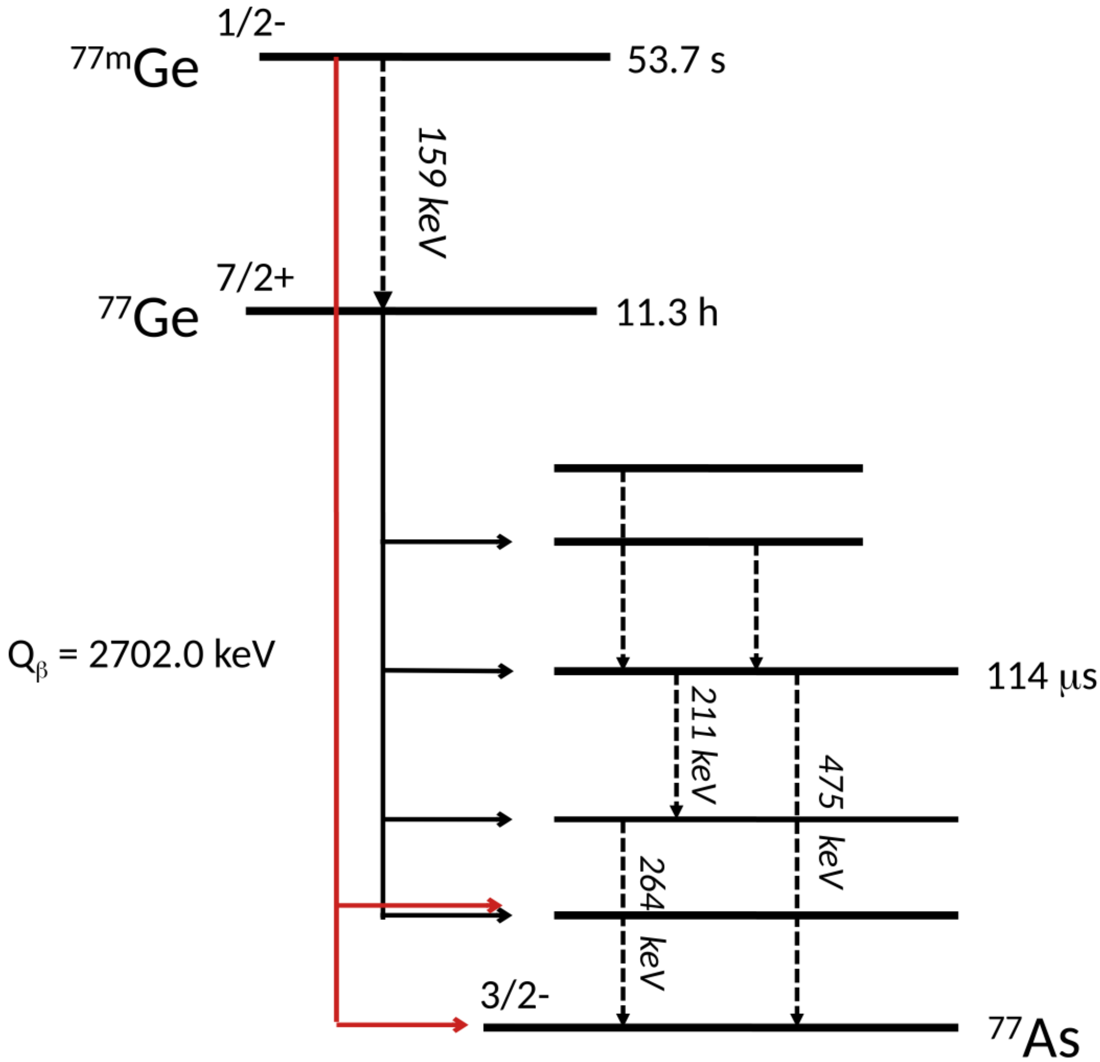

FIGURE 4.5: The schematic of the decay scheme of ^{77}Ge and ^{77m}Ge adapted from Ref. [80]. These isotopes undergo β decay to ^{77}As. The ^{77m}Ge mainly decays to the ground state of ^{77}As without any additional γ-rays while the ^{77}Ge could decay to higher excited states of ^{77}As, the decay of which could produce some additional γ signatures.

energy spectra from (α, n) reactions in the calibration source. The major contributor to the neutron yield is the $^{13}\text{C}(\alpha, n)^{16}\text{O}$ reaction. The average neutron yield is found to be 2.26×10^{-6} neutron/decay.

4.3.2 Simulation for Background Estimation using MaGe

The neutrons produced from the (α, n) reactions with energy and corresponding yields are isotropically distributed in the calibration track of each module. The simulation is performed using

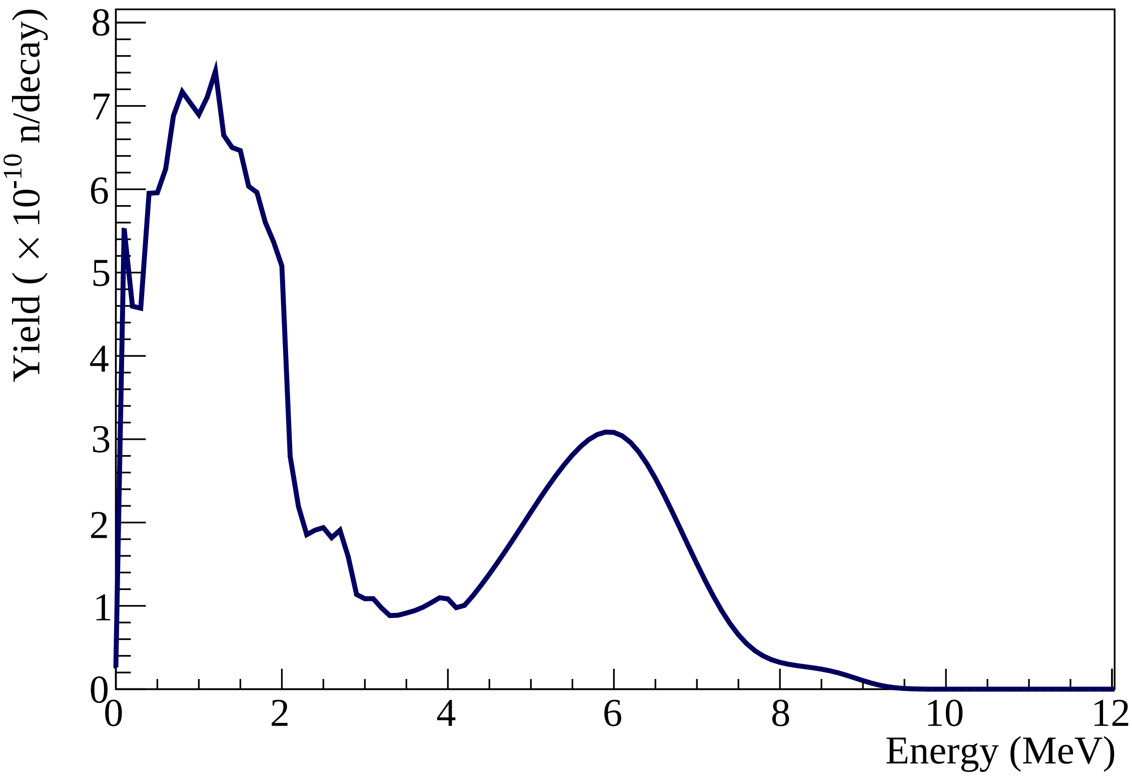

FIGURE 4.6: Neutron energy spectrum from all possible (α, n) reactions in the calibration source. TALYS-1.95 generated cross-section data for each element present in the source is used. The unit of yield refers to the per decay of ^{228}Th. The neutron energy and corresponding yield are obtained from NeuCBOT.

GEANT4-based [130] simulation package, MAGE [131]. The number of ^{77}Ge produced during calibration in each dataset is counted based on the yield, source activity, efficiency, and calibration time. The efficiency is estimated based on a total number of neutrons simulated and the number of ^{77}Ge produced in active detectors in each dataset. The total number of ^{77}Ge produced in enriched active detectors is found to be 11, which translates to a production rate of 0.24 nuclei/kg-yr using DS0 through DS6c exposure.

The background contribution for the $0\nu\beta\beta$ is estimated based on the number of events observed in the 400 keV background window, which is 200 keV around $Q_{\beta\beta}$ value (2039 keV) in germanium. First, we simulate the ^{77}Ge isotopes distributed in the germanium detectors of MAJORANA DEMONSTRATOR using MAGE. Then, we obtained the energy spectra from the energy deposition in a single detector (hit energy) from the decay of ^{77}Ge inside the detectors. Figure 4.7 is the hit energy spectrum obtained based on active enriched detectors in the MAJORANA DEMONSTRATOR. The background index (BI) based on the events in the 400 keV window and total exposure of data used for this analysis ($\sim$ 46 kg-yr) is estimated to be 2.01×10^{-5} cts/(keV-kg-yr) before any analysis cuts. This background is negligible compared to the measured background in the MAJORANA DEMONSTRATOR. In the Phase I data-taking, the GERDA experiment also investigated similar background contribution [132] from neutrons produced from the calibration source. They minimized this background by using a different calibration source made by encapsulating thorium by gold to reduce the neutron flux. A similar calibration source design is adapted for LEGEND [52]. In addition to the calibration source, future low-background experiments with a stringent background goal should be aware of (α, n) neutrons during material selection to avoid possible background from radiogenic neutrons.

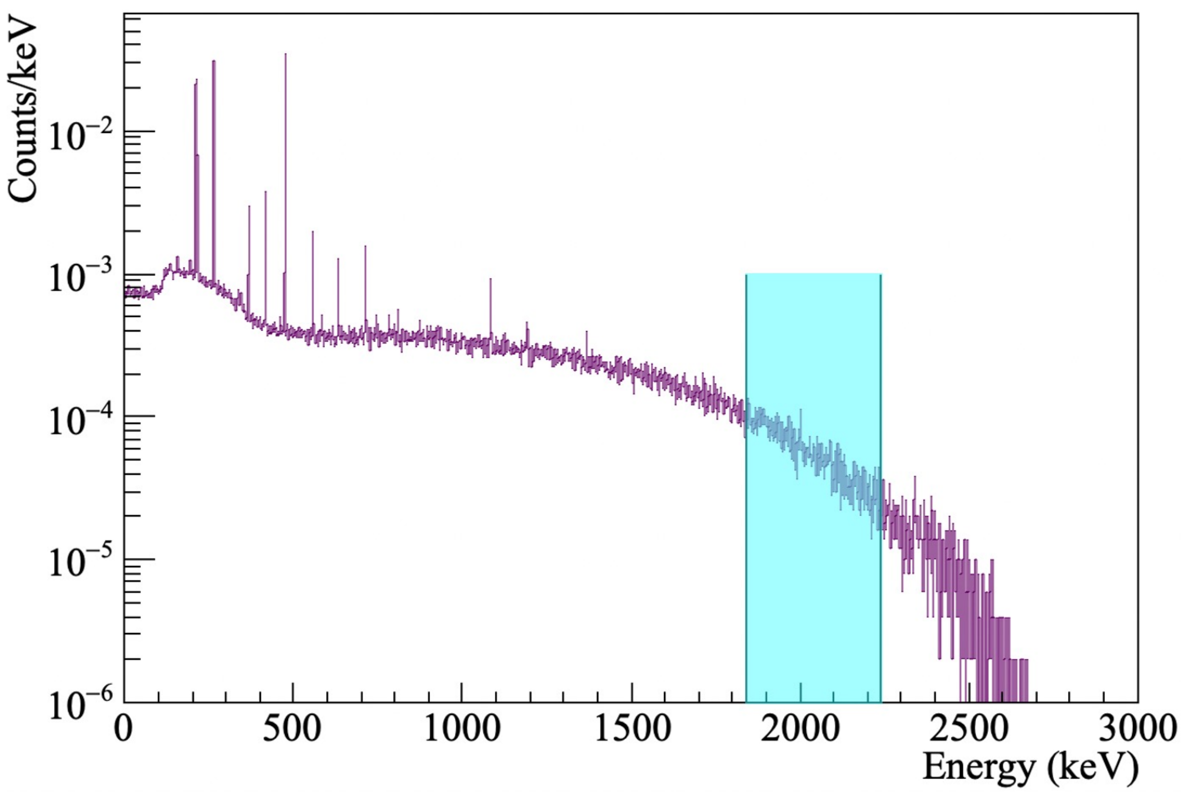

FIGURE 4.7: Normalized hit energy spectrum per ^{77}Ge nuclei decay in the MAJORANA DEMONSTRATOR. The shaded colored region is a 400 keV background estimation window, which spans from 1839 to 2239 keV.

5

^{13}C$(\alpha, n)^{16}$O Measurement in Majorana Demonstrator

In the Majorana Demonstrator calibration source, ^{13}C$(\alpha, n)^{16}$O reaction could produce 6129 keV isomeric photons, which are the signature to search for in the calibration data. Therefore, we used the weekly calibration data and analyzed it in several steps, including data selection, data quality checks, validation of simulation performed in MaGe, signature search, and comparison with NeuCBOT prediction. These steps are described individually in the following sections, and this analysis is published in [81].

5.1 Data Selection

The weekly calibration data taken with ^{228}Th line sources were used for the isomeric photon analysis. Each calibration source was deployed into the corresponding module's track separately for most of the times in the Majorana Demonstrator's calibration data. However, during specific periods, mainly after the installation of the second module, two sources were deployed simultaneously to calibrate both modules. During that period, the throughput of the DAQ can be saturated, and events could be lost. Therefore, this analysis uses the calibration data taken when one source was deployed at a time. Also, early commissioning data is not used either due to evolving issues of the calibration procedure. For example, during DS0 data-taking, transition runs during which the source is in the motion were not tagged, which created uncertainties in analysis time boundaries. The calibration data with a GAT revision tag used for the analysis are summarized below. GAT revision refers to the data processed with different version of analysis software (Germanium Analysis Toolkit).

- DS1: With tagged GAT revision **GAT-v02-07**
- DS2: With tagged GAT revision **GAT-v02-07**
- DS5ab: with tagged GAT revision **GAT-v02-07**
- DS6a: Run from **35938-37086** with tagged GAT revision **GAT-v02-07**
- DS6b: With tagged GAT revision **GAT-v02-07**
- DS6c: With tagged GAT revision **GAT-v02-07**

The MAJORANA DEMONSTRATOR DAQ system records waveforms from each detector through two digitization channels with different amplifications. The high-gain channel has better noise characteristics at lower energy and is used extensively for double-beta decay searches [55]. However, the high-gain channels are saturated around 3-4 MeV. On the other hand, low-gain channels have a more comprehensive dynamic range and saturate around 10 MeV, allowing the study of higher energy signatures *e.g.* by cosmic ray reactions or neutrons. We used the low-gain channel data for the analysis of the 6129 keV signature in the $^{13}\mathrm{C}(\alpha, n)^{16}\mathrm{O}$ reaction.

5.2 Data Quality Check and Run Selection

The primary data cleaning cuts that are used for any physics analysis in the MAJORANA DEMONSTRATOR are also used for this analysis. For example, !wfDCBits cut removes any bad waveform, !muVeto cut removes any events tagged with muon veto signal, and !isGood cut is applied to reject any bad channel data during a specific period. Additionally, we applied run selection based on the rate of 2615 keV γ-ray events. The method applied for the run selection is described in the following subsections 5.2.1 and 5.2.2.

5.2.1 Rate of 2615-keV γ-ray Events

The β^- decay of ^{208}Tl produces 2615 keV γ-rays, the most prominent γ-peak in the calibration data. The branching ratio of this decay in the ^{228}Th decay chain is 35.9%. Since the activity of the calibration source decays exponentially with time, the rate of 2615 keV γ-rays events is also expected to decrease exponentially. Therefore, the calibration runs with a rate significantly deviated from the expected value could have some underlined issues and should be removed from the analysis. For example, such deviation could occur in the runs during which nitrogen dewars were filled because the flow of liquid nitrogen induces noise. The rate of events in each weekly calibration was calculated based on the Eq. 5.1.

$$R = \frac{C}{T \times \epsilon} \tag{5.1}$$

where,

C = Number of 2615 keV events in the ± 5 keV window

T = Live time of each weekly calibration

ϵ = Efficiency of detecting full energy peak of 2615 keV photons in the MAJORANA DEMONSTRATOR detectors in each weekly calibration.

The region of interest for the 2615 keV photons was defined as ± 5 keV based on the energy resolution of detectors in that energy region. The number of 2615 keV events in terms of $Final\_Energy$ energy parameter that pass the basic data cleaning cut mentioned in Section 5.2 in the low-gain channel data in each calibration run were evaluated. The livetime of each calibration run was evaluated using official livetime and exposure code `ds_livetime.cc`. If the livetime of the run is less than 2 min and more than 30 min, those runs were removed from the analysis to avoid short transition runs, and long calibrations run. The total counts and livetime for each weekly calibration were then calculated using the values from each run.

Efficiency Estimation for each Weekly Calibration

The efficiency of detecting full energy events of 2615 keV γ-rays was estimated based on the simulation performed in MAGE. At first, one million such photons were isotropically populated in each calibration track of the modules. The simulation output saves many parameters, including hit energy, event energy, detector id, and waveform id. The hit energy refers to the energy deposited in a detector from a single hit, and the event energy refers to the sum of hit energies if they are within 4 μs time window. Figure 5.1 shows the combined hit energy spectrum from all the detectors in M1 and M2 modules when the 1 million photons of energy 2614.5 keV are populated in the calibration track of the M1 module.

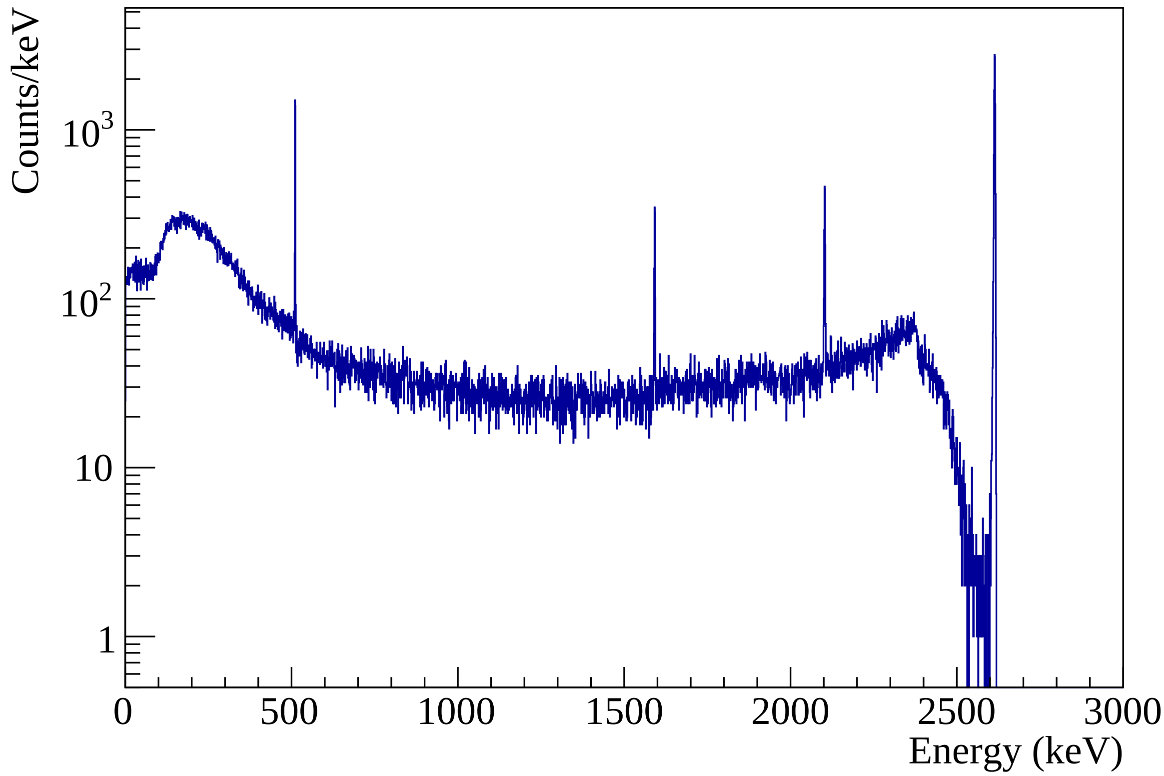

FIGURE 5.1: Hit energy spectrum from the simulation of 1 million 2615 keV γ-rays populated in the calibration track of the M1 module. The spectrum shows the full energy peak at 2615 keV, its single escape and double escape peaks at 2103.5 keV and 1592.5 keV, respectively. Also, the peak at 511 keV due to electrons is seen as expected.

In MAJORANA DEMONSTRATOR, some detectors were disabled and not used for data-taking for some period. Also, suppose the detector has some instabilities in parameters *e.g.* AvsE, DCR, and energy, for a certain period. In that case, they are channel-selected and not used in any physical analysis. As a result, each calibration might have different sets of active detectors. Therefore, efficiencies in each weekly calibration were estimated based on the number of full energy events observed in the region of interest from the active set of detectors in the respective calibration. The region of interest was taken as $\pm$ 5 keV window around the full energy peak. Figure 5.2 shows the efficiencies of detecting 2615-keV events in the MAJORANA DEMONSTRATOR when they are populated in the calibration tracks of M1 and M2 modules. The M1 module has more detectors, resulting in a higher average value of efficiency from its calibration track.

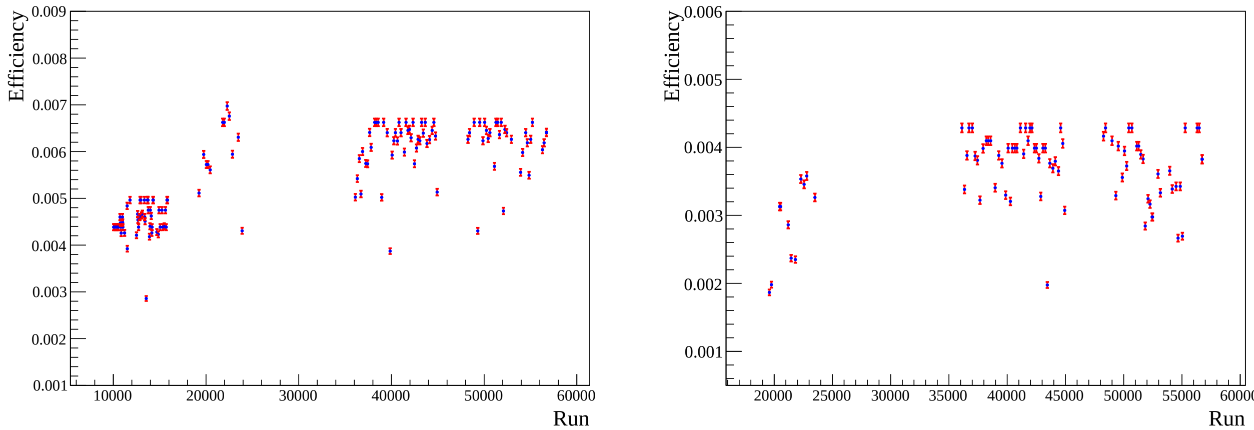

FIGURE 5.2: (Left): Efficiency of detecting full energy events of 2615-keV γ-rays when the source is deployed in calibration track of M1 module. Each data points represent the efficiency of that weekly calibration. The run number in the X-axis corresponds to the first run of each weekly calibration. (Right): The similar plot when the source is deployed in the calibration track of the M2 module.

The rate of 2615 keV events was calculated for each weekly calibration using Eq. 5.1. The rate values of each calibration in each dataset were fitted with an exponential function. The decay term of the exponential function (P_1) was fixed to $1.15e^{-08}$ and kept the offset parameter floating. The decay term was calculated based on the half-life of the ^{228}Th source, which is 1.912 years. Figure 5.3 shows such a fitting applied to the DS6 data when the source was deployed for M1 module calibration. A good Chi-Square value in the fit represents that the decaying source activities are correctly reflected in the actual data. A similar rate was also checked for individual channels in each dataset to ensure no abnormal rate was seen in any channel. However, we have not included that study here because we did not use a channel-by-channel rate study for the run selection.

5.2.2 Run Selection Criteria

The parameters $p0$ and p_1 were extracted from the fitting of each dataset. Since the p_1 represents the real decay term of the source activity, we used Eq. 5.2 to calculate the expected rate of each calibration run. The observed rate of each calibration run was calculated using Eq. 5.1. The ratio between R_{obs} and R_{fit} is expected to be close to 1 with some uncertainties. Hence, ratios were expected to follow a Gaussian distribution with a mean close to 1 and some σ. Figure. 5.4 is such distribution for DS6 dataset. The distribution was fitted with a Gaussian function with both mean and sigma floating. If the rate is outside 3.5 σ, the run was rejected from the analysis. The 3.5 σ was

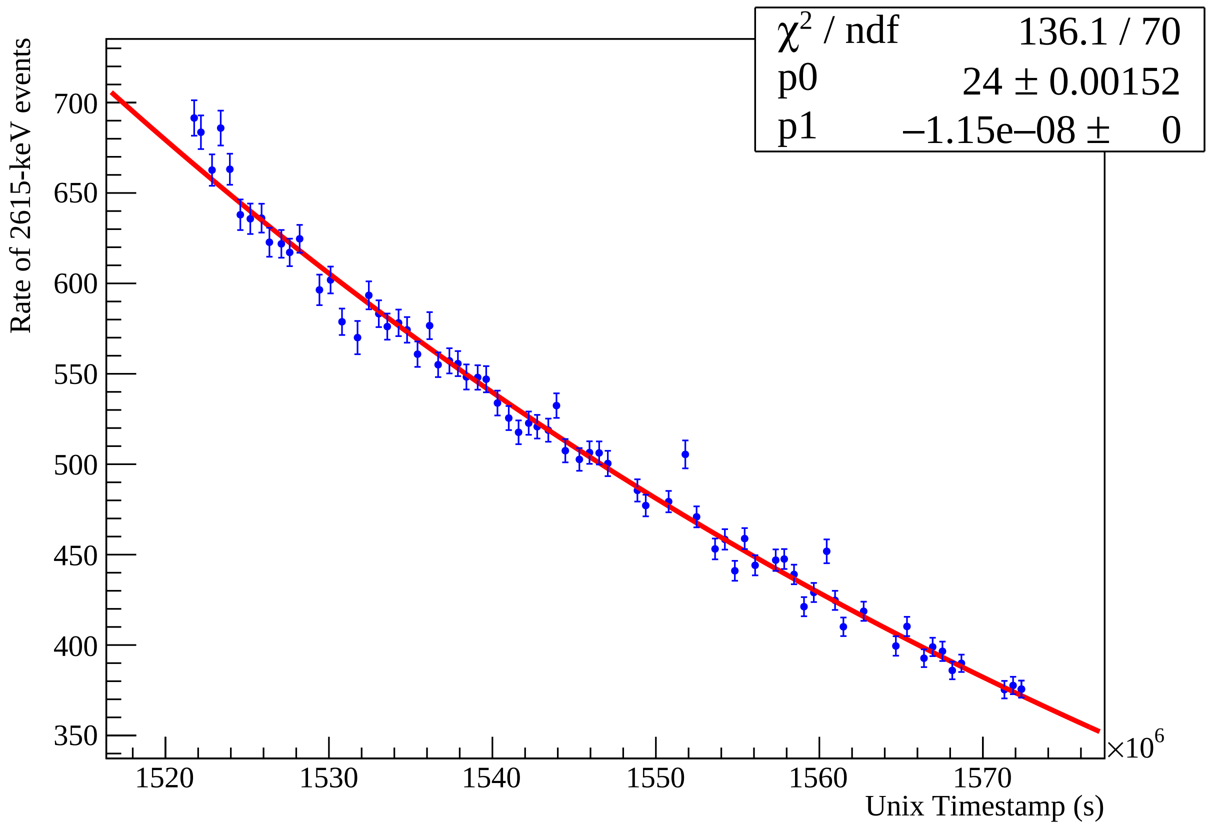

FIGURE 5.3: Rate of 2615-keV events in DS6 dataset with a calibration source deployed in M1 module. Each data point refers to the weekly calibration, and the uncertainty associated with each data point is the statistical uncertainty. The data were fitted using an exponential function with a fixed decay parameter (p_1) and a floating offset parameter (p_0) . The slope parameter is calculated based on the half-life of the calibration source, which is 1.912 years.

chosen based on the corresponding exposure lost for the analysis. For example, this cut removed about 0.7% exposure in the DS6 dataset. This additional run selection was applied to analyze 6129-keV isomeric γ-rays in the calibration data.

$$R_{fit} = e^{p_0 + p_1 t} \tag{5.2}$$

where,

R_{fit} = Rate of each calibration run based on the fit parameters

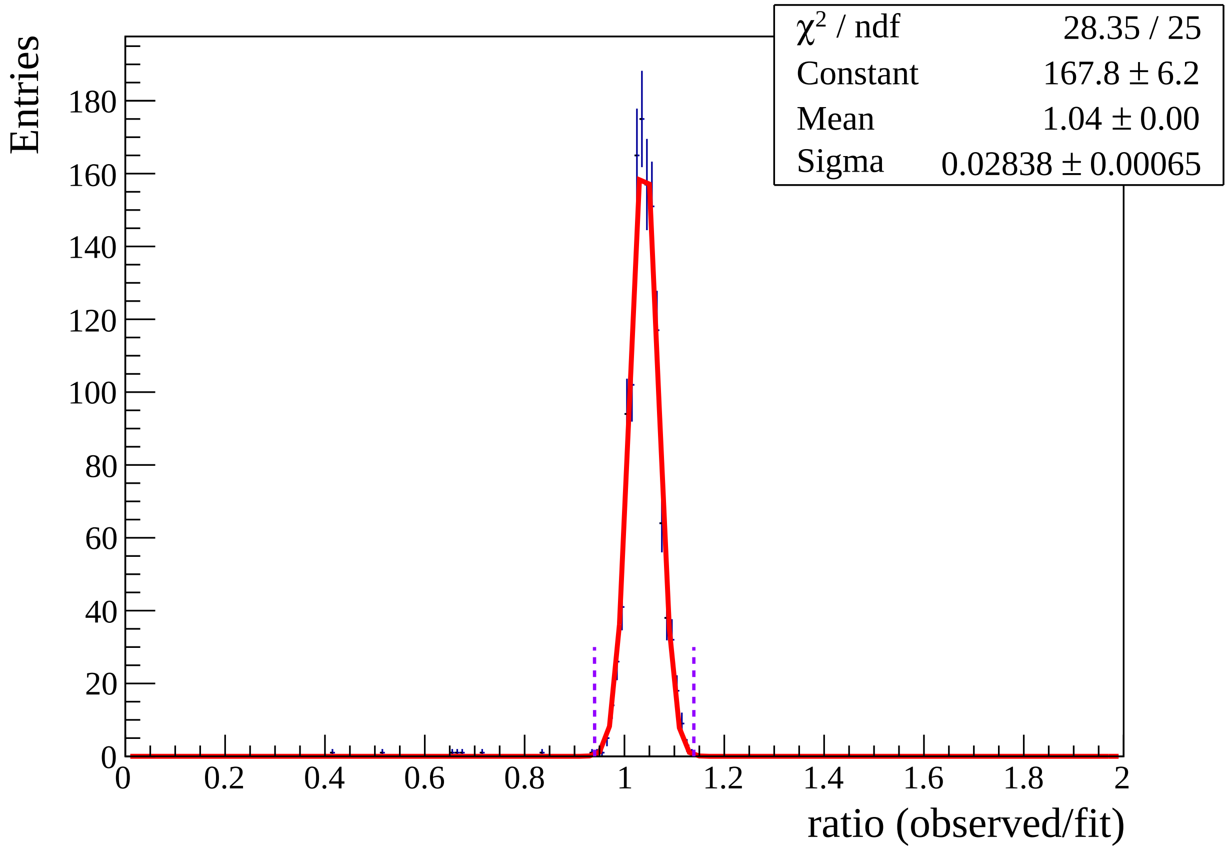

FIGURE 5.4: The distribution of ratio values of each calibration run in the DS6 dataset was calculated based on the observed and expected rate of 2615-keV events. The observed rate of each calibration run was calculated using Eq. 5.1. The expected rate of each run was calculated based on the fit parameters from Fig. 5.3. The two purple vertical lines are at 3.5 σ from the mean of the Gaussian peak.

5.3 Benchmarking Simulation

After the run selection based on 2615-keV γ-ray events, we studied the validation of simulation performed in MaGe. A good performance in estimating the detection efficiency of 2615-keV γ-ray events also implies its similar performance in estimating the detection efficiency of 6129-keV γ-ray analysis. In order to calibrate the detectors in M1 and M2 modules, two separate calibration source assemblies were manufactured. Each calibration source assembly contains a pair of ^{228}Th sources. We analyzed its performance in terms of activities of calibration source assemblies measured and expected over time using multiple years of data-taking.

The integrated activity of each calibration source assembly was reported as 10.36 ± 0.60 kBq with up to 3% deviation on homogeneity along the line on May 1, 2013 by the vendor. The activity of the source decays with a half-life of 1.912 years. Therefore, the expected activity of the source was calculated during each calibration based on Eq. 5.3. The corresponding uncertainty was calculated based on the propagation of initial uncertainty. However, 3% uncertainty was irrelevant because the rate from all active detectors combined was studied and hence not included in the uncertainty.

$$A_{expected} = A_0 e^{[-\lambda(t-t_0)]} \tag{5.3}$$

where,

$A_0 = (10.36 \pm 0.60)$ kBq

$\lambda =$ decay constant based on half-life of ^{228}Th which is 1.912 years

$t =$ timestamp of each calibration

$t_0 =$ initial timestamp of May 1, 2013

$A_{expected} =$ expected activity of source during calibration taken at timestamp t

The observed activity of the source in each calibration was calculated using an Eq. 5.4. The livetime and efficiency estimation have negligible uncertainty. Therefore the uncertainty in the observed activity is statistical only.

$$A_{observed} = \frac{R}{\epsilon \times b} \tag{5.4}$$

where,

$A_{observed} =$ observed activity of source

$R =$ rate of 2615 keV γ-ray events which is calculated based on number of counts and livetime of each calibration

$b =$ branching ratio of ^{212}Bi $\rightarrow$ ^{208}Tl decay, which is 35.9%

$\epsilon =$ efficiency of detecting 2615-keV γ-ray events in the Majorana Demonstrator.

The observed and predicted activity of each source assembly in each calibration were computed with corresponding uncertainties over multiple years of data-taking. The data analyzed here include calibration data sets from 2016-2019, which were also used in the analysis of the recent double-beta decay results [55]. Figure. 5.5 and Figure. 5.6 show a good agreement between expected activities

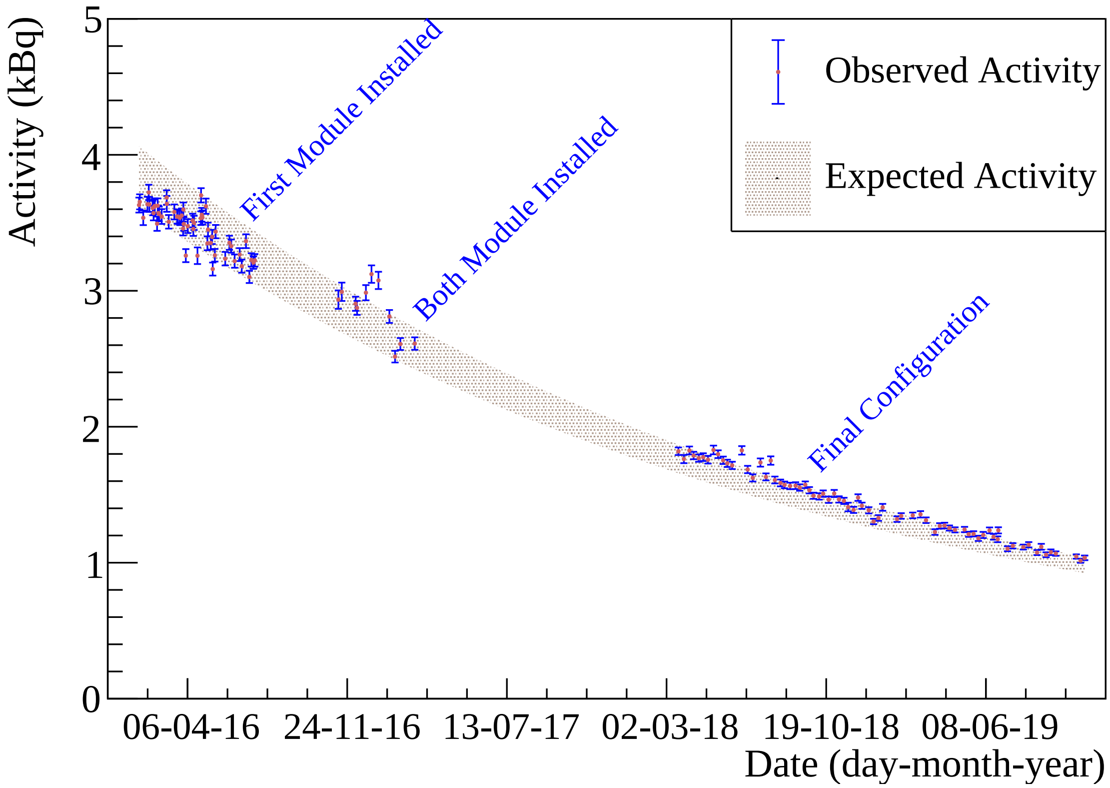

FIGURE 5.5: Observed and expected activities for the calibration source assembly A in the MAJORANA DEMONSTRATOR. This source was used to calibrate M1 detectors for a certain period before the second module was installed. After both modules were installed, it was used to calibrate M2 detectors. The data points indicate the observed activity of source A for each weekly calibration with associated statistical uncertainty. The band represents the expected activity, including the vendor-reported uncertainty. The gaps in the plot represent the periods during which data were not used for this analysis for the reasons mentioned in Section 5.2.

and observed activities of both sources assemblies. This implies a good accuracy for the simulations performed by MaGe and gives confidence that MaGe can make correct efficiency predictions for the analysis of the 6129 keV γ-rays.

The validation of simulation performed in MAGE was important not only for the analysis of 6129-keV γ-rays but also in the other MAJORANA DEMONSTRATOR analyses as well as in LEGEND experiment [52]. MAGE is primarily used for all simulations within MAJORANA DEMONSTRATOR experiment and in many simulations for the LEGEND experiment. We reported this quantitative validation study of the MAGE in the $^{13}C(\alpha, n)^{16}O$ analysis paper [133].

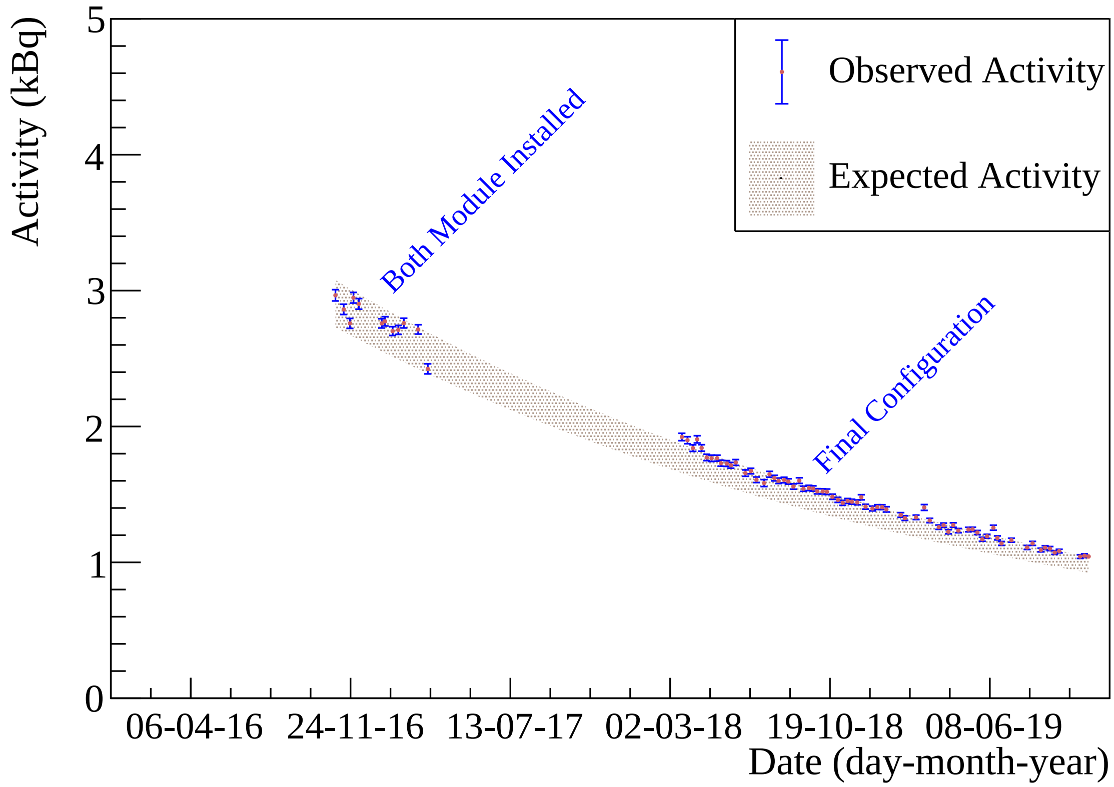

Figure 5.6: Observed and expected activities for the calibration source assembly B in the Majorana Demonstrator. This source was used to calibrate M1 detectors except for a period when source assembly B was used instead. The data points indicate the observed activity of source A for each weekly calibration with associated statistical uncertainty. The band represents the expected activity, including the vendor-reported uncertainty. The gaps in the plot represent the periods during which data were not used for this analysis for the reasons mentioned in Section 5.2.

5.4 Signature Search

The calibration runs that passed the run selection criteria mentioned in Section 5.2 which were also used in validating the simulation mentioned in Section 5.3 were used for the analysis of 6129 keV photons from the $^{13}C(\alpha, n)^{16}O$ reactions. The search of 6129 keV events in those calibration runs was performed using the sum energy of events from the low-gain channels saved as the $sumEL$ parameter in the Majorana Demonstrator data. The summed energy is obtained by summing all coincident energy depositions over all low-gain channels of active HPGe detectors within a 4 μs window. The $sumEL$ was used because of the high probability that several-MeV photons distribute their total energy in multiple detectors.

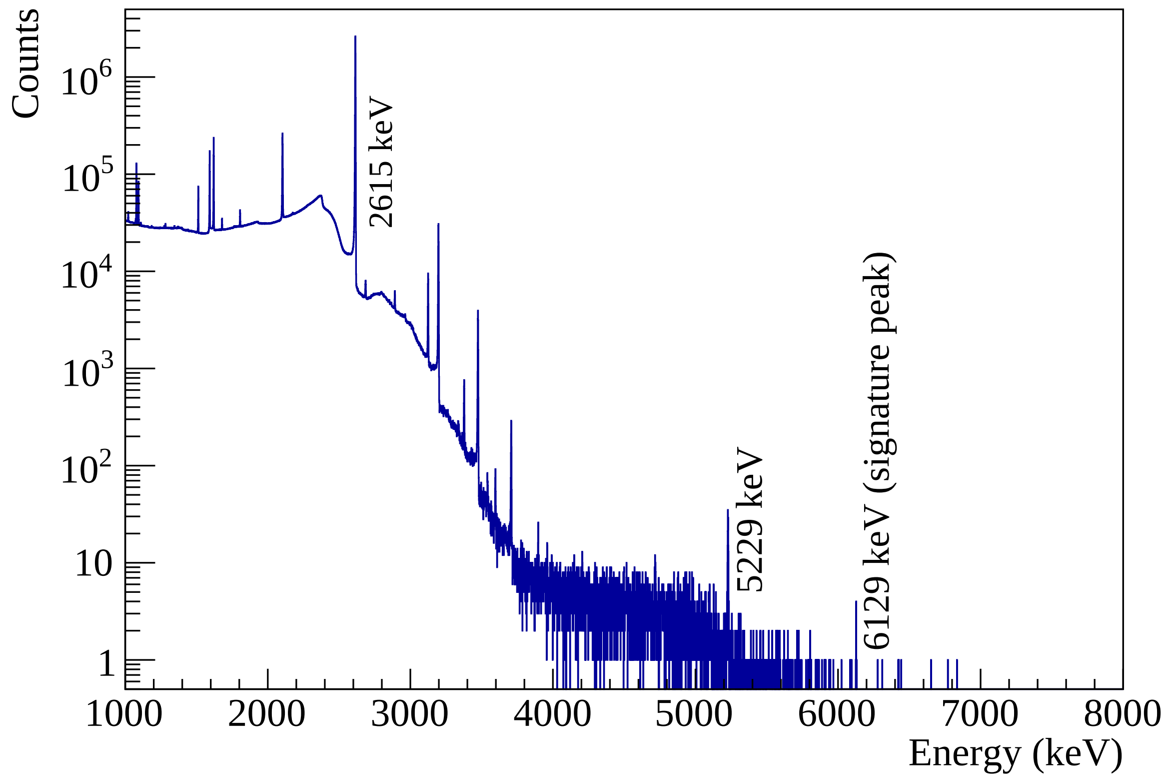

FIGURE 5.7: The sum energy spectrum from the low-gain channel using the calibration data selected for the analysis. It shows various γ-ray peaks, including 2615 keV and the signature peak of 6129 keV. The other peaks correspond to the peaks from the ^{228}Th decay chain, random coincidence events, and summing.

Fig. 5.7 shows the sum energy spectrum above 1 MeV in the calibration data that passed the basic data cleaning cuts mentioned in Section 5.2. The isomeric γ signature at 6129 keV following the $^{13}\mathrm{C}(\alpha, n)^{16}\mathrm{O}$ reactions is clearly seen in the spectrum, including several other peaks as expected. The other peaks are due to events from the ^{228}Th decay chain and their random coincidences and summing. For example, the most prominent peak at 2614.5 keV peak is from the β decay of ^{208}Tl, while the peak at 5229 keV is due to two 2614.5 keV events occurring within the coincidence window. Most of the events above 3 MeV are due to the coincidence of lower energy events.

The region of interest (ROI) for the 6129-keV peak search was defined based on the energy resolution at that energy region. The expected resolution (1σ) at 6.13 MeV is around 2 keV. Therefore, the ROI was defined as (6129 ± 10) keV, which covers about 5σ around each side of the peak. We found a total of 9 events in the ROI with all the data combined. Since the peak has low statistics, we performed a simple Gaussian fit with the Log-Likelihood method (option $'L'$) to the signal peak. We found the mean to be 6127±0.6 keV and the standard deviation to be 1.8±0.4 keV from the fitting shown in Fig. 5.8. Given the low statistics of 6129-keV events, the uncertainties in the fit are larger and less robust.

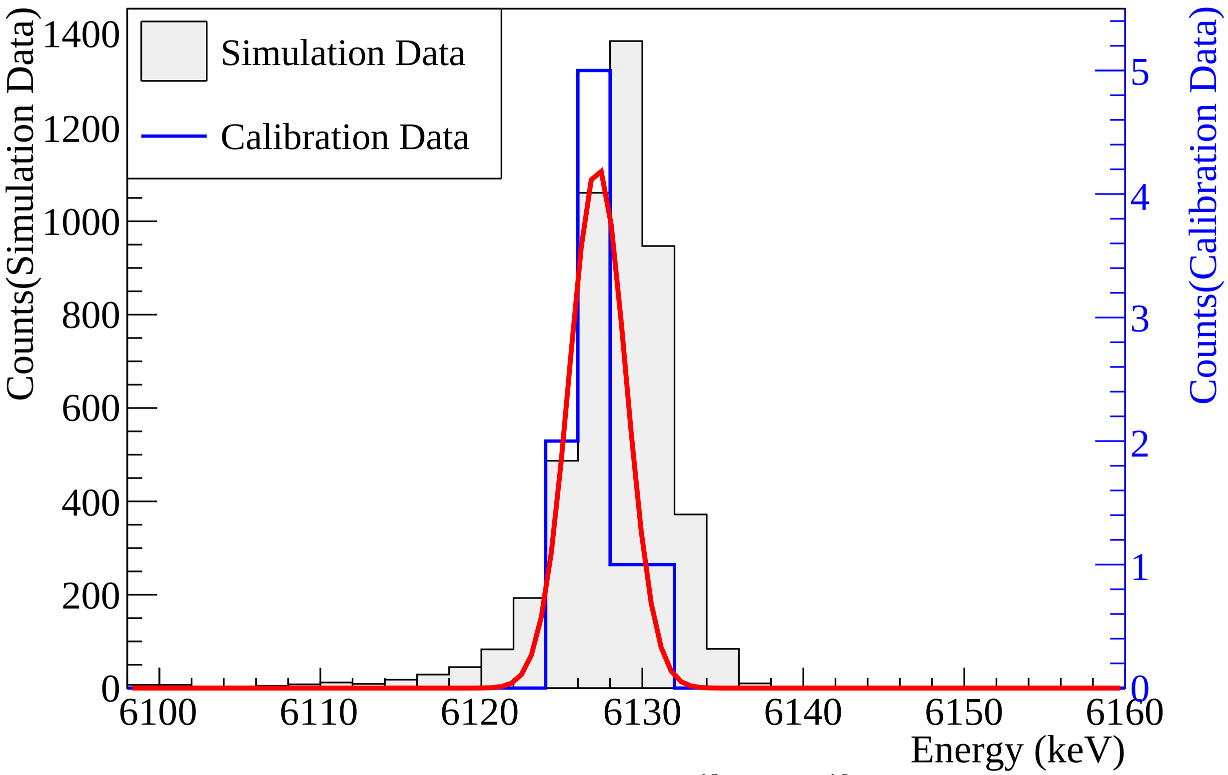

FIGURE 5.8: The 6129-keV signature peak from the $^{13}C(\alpha, n_2)^{16}O$ reactions in the MAJORANA DEMONSTRATOR calibration sources, shown in blue color and fitted with Gaussian in red. The gray-filled spectrum is the peak shape from the simulation of 1 million 6129-keV photons from the calibration tracks.

To cross-check the fit results of the signal peak in Fig. 5.8, we performed the fit to the much more substantial, higher energy peak at 5229 keV. Figure 5.9 is a simple Gaussian plus flat background fit performed to the 5229-keV peak. The mean was found to be 5228±0.2 keV with a standard deviation of 2.0±0.1 keV. These full energy peaks are seen at their expected locations and with their expected widths in the sum energy spectrum from the low-gain channels. In MAJORANA DEMONSTRATOR, we have a detailed study of energy linearity and systematic as mentioned in Chapter 3 and achieved an excellent performance. However, that study is limited to high-gain channels and up to 3 MeV for hit energy. Generally, the linearity in the low-gain channel is expected to be slightly worse than in high-gain. Also, the sum energy is expected to have slightly worsened energy resolution. However, the systematic study of these higher sum energy peaks from low-gain channels indicates the excellent energy performance extended to the energy range of multiple-MeV in the MAJORANA DEMONSTRATOR.

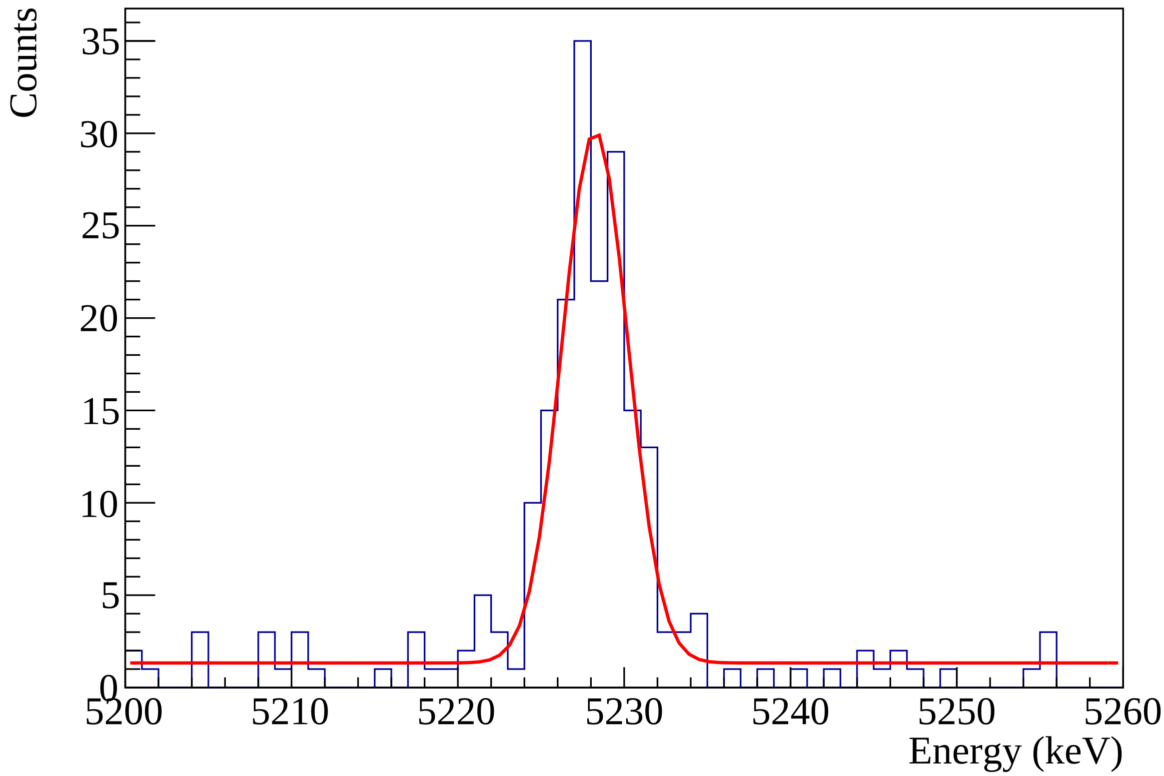

FIGURE 5.9: A Gaussian and a flat background fit performed to the 5229-keV peak from the double coincidence (2614.5 keV$\times$2) in the sum energy spectrum of the calibration data.

We found a clear signature peak with nine events, as shown in Fig. 5.8. Table 5.1 summarizes the detail information about those events. Figure 5.10 shows some sample waveforms of those events. All 11 waveforms, seven waveforms of multiplicity one events, and four waveforms of multiplicity two events were normal-looking as expected.

Table 5.1: 6129-keV signature events that lie within the ROI. A total of 9 events were found; among them, two are multiplicity two events, and the remaining are multiplicity one events.

Dataset	Detectors	Energy (keV)	mL	Energy split (keV)
DS2	C1P1D3	6127.1967	1	-
DS5ab	C1P2D3	6127.8565	1	-
DS6a	C1P3D3,C1P3D2	6125.1066	2	5647.8644,477.24223
DS6b	C2P3D1	6127.8895	1	-
	C1P3D3	6127.1245	1	-
	C1P2D2	6130.8384	1	-
	C2P4D2	6129.5045	1	-
DS6c	C1P2D2, C1P3D3	6124.3313	2	5878.2240,246.10730
	C2P2D1	6126.5728	1	-

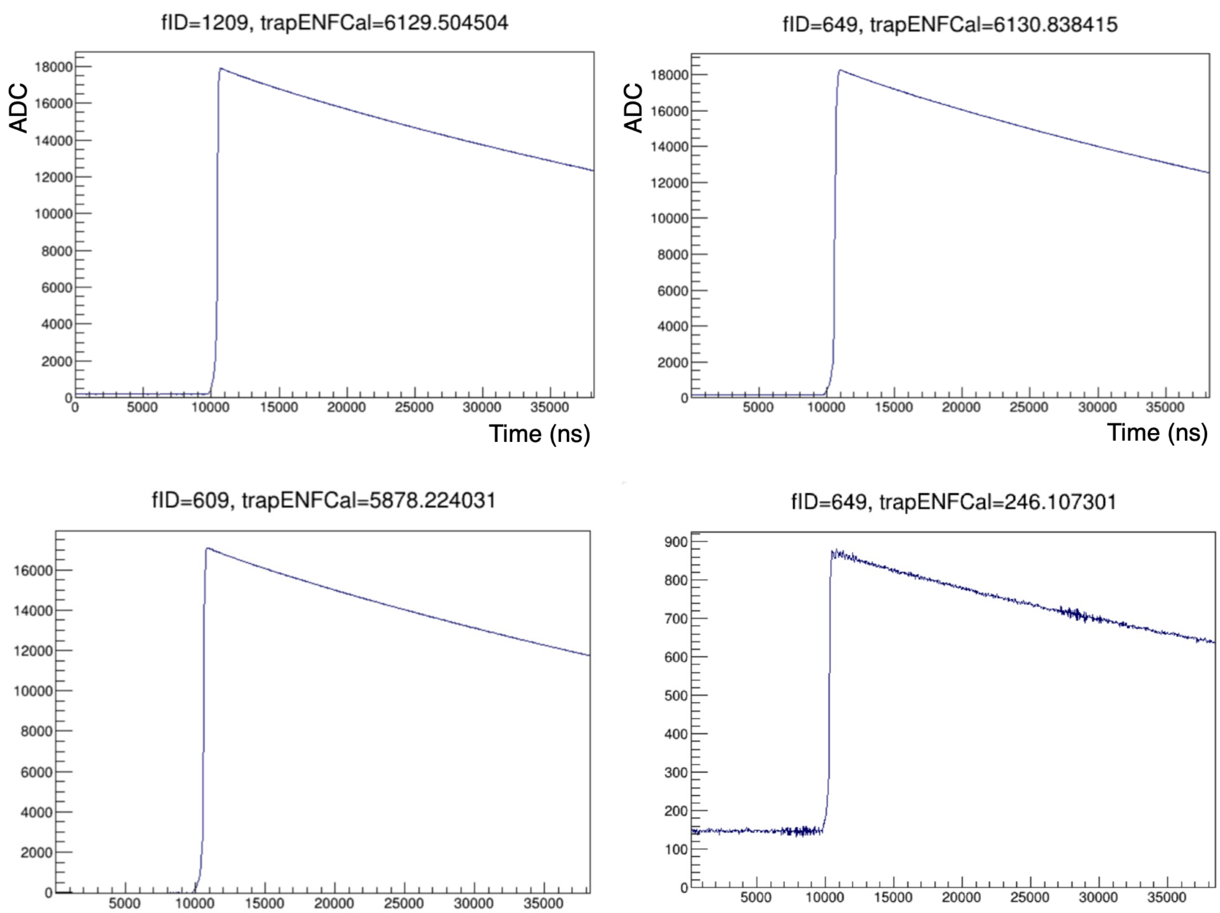

FIGURE 5.10: (Top): Waveforms with a multiplicity of one (mL = 1) event. FID is the channel ID of the detector, and trapENFCal is the hit energy of the event. (Bottom) Waveforms of an event with a multiplicity of two (mL = 2) events. This event has sum energy of 6124.3313 keV that is distributed in two detectors.

5.5 Background Estimation in ROI

The signature peak at 6129 keV stands out clearly, as seen in Fig. 5.8, so all the 9 events in the peak are considered to be true signal events. Also, there are no background events at least 20 keV on both sides of the peak outside the ROI, *i.e.* 6099 keV to 6119 keV and 6139 keV to 6159 keV. The potential background in that 40-keV region at the 1σ level could be at most 1.29 counts based on the Feldman-Cousins statistics [134]. This translates to an upper background limit in the 20-keV ROI as 0.64 counts. However, to better estimate the potential background contribution to the ROI, we considered a much wider energy region, *i.e.* from 6 MeV to 6.5 MeV excluding the 20-keV ROI. In this 480-keV region, we found 8 events as seen in Fig. 5.11, based on which 0.33 counts of background is estimated in the ROI. In the smaller sidebands, this projects to 0.67 counts of background estimation. This is statistically consistent with observing no events, which would happen with 50% probability. In summary, the observed number of events in the ROI is 9, whereas the predicted background contribution to the expected number of events is 0.33 counts. The difference between 0.64 and 0.33 counts, *i.e.* 0.31 counts is considered as systematic uncertainty due to background contribution in the ROI.

5.6 Prediction of 6129 keV Event Rate

The number of 6129 keV photons predicted in the calibration data of each dataset is estimated based on the yield, detection efficiency, activity of the calibration source, and exposure time of the calibration data. The predicted number of events in each weekly calibration is calculated using Eq. 5.5 and summed over all weekly calibrations in the dataset.

$$N = Y \times \sum_i A_i \times \epsilon_i \times T_i \tag{5.5}$$

where,

N = Number of 6129 keV events predicted in each dataset

Y = Yield of 6129 keV photons from the calibration source, which is estimated as number per ^{228}Th decay

A_i = Activity of source during each weekly calibration

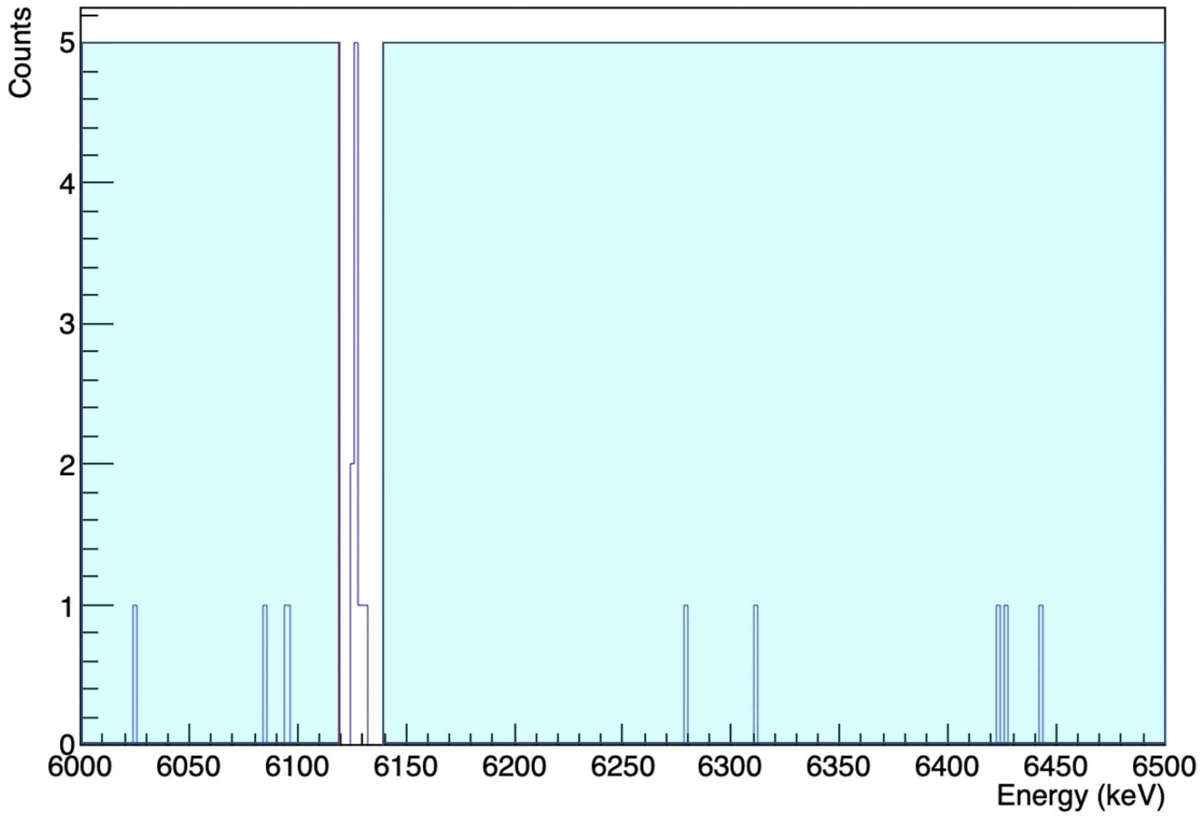

FIGURE 5.11: Events in the shaded region shown in cyan color were used for the background estimation in the ROI. There are 8 events in the 480-keV region which are mostly higher multiplicity events.

ϵ_i = Efficiency of detecting 6129 keV photons in each weekly calibration

T_i = Livetime of each weekly calibration

The source activity reduces exponentially as ^{228}Th decays away. Therefore, the expected activity of the source during each weekly calibration is used. The activity and livetime values used in the calculation are described in Sec. 5.3. The estimation of other quantities in Eq. 5.5 and total systematic uncertainty in the estimation are described in the following subsections.

5.6.1 *Estimation of 6129 keV photon Yield from NeuCBOT*

The yield of 6129 keV photons from the ^{13}C$(\alpha, n)^{16}$O reaction in the calibration source is estimated with NeuCBOT software. In NeuCBOT, the precompiled database for all naturally occurring isotopes ranging from 0 to 10 MeV α-particles generated by TALYS-1.95 are available. Those database values for all the isotopes present in the calibration source were downloaded. Then the software is modified such that the partial cross-section of the second excited state ($J^{\pi} = 3^{-}$) of ^{16}O in the ^{13}C$(\alpha, n)^{16}$O is used, which produces 6129 keV photons. Figure 4.4 of Chapter 4 shows this cross-section, including other partial and total cross-sections. The vendor had provided the epoxy resin and hardener materials used in manufacturing the calibration source in the private communication. The exact mixing ratio was kept secret, but both are carbon-rich materials, and the yield does not change much between them. Therefore, we used the average yield of 6129 keV photons from the calibration source using NeuCBOT, which is estimated to be 2.98×10^{-7} γ/decay with 4% uncertainty due to the mixing ratio. The unit of per decay refers to the top of the decay chain, which is ^{228}Th in this case for the Majorana Demonstrator calibration source. In addition, there is 5% of systematic uncertainty in the yield due to uncertainties in the SRIM reported in Ref. [135].

5.6.2 Detection Efficiency

The efficiency of detecting full energy events of 6129 keV γ-rays is estimated based on simulation performed in MaGe. Figure 5.12 is the sum energy spectrum from the simulation of such photons in the M1 calibration track. As discussed in Subsection 5.2.1, efficiency is estimated for each calibration to include only active good detector's response in the simulation. The efficiency in each calibration is done based on the sideband subtraction method. The signal region is defined as (6129±10) keV and two sidebands of width 10 keV in each side of ROI, *i.e.* 6099 keV to 6109 keV and 6049 keV to 6059 keV regions. Figure 5.13 shows the efficiency of detecting full energy 6129 keV events in each calibration. The average efficiency is higher in module 1 calibration data-taking due to more active detectors in the M1 module.

The systematic uncertainty in the simulation is estimated based on the observed activity of the calibration source. The observed activity in each calibration using 2615-keV hit energy events is described in Sec. 5.3. We repeated the same procedure to calculate based on the rate of 2615-keV sum energy events. We used DS6b calibration data to calculate the observed activities based on the 2615 keV sum energy events. The difference between the two approaches is calculated for each calibration. The percentage difference is then evaluated based on the expected activity during that calibration. Figure 5.14 shows such distribution with a simple Gaussian fit. The mean difference is 11.9% and we treated it as a systematic uncertainty in simulation.

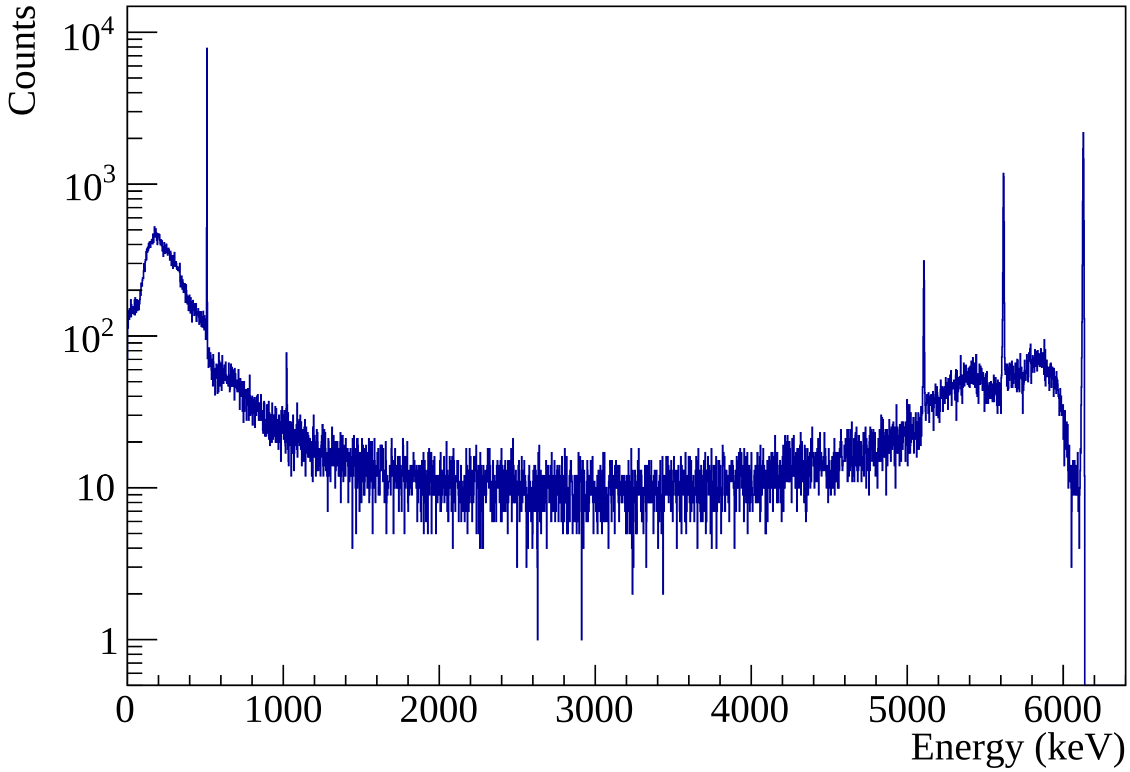

FIGURE 5.12: Sum energy spectrum from the simulation of 1 million 6129 keV γ-rays populated isotropically in the calibration track of the M1 module. The spectrum shows the 6129-keV peak and some other peaks as expected. The single and double escape peaks at 5618 keV and 5107 keV, respectively, are due to 6129-keV events. The 1022-keV peak is due to the double coincidence of two 511-keV events.

5.6.3 Systematic Uncertainty

The total systematic uncertainty in estimating the expected number of 6129 keV events is calculated based on uncertainties in various quantities in Eq. 5.5. Table 5.2 summarizes the individual and total uncertainties in the estimation. The systematic uncertainty in background contribution is 8.3% which is based on 0.31 counts expected in the ROI described in Sec. 5.5 and total expected 6129 keV events. The total uncertainty is calculated by adding individual uncertainties in quadrature.

5.7 Comparisons between Measurements and Predictions

The expected and observed number of 6129 keV events in each data set and in a combined dataset are shown in Fig. 5.15. The observed number of events tends to be higher than expected; however,

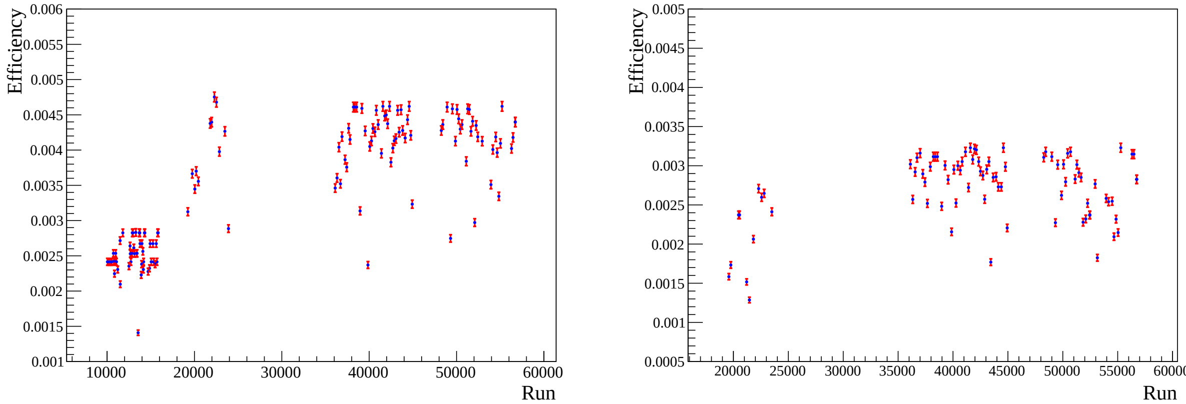

FIGURE 5.13: Left): Efficiency of detecting full energy events of 6129 keV γ-rays when the source is deployed in calibration track of M1 module. Each data points represent the efficiency of that weekly calibration with a statistical uncertainty in simulation. The run number in the X-axis corresponds to the first run of each weekly calibration. (Right): The similar plot when the source is deployed in the calibration track of the M2 module.

Table 5.2: Uncertainties for the expected number of counts. The total systematic uncertainty is the sum of individual systematic contributions in quadrature.

γ yield value due to uncertainties in the SRIM reported in [135]	5.0%
Chemical composition in epoxy	4.0%
Activity of the source as reported by Eckert & Ziegler	5.8%
Systematic uncertainty in simulation	11.9%
Statistical uncertainty in simulation	1-2 % (neglected)
Systematic uncertainty in background contribution	8.3%
Total systematic uncertainty	16.9%

statistical uncertainty is large, and they are consistent within the 90% confidence level interval of Poisson's signal mean. This agreement suggests that TALYS-generated cross-sections combined with the SRIM database can reasonably estimate (α, n) reactions rate. Since the precise cross-section measurement relevant for the entire range of α-particle from the ^{228} decay is sparse, one can use a statistical modeling approach such as TALYS. The overall consistency supports the approach of predicting radiogenic neutron yield in low-background experiments using TALYS-based NeuCBOT.

5.8 Summary

The work presented in this chapter demonstrates the technical achievements of the MAJORANA DEMONSTRATOR in terms of energy performance and robust as-built simulations. A direct comparison between expected and observed activities of calibration source assemblies over multiple years

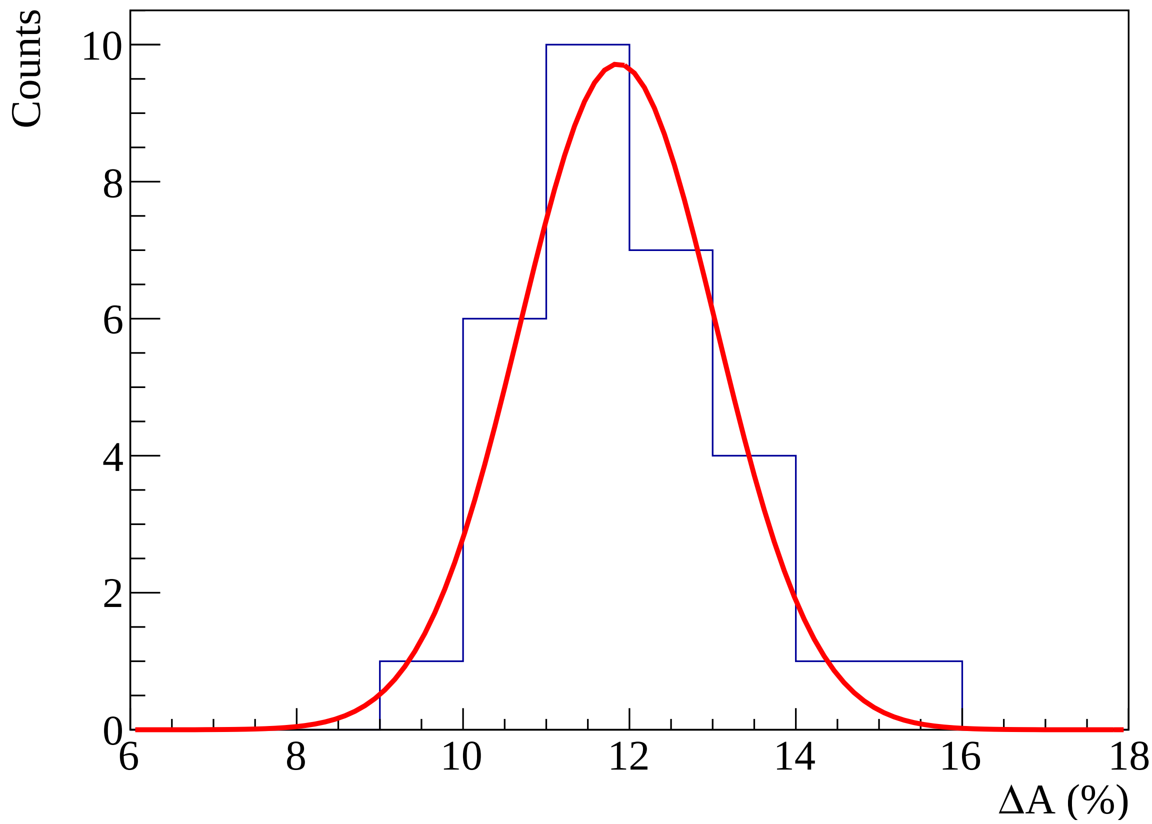

FIGURE 5.14: The distribution of the difference in activities of the calibration source observed based on the rate of 2614 keV hit energy events and sum energy events in DS6b dataset. The mean and standard deviation were found to be 11.9 ± 0.2 and 1.9 ± 0.2, respectively.

Table 5.3: Expected and observed counts of 6129-keV photons in each dataset. Expected counts are estimated based on Eq. 5.5, and the corresponding uncertainties are the 16.9% of total systematic uncertainty reported in Table 5.2. The range of signal mean is the 90% C.L. interval of Poisson signal mean based on observed signal counts in each data from the Feldman-Cousins statistics [134].

Data Set	Integrated Exposure Time (hour)	Expected Counts	Observed Counts	90% C.L. Interval of Signal Mean given Observation
DS1	40.2	0.42 ± 0.07	0	[0.00, 2.44]
DS2	13.4	0.13 ± 0.02	1	[0.11, 4.36]
DS5	41.8	0.41 ± 0.07	1	[0.11, 4.36]
DS6a	43.9	0.32 ± 0.05	1	[0.11, 4.36]
DS6b	178.3	1.19 ± 0.20	4	[1.47, 8.60]
DS6c	245.0	1.27 ± 0.21	2	[0.53, 5.91]
Total	562.6	3.74 ± 0.63	9	[4.36, 15.30]

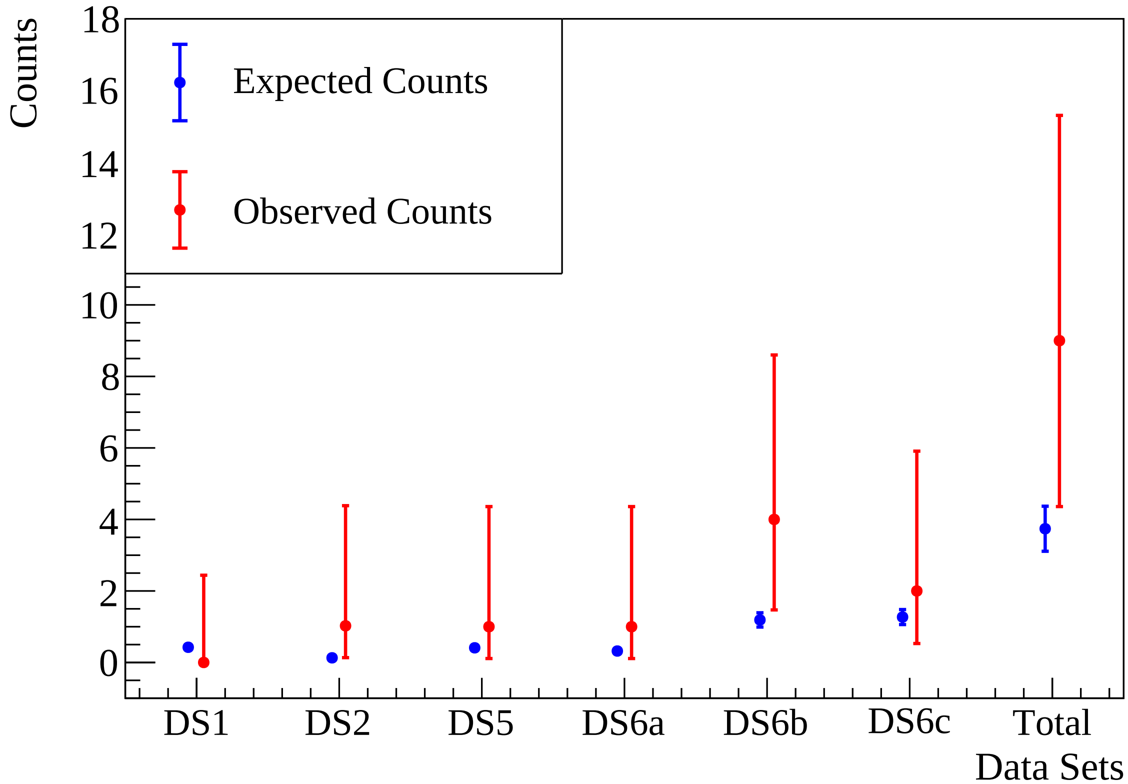

FIGURE 5.15: Observed and expected number of 6129-keV photons with corresponding uncertainties in each data set and the combined data set. The corresponding uncertainties are from Table. 5.3.

of data-taking is performed. A good agreement between measurements and observations adds credibility in simulations performed using MaGe for the Majorana Demonstrator. In addition, a systematic study of higher energy photons beyond 3 MeV suggests that the Majorana Demonstrator has excellent energy performance in wide energy regions. Thanks to excellent energy performance, 6129 keV isomeric photons from the $^{13}C(\alpha, n)^{16}O$ reaction are clearly observed in the calibration data. Combining with MaGe simulations, a direct comparison of observed 6129 keV photon rate with prediction based on TALYS-based NeuCBOT is performed. At 90% C.L., the measurement is consistent with predictions, albeit with large statistical uncertainty. This result suggests that TALYS-based NeuCBOT can reasonably estimate (α, n) reaction rate. The combination of Geant4 simulations and TALYS-based NeuCBOT can be used to estimate the radiogenic neutron background contribution to the experiment. The background contribution of such neutrons produced from the calibration source during calibration data-taking is estimated. The background level at the Majorana Demonstrator turned out to be not a concern. However, future experiments with a stringent background goal, for example, LEGEND, would require understanding and estimating such neutron contributions with reasonable detail and precision. The combination of NeuCBOT software and MaGe are also used to estimate (α,n)-neutrons induced background for LEGEND [52].

6

Pulse Shape Based Analysis using Interpretable Machine Learning Model

6.1 Introduction

The development of analysis techniques to reject various possible backgrounds plays an important role in rare-event searches. In addition to the traditional techniques, machine learning-based approach have been used widely to identify and reject various background in neutrinoless double-beta decay experiments [136–138].

In Majorana Demonstrator, PPC detector geometry allows powerful PSA techniques. One such analysis technique developed in the Majorana Demonstrator is called AvsE, as described in Chapter 2. The AvsE is used to remove multi-site events in the detector, which are backgrounds for $0\nu\beta\beta$ searches, and it suppresses the background level at ROI by a factor of three. The rising edge of single-site and multi-site waveforms have different features, as shown in Fig. 2.5. Therefore, we used machine learning approach to identify between them. An interpretable Recurrent Neural Network (RNN) model has been developed that has the potential to outperform the traditional AvsE approach to reject multi-site events. This chapter describes the RNN model, its performance, a comparison with the AvsE approach, and its potential impact on the next-generation experiment like LEGEND.

6.2 Recurrent Neural Network

A recurrent Neural Network (RNN) is a canonical model for natural language processing and time-series data. The waveforms of each event recorded in MAJORANA DEMONSTRATOR are the time series data. In the recurrent unit of RNN, each waveform sample, $\vec{X}_t$, at time sample, t in the time series, $[t, \vec{X}_t]$ is fed sequentially. The recurrent unit contains a hidden state, $\vec{h}_i$, which stores information from previous hidden states during training. The recurrent unit has two kernels one is w_{input} for current input $\vec{x}_t$ and other, w_{hidden}, for the previous hidden state, $\vec{h}_{t-1}$. As the recurrent unit moves each step forward in the time sample, the kernel is updated based on Eq. 6.1 where $\vec{h}_{t-1}$ and $\vec{x}_t$ are analyzed together. This iteration goes until the last time sample data in the waveform and gives the last hidden state output $\vec{h}_n$ with a waveform divided into n number of samples as an output of the network. Figure 6.1 is a typical waveform with a schematic of traditional recurrent unit. The recurrent unit is adapted from Colah's lab [1].

$$\begin{aligned} \vec{h}'_t &= w_{input}\vec{x}_t + w_{hidden}\vec{h}_{t-1} + bias \\ \vec{h}_t &= tanh(\vec{h}'_t) \end{aligned} \tag{6.1}$$

The traditional RNN handles the order information of the data well, but there might be long-range information loss. The rising edge of the waveform is the one that carries information whether the given waveform is due to single-site interaction or multi-site interaction. This information can be lost until the recurrent unit moves to the final waveform sample. To account for this issue, a special RNN called Long Short Term Memory (LSTM) [139] can be used. The core idea behind LSTM is that it contains cell states and hidden states. The cell state is responsible for keeping long-term memory, and the hidden state is responsible for short-term memory. The gate operation in LSTM controls the information flow between short-term and long-term memories. Figure 6.2 on left shows a schematic of gate operation in LSTM. The schematic diagram is adapted from [2]. The three basic gate operations in LSTM are briefly described below.

- Forget gate: Current input and previous hidden state are analyzed together and fed into the

[1] http://colah.github.io/posts/2015-08-Understanding-LSTMs/

[2] http://dprogrammer.org/rnn-lstm-gru

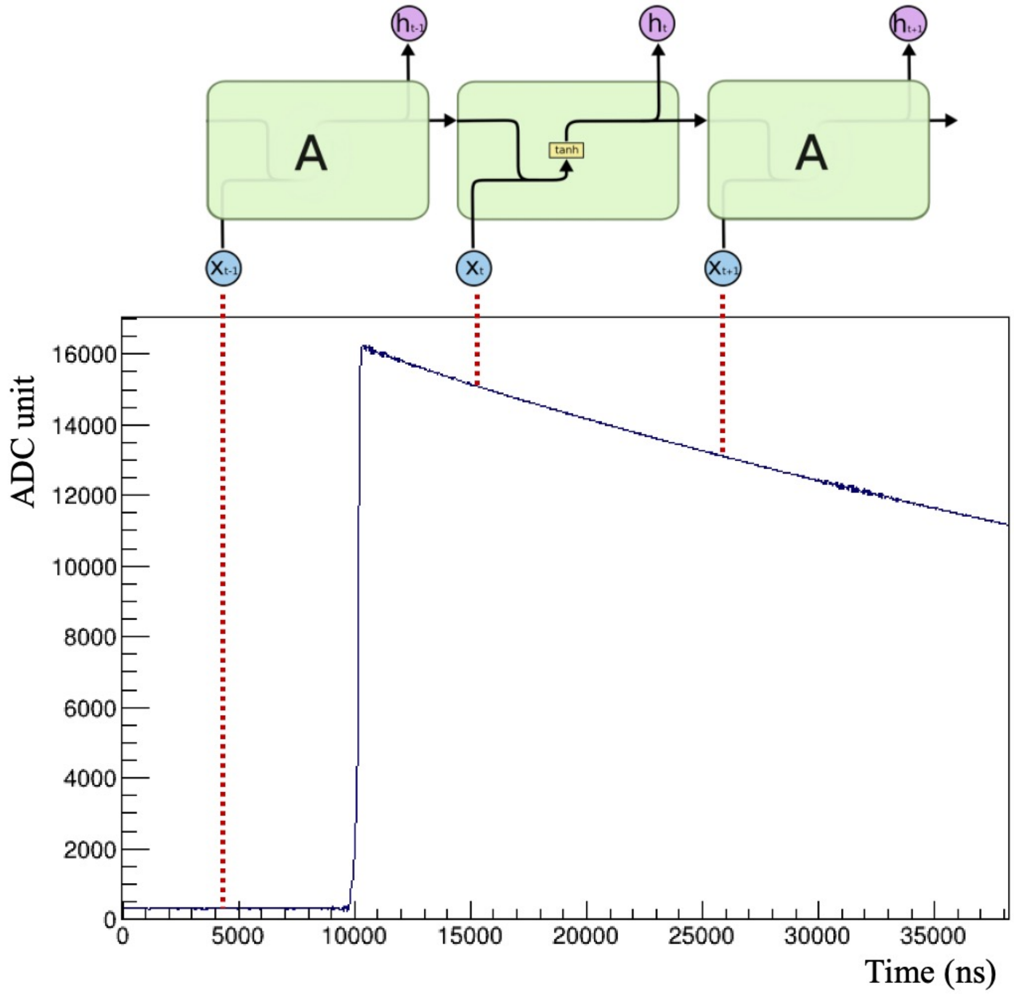

FIGURE 6.1: A typical waveform with a recurrent units of RNN where X_t is ADC sample in waveform at time sample t. Adapted from Colah's lab `http://colah.github.io/posts/2015-08-Understanding-LSTMs/`

Sigmoid function. The output, f_t, is used to define how much information has to be preserved or erased for the cell state.

- Input gate: In this gate, the input of the information that has to be added to the cell state occurs. The amplitude of the information is calculated based on the Sigmoid output of hidden state input, i_t, and hyperbolic tangent output of cell input, $\tilde{C}_t$. This information remains constant until the recurrent unit moves to the next time sample data.

- Output gate: The output gate structure is similar to the input gate, but the output is calculated based on the cell state. The output is calculated based on Sigmoid output, O_t, and hyperbolic tangent of cell state C_t.

We built a neural network model based on Gated Recurrent Unit (GRU) [140] which was introduced to solve the vanishing gradient problem in RNN. This GRU is the modified version of LSTM, where it combines long and short-term memories into a hidden state. It has two gates; reset gate and update gates, as shown in Fig. 6.2. It has two gates, unlike in the LSTM, and they are briefly described below.

- Reset gate: The gate, r_t, is responsible for deciding how much previous information is essential to neglect.
- Update gate: The update gate, z_t is used to calculate the amplitude of the previous information that needs to be passed along the next state.

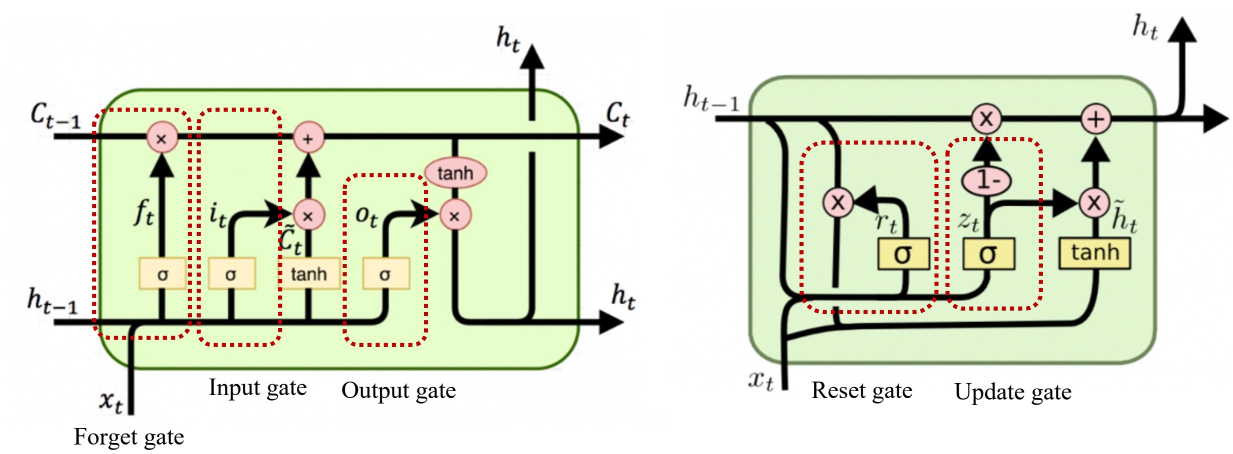

FIGURE 6.2: A schematic of gate operation of LSTM network on left and GRU on right. These schematic diagram are adapted from `http://dprogrammer.org/rnn-lstm-gru`.

Attention Mechanism

The LSTM or GRU networks preserve long-range correlation in which the final hidden state output, h_n, contains information of all previous steps. However, the h_n often loses focus to the most critical part of the time samples due to information overload. The information on whether the given waveform corresponds to single-site or multi-site interaction lies in the rising part of the waveform, while the baseline and falling edge do not have that information. Therefore, not all hidden state outputs of the network are equally important. The hidden state output of the time sample in which the rising edge lies is the most important, while others are less important. In order to utilize all the hidden state outputs individually, we applied the attention mechanism [141] that allows the network to put more attention to the most important time samples. The three sequential steps in the attention mechanism are briefly described below.

- Similarity scores: It is a scalar quantity, s_i, calculated between each hidden states, h_i, with final hidden state h_n. This represents how well the h_n is aligned with each h_i. There are various ways to calculate the similarity matrix depending on the types of attention. Equation 6.2 is weight kernel concatenation where w is a kernel tensor whose value is updated during the network training.

$$s_i(h_i, h_n) = h_i^T w h_n \tag{6.2}$$

- Weights: These are the attention scores for each time sample computed by applying Softmax operation to the previously calculated similarity scores.

$$\vec{a} = Softmax([s_0, s_1, ..., s_{n-1}, s_n]) \tag{6.3}$$

- Context vector: It is a weighted sum of the weights and intermediate hidden states.

$$C = \sum_i^n a_i h_i \tag{6.4}$$

The context vector and final hidden state output are concatenated into a single attention vector and fed into the Fully Connected Neural (FCN) network, which has one neuron in the output layer.

6.3 Data Selection

We used ^{228}Th calibration data from the DS8 dataset for training and testing the network. This dataset has 21 PPC detectors and 4 Inverted Coaxial Point Contact (ICPC) detectors. The DS8 calibration skim data with GAT revision tag `GAT-v02-11-2-g6b785f1` was used. The network training requires both classes of data; background and signal. The double escape peak (DEP)

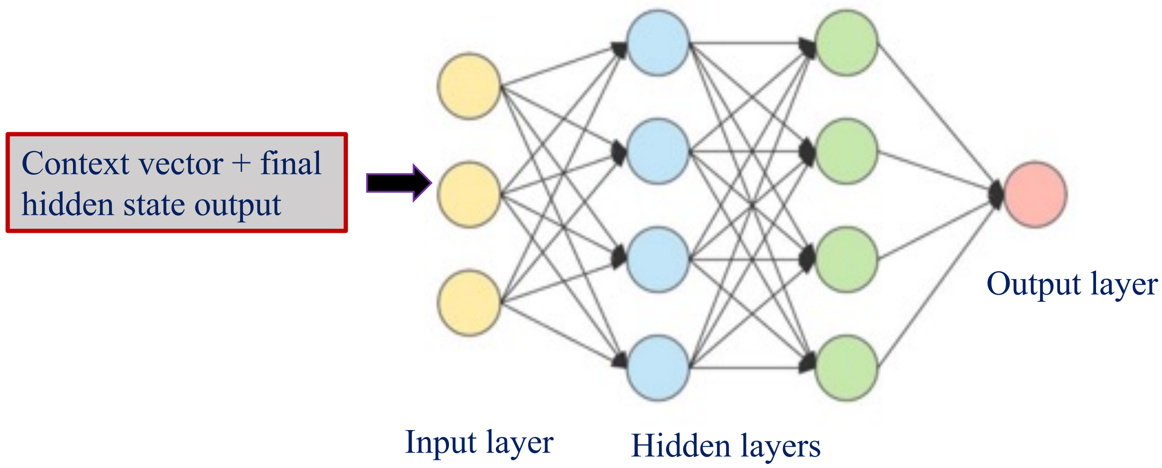

FIGURE 6.3: A schematic for a fully connected neural network. The context vector and final hidden state output are concatenated and fed into the input layer of FCN.

and single escape peak (SEP) events of 2614-keV peak from ^{208}Tl are inherently single-site and multi-site interactions. The DEP and SEP events are proxies to the signal and background for the $0\nu\beta\beta$ search. Therefore, we selected waveforms from the DEP and SEP energy regions based on the energy cut. The energy window for DEP and SEP events were selected as (1592.5 ± 1.5) keV and SEP as (2103.5 ± 1.5) keV, respectively. The data following standard data cleaning cuts were applied for the data selection.

```
Final_Energy > a && Final_Energy < b && channel == c && isGood == 1
&& isLNFill1 == 0 && isLNFill2 == 0 && wfDCBits == 0 && mH == 1
```

where,

`a`, `b` are lower and upper bound of energy window

`c` is the high-gain channel of the detector The waveform and corresponding parameters as $avse\_corr$, detector id, and t_0 were extracted from each high-gain channel of PPC detectors. Since ICPCs use ORNL analysis, we extracted $ORNL\_AoverE$ parameters for them. We saved each detector's SEP and DEP data in two separate pickle data files. The $avse\_corr$ and $ORNL\_AoverE$ were used to compare the network's performance with the traditional approach of AvsE for PPCs and ICPCs, respectively.

6.4 Simultaneous Training of Network

The network was trained by using all of the detector's training data simultaneously. Unlike in the traditional AvsE approach, simultaneous network training avoids detector by detector parameter tuning. This is especially important for next-generation experiments with a large number of detectors, such as LEGEND. This approach requires a single well-trained network that can be used to test detector-by-detector performance in rejecting the background events. To get a single trained model, we applied a one-hot encoding to the detector id. Each detector can be represented by a vector, and testing of the network can be done on the detector using a trained network. Since there are 25 enriched detectors, each one-hot encoded vector of a detector has 25 elements.

The baseline and falling edge of the waveform are not crucial in classifying signal-like and background-like events. Therefore, we chopped off the first few sample data from the baseline and the last few sample data from the falling edge of the waveform. It was done by selecting the data from the 100-time sample prior to t_0 until the 200-time sample after t_0. Then the waveforms were normalized so that their heights were equal irrespective of their corresponding energies. Next, the normalized waveforms were labeled; label 1 for DEP waveforms and 0 for SEP waveforms. Figure. 6.4 shows the labeled waveforms in charge and current domain.

The network was built in a Pytorch [142] framework which uses a torch library. Waveforms, labels, and corresponding one-hot encoded vectors were fed to the network for each batch sample. The prediction is computed based on the loss function used in each forward pass. We used `BCEWithLogitsLoss` as a loss function in which the Sigmoid function and Binary Cross-Entropy Loss (BCELoss) are combined into one class. In the backward pass, the gradient is calculated, and the weights and bias are optimized to minimize the loss using `Adam` optimizer. The following is the list of hyperparameters used to optimize the result.

- Number of hidden layers: 3

  There is no analytical rule for choosing the correct number of hidden layers in the network. However, having too many or too few hidden layers compared to a sufficient number of layers may cause overfitting and underfitting, respectively. It has been reported that a good accuracy with the lowest time complexity can be achieved with three or fewer hidden layers in

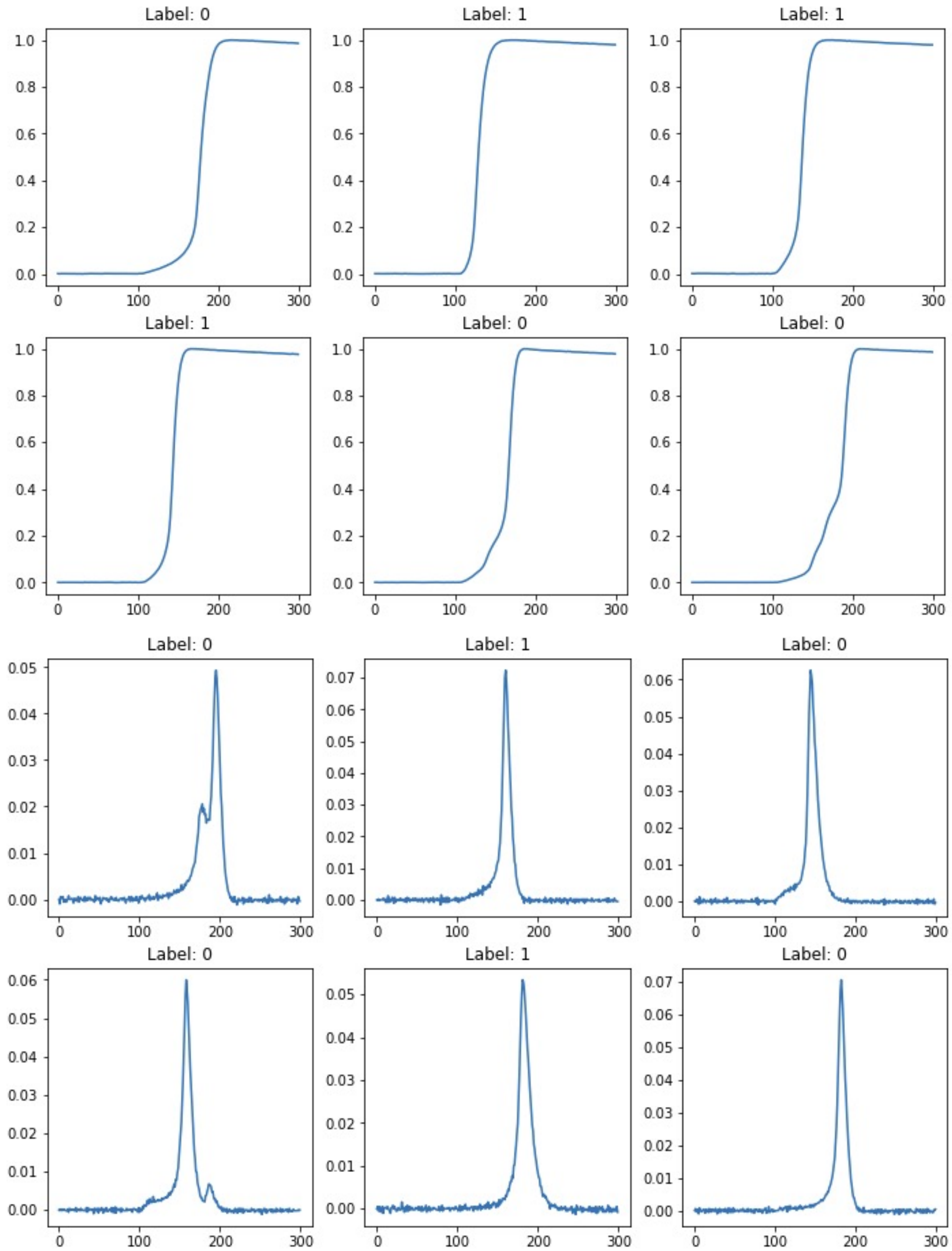

FIGURE 6.4: (Top two rows): Normalized labeled waveforms in the charge domain. (Bottom two rows): The labeled waveforms in the current domain were obtained by differentiating the charge domain waveform. The waveform in charge and current domains correspond to different data samples.

backpropagation neural network architecture [143]. Furthermore, we found that with three hidden layers, network performance was satisfactory with less training time.

- Number of neurons: [512,256,128,64,1]

  The network was built for binary classification to identify whether the given waveform is single-like or background-like. Therefore, the output layer was adjusted to contain one neuron. The number of neurons in the input and hidden layers, on the other hand, can be adjusted through trial and error. We used 512 neurons in the input layer and half of the neurons in each following hidden layer.

- Activation function: LeakyReLU

  A non-linear activation function, Leaky ReLu, is used in each hidden layer to avoid gradient vanishing problems which is possible in the ReLU activation function.

- Dropout: 0.2

  The dropout layers were added to avoid the possibility of overfitting in the training data by randomly dropping neurons at a rate of 20%.

- Batch size: 32

  We used the batch size of 32 based on the training data size and time taken for each training iteration.

- Number of epochs: 100

  The optimal number of epochs was chosen to be 100 based on the performance of the network during training.

- Learning rate: 0.01

  Setting a reasonable learning rate aids in the efficient convergence of loss minimization. Training would be faster with a higher learning rate, but the model might not converge to the minimum loss. On the other hand, the model would converge with a lower learning rate, but training would be very slow. We found the optimal learning rate of 0.01, at which the model was efficiently trained.

The network was trained by using waveforms in both charge and current domain. We examined the performance with two trained networks, one with a charge domain and the other with a current domain.

6.5 Network Performance

The network was trained using waveforms in both the charge and current domain. Then, the two trained networks were used to evaluate the corresponding performance of identifying signal-like and background-like events on each detector using their testing dataset. Subsection 6.5.1 describes the output distribution of the network for SEP and DEP events. Subsection 6.5.2 shows the confusion matrix plots. Subsection 6.5.3 describes the quantitative performance and comparison with the traditional approach of AvsE.

6.5.1 Network Output

The output layer of the network gives some score for each waveform based on the final hidden state output, weight vector of the output layer, and bias of the output layer. The optimum parameters that give the minimum loss during the training are saved in the trained networks. We used two trained networks to get the distribution of network output on testing data in each detector. Figure 6.5 and Fig. 6.6 shows the distribution of network output for DEP and SEP events in a PPC and ICPC detectors respectively. We observed a clear separation of the distribution between SEP and DEP events in the charge and current domains. Furthermore, the distributions were similar between PPC and ICPC detectors, as expected.

6.5.2 Confusion Matrix

The network was used for the binary classification with two classes to classify, a signal and a background class. In order to better visualize the performance of the network in identifying signal and background events, confusion matrices were plotted. Each entry in a confusion matrix represents classification based on the traditional approach, and the prediction by the network. Figure 6.7 and Fig. 6.8 are the confusion plots for a PPC detector P42575B and an ICPC detector P43387A respectively. The AvsE approach uses different parameters and cut thresholds for PPC and ICPC detectors. It uses `avse_corr`, represented by AvsE corrected for PPC detectors and `ORNL_AoverE`,

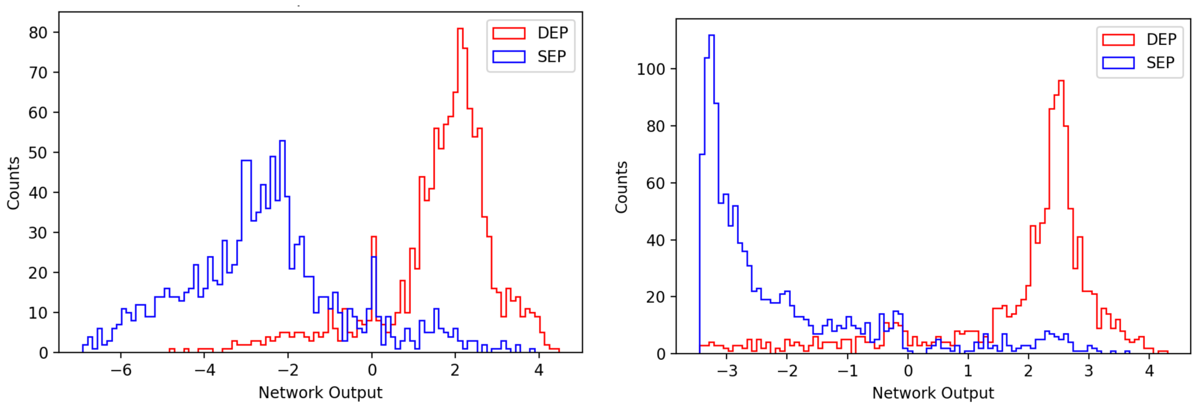

FIGURE 6.5: The distributions of network output for DEP and SEP events on detector P42575B were evaluated with the trained networks. (Left) the distribution with a network trained in the charge domain. (Right) the distribution with a network trained in the current domain.

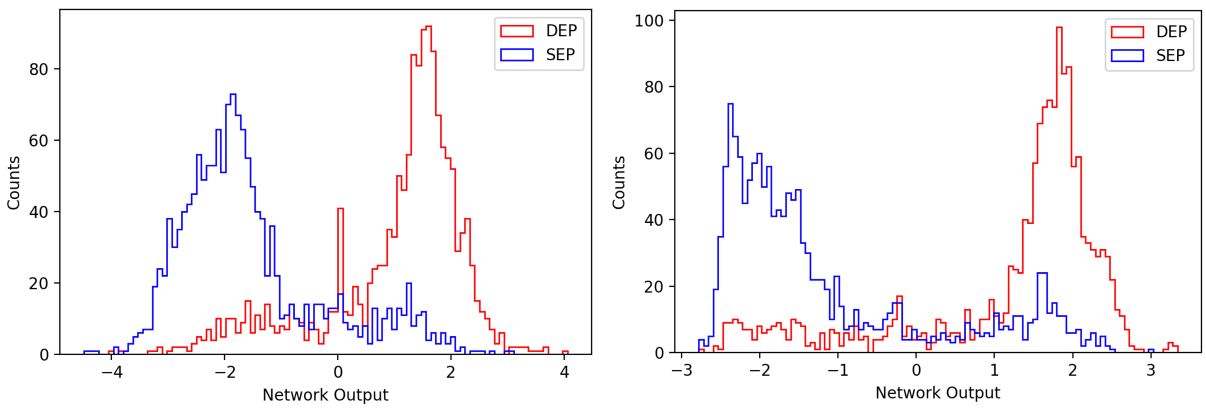

FIGURE 6.6: The distributions of network output for DEP and SEP events on detector P43387A were evaluated with the trained networks. (Left) the distribution with a network trained in the charge domain. (Right) the distribution with a network trained in the current domain.

represented by A/E_ORNL, for ICPC detectors. These parameters are tuned for both types of detectors to accept 90% DEP events [144, 145].

We assumed all the waveforms from SEP as true background-like and all the waveforms from DEP as true signal-like events and labeled them accordingly. The left and right plots in Fig. 6.7, and Fig. 6.8 corresponds to SEP and DEP events respectively. The population in the different quadrants in these confusion matrix plots represents the following class of events.

- First quadrant: Events are classified as a signal by both AvsE and network prediction
- Second quadrant: Events are classified as a signal by AvsE but background by the network
- Third quadrant: Events are classified as background by both AvsE and network prediction

- Fourth quadrant: Events are classified as background by AvsE and signal by the network

The population of events in the second and fourth quadrants corresponds to the disagreement between AvsE and the network, and we found a relatively tiny population in those quadrants.

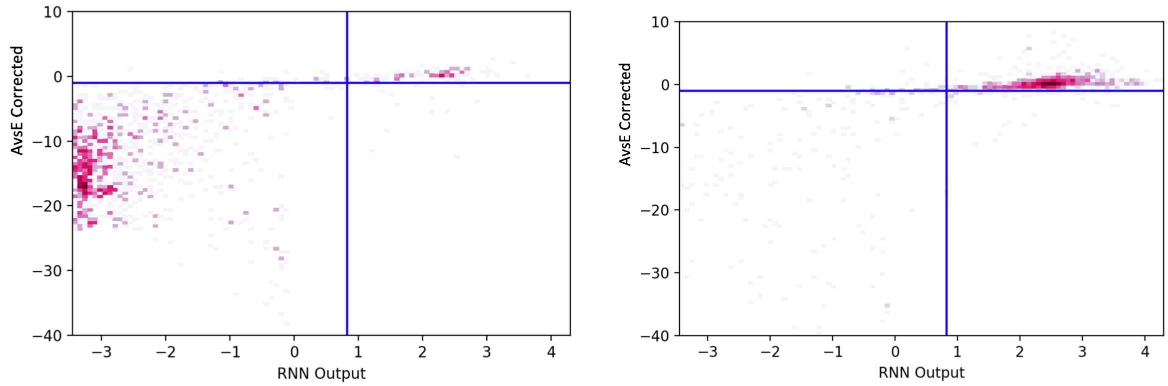

FIGURE 6.7: (Left): Confusion matrix plot based on the AvsE parameter and network output for the detector P42575B, which is a PPC detector . All waveforms belong to the SEP region. Each data point represents the AvsE parameter and network output value in a two-dimensional representation. The waveforms below and above the horizontal line are labeled as background and signal by the AvsE approach, while the waveforms on the right and left of the vertical lines are labeled as signal and background, respectively, by the network. (Right): Similar plot for the waveforms belonging to the DEP region.

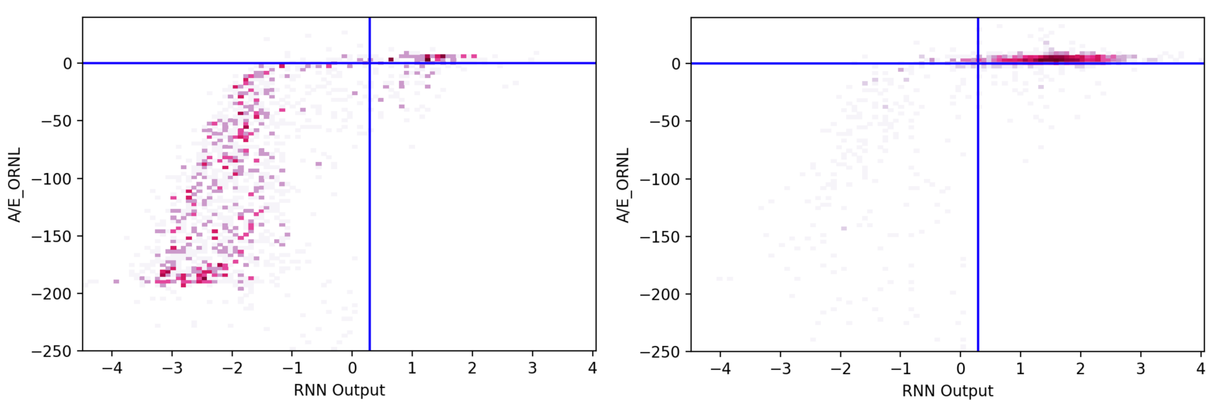

FIGURE 6.8: (Left): Confusion matrix plot for an ICPC detector P43387A based on AvsE approach and network output for the waveforms belonging to the SEP region. (Right): A similar plot for the waveforms belonging to the DEP region. The horizontal and vertical lines represent the cut threshold values for AvsE and network approaches as in Fig. 6.7.

6.5.3 ROC curve and AUC

The quantitative analysis and the comparison of network performance versus the traditional approach of AvsE were done by plotting ROC (Receiver Operating Characteristics) curve. The ROC

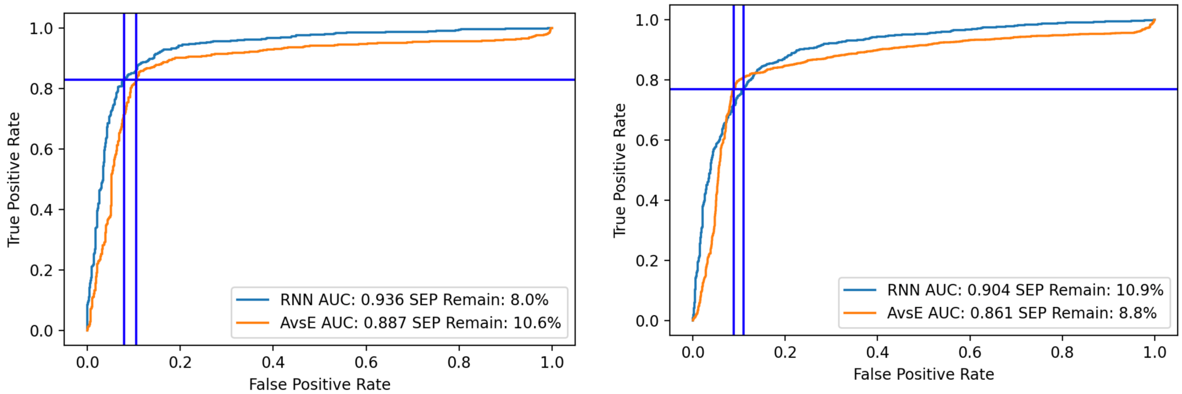

FIGURE 6.9: (Left): The ROC curve generated based on the performance of the network and AvsE to classify single-site and multi-site for the detector P42574B . The acceptance of the true positive rate is fixed to a value based on the fraction of events classified as a signal based on the recommended cut threshold of AvsE. The vertical lines represent the acceptance of background events in the AvsE, and the network approaches. (Right): The similar plot for the detector P43387A, which is a ICPC detector. The acceptance of signal events by the recommended threshold cut was observed to be smaller than in PPC detectors.

curve represents the true positive rate (TPR) versus false positive rate (FPR) when the cut threshold varies. The TPR and FPR can be calculated by using Eqn. 6.5 The AUC (area under curve) score is the quantitative measure that represents the network's ability to separate signal and background classes.

$$\begin{aligned} TPR &= \frac{TP}{TP+FN} \\ FPR &= \frac{FP}{FP+TN} \end{aligned} \tag{6.5}$$

Where TP, TN, FP, and FN are true positive, true negative, false positive, and false negative events.

Generally, higher the AUC values, better is the performance of the model in terms of identifying true signal events as signal and true background events as background events. However, the performance of the network is compared based on acceptance of background while signal acceptance is fixed to same value in the network and AvsE. The approach which give the smaller acceptance of background events is better. Figure 6.11 shows the acceptance of background events with same acceptance of signal events in both approaches. We observed that the network outperforms AvsE approach in nearly all PPC detectors while AvsE is better in ICPCs. The difference is due to slightly different geometry of ICPCs. Furthermore, we observed slightly different distribution in terms of background acceptance with the networks trained in charge and current domains. As seen in Fig. 6.12, background acceptance is slightly smaller with the network trained in charge domain.

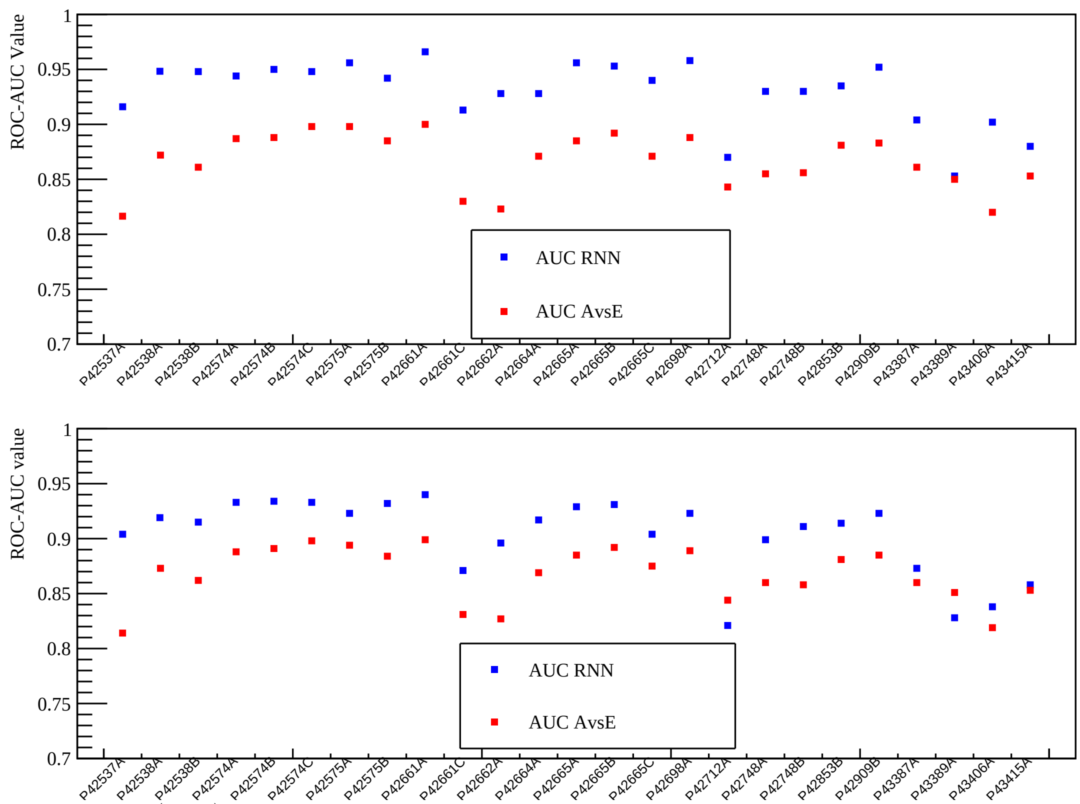

FIGURE 6.10: (Top): AUC-ROC values of all enriched detectors in the DS8 dataset using the trained network in charge domain. (Bottom): The similar plot using the trained network in the current domain.

6.6 Interpretability of the Model

The interpretability of the model refers to the degree to which the cause of the decision is understood. The interpretable model increases the transparency of the decision and helps to understand the model itself better. A model with better interpretability gives the decision based on some easily understood causes. The interpretability of the model we built was driven by the attention mechanism applied to the network. As we discussed in Subsection 6.2, the classification source should be based on a different feature of the rising edge between signal and background events. We plotted the attention score in the different time samples in the waveform, and we observed that the model put more attention score on the rising edge of the waveform, as shown in Fig. 6.13. This indicates that

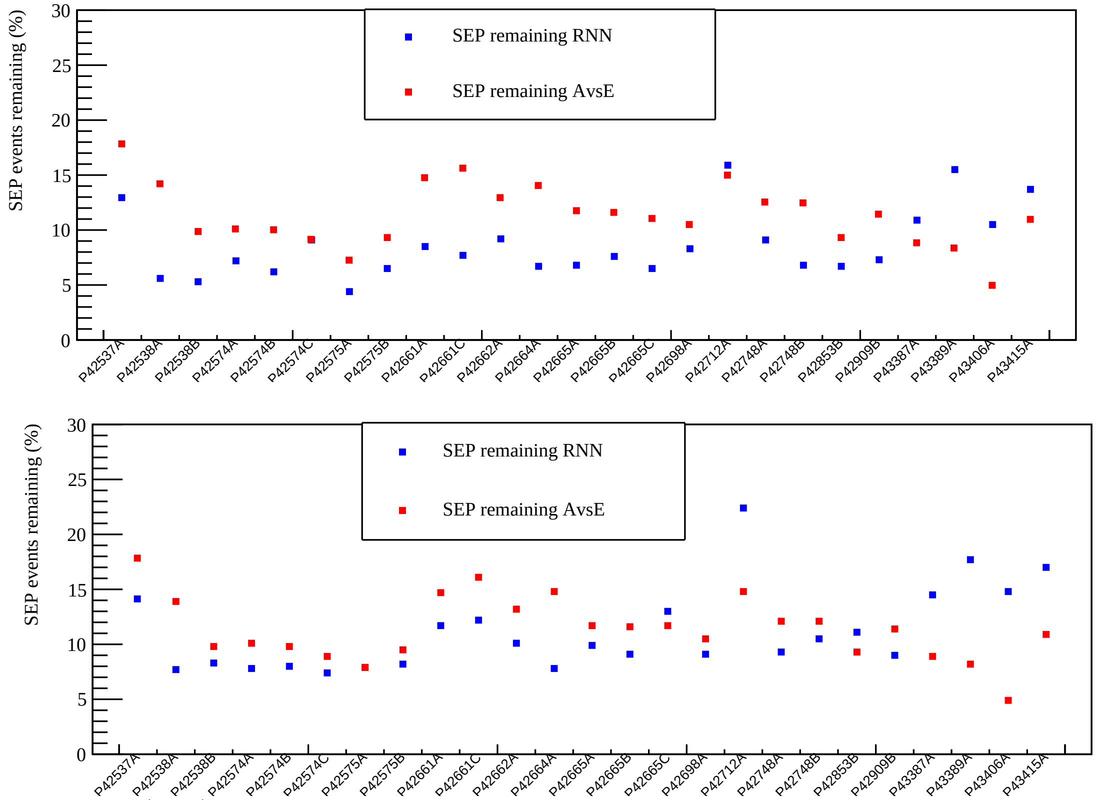

FIGURE 6.11: (Top): Background acceptance rate between AvsE and network approaches with the same signal event acceptance. The network performance was determined by training the network in the charge domain. (Bottom): The similar plot based on the network trained in the current domain.

the model we built can self-explain its source of classification power.

We analyzed some of the waveforms identified as a background by the network and signal by the AvsE approach. Figure 6.14 shows some of such sample waveforms. Since the avse_corr > -1 or A/E_ORNL>0, these waveforms are classified as signal events. However, they look like multi-site events, where one interaction site might be too close to point contact of the detector. AvsE could still be high in these cases, and the waveform might be misidentified as signals. Such waveforms, however, are identified as background by the network.

6.7 Summary

We built an interpretable machine learning model to classify single-site and multi-site events that are proxies to signals and backgrounds in $0\nu\beta\beta$ analysis. The model was trained using normalized DEP and SEP waveforms from the ^{228}Th calibration data. We used all active enriched detectors data in

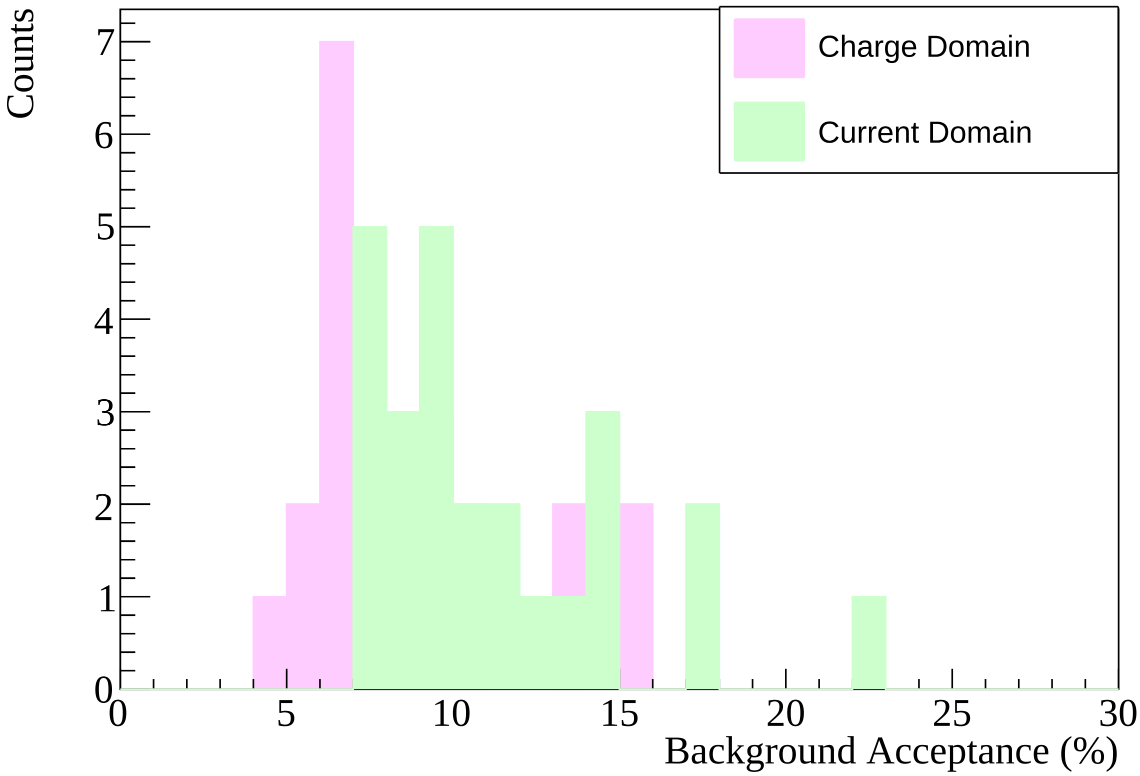

FIGURE 6.12: The distribution of background acceptance in different detectors using the trained network in charge and current domain. Counts on the Y-axis represent the number of detectors. The mean value of background acceptance is slightly better in the charge domain.

dataset DS8. The model was trained using all detector data simultaneously with waveforms in the charge and current domains. The performance of each trained model was evaluated on each detector using the corresponding test dataset and compared with the AvsE approach. In addition, the survival of background events was compared between the model and the AvsE approach, given the same acceptance of signal events. We observed that the model outperformed the traditional approach of AvsE in PPC detectors in both the charge and current domain. However, its performance is slightly poor in ICPC detectors. A model trained with all the detector data simultaneously could be crucial for a next-generation experiment like LEGEND, which uses a large number of detectors. The model outperforms the traditional approach with less parameter tuning in classifying single-site and multi-site events.

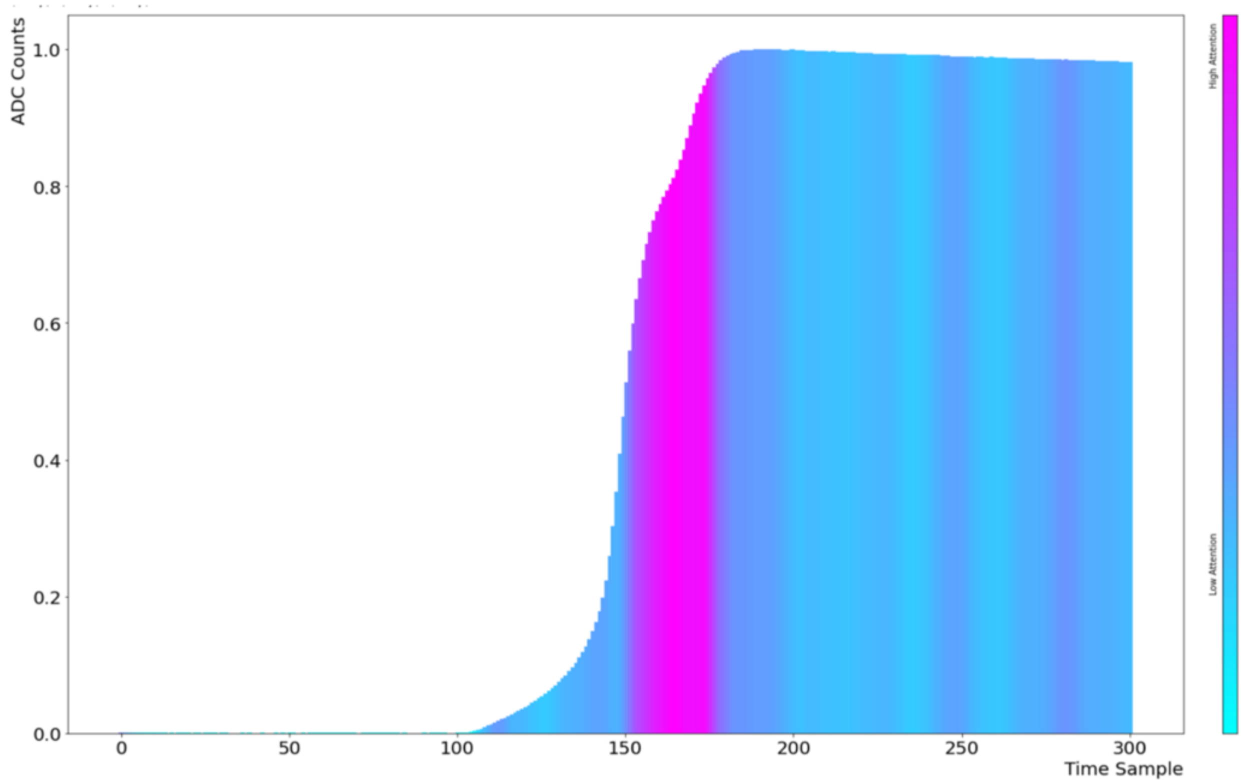

FIGURE 6.13: Attention score on the different time samples of the waveform. The network rejects this waveform by tagging it as multi-site interaction. The network put more attention on the rising edge of the waveform where the feature looks clearly multi-site interaction as expected, demonstrating the interpretability of the network.

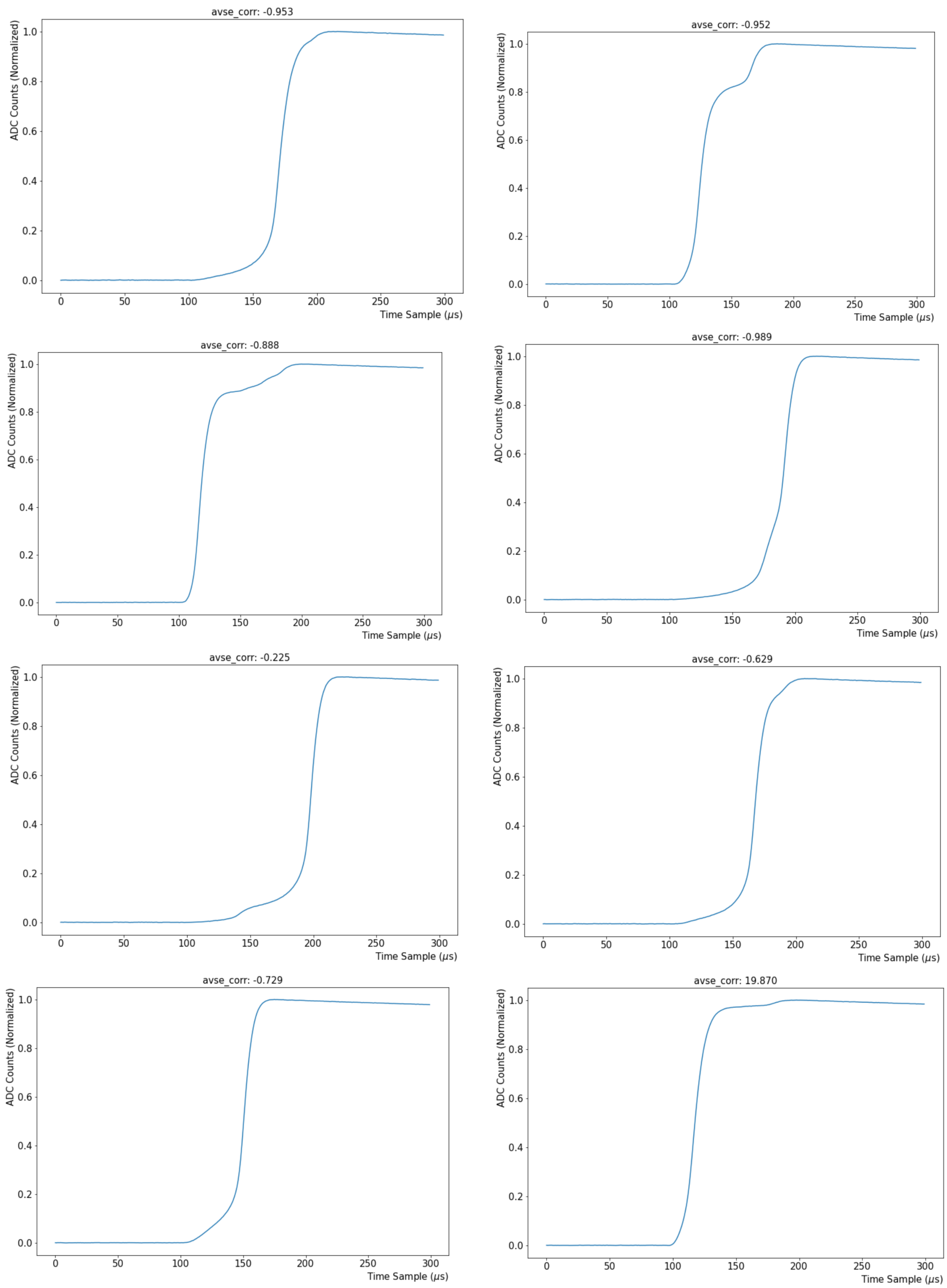

FIGURE 6.14: Some sample waveforms are rejected by the network and accepted by the AvsE approach as signal waveforms. However, these waveforms look like small multi-site events and should be rejected as the network does. Nevertheless, they meet the AvsE criteria to be classified as a signal because one of the interaction sites might be very close to the point contact and has a high enough A that even with the second site, it still ends up high in AvsE. Usually, this only happens if there is a near-point contact event with much energy and one further away with much less energy. The network can identify these background-like events, which the AvsE fails to do so.

7

Summary and Outlook

The observation of $0\nu\beta\beta$ would dramatically revise our understanding of physics and the cosmos. The MAJORANA DEMONSTRATOR searched for $0\nu\beta\beta$ of ^{76}Ge using PPC HPGe detectors. In addition, the DEMONSTRATOR probed a wide range of physics, including the Standard Model and Beyond the Standard Model physics. Furthermore, the proven technologies of the DEMONSTRATOR to use extremely pure materials and low noise electronics are some of the critical assets in building the LEGEND experiment.

This dissertation presents multiple works based on the calibration data, which is an extremely critical component of the physics program and carries many important functions and promises.

The energy resolution of the detectors is one of the critical parameters which directly affect the half-life sensitivity of the $0\nu\beta\beta$ search. The MAJORANA DEMONSTRATOR has achieved world-leading energy resolution with PPC detectors. Overall, an excellent energy performance, including energy linearity on a wide energy scale, has been achieved. These achievements are the results of the intrinsic properties of the PPC detectors and the efforts of detailed analysis, which are described in this dissertation.

(α,n) reactions are one potential source of background for low-background rare-event searches. Experiments with stringent background requirements should understand the background contribution of (α,n) neutrons with reasonable detail and precision. However, precise measurements of (α,n) cross sections are often sparse for the entire range of α-particle energies relevant for (α,n) backgrounds and TALYS-generated cross sections are widely used. In this dissertation, the experimental study of ^{13}C(α,n)^{16}O reaction in the MAJORANA DEMONSTRATOR calibration data and findings are discussed. The consistency found between measurements and predictions, albeit with a large statistical uncertainty, suggests that the TALYS-based NeuCBOT software can predict (α, n) reaction rates reasonably well. The findings described in the dissertation are broadly applicable because thorium is one of the most common impurities, and carbon-rich materials are often used in considerable amounts in low-background experiments. In addition, the combination of TALYS-based software with GEANT4 has been used to estimate the background contribution from the (α, n) reactions for $0\nu\beta\beta$ searches.

Excellent energy performance is observed beyond 3 MeV as well in the MAJORANA DEMONSTRATOR. The higher energy γ-peaks (above 3 MeV) were analyzed in terms of energy resolution and linearity. The 5229-keV peak from the double coincidence of 2614 keV events and the 6129-keV peak were observed with expected resolutions at expected positions. The findings support the higher energy searches in the MAJORANA DEMONSTRATOR.

A good agreement between the observed and expected activities of the calibration source assemblies is observed over multiple years of data-taking. The observed activity is calculated based on the raw event rate and efficiencies from the simulations performed in MAGE, while the expected activity is calculated based on the vendor-reported value. The agreement suggests robust performance of the MAGE simulation and is reported for the first time in this work. MAGE is the official simulation package of the MAJORANA DEMONSTRATOR, which is also used by GERDA and LEGEND, and this work adds more credibility to the simulation results of these experiments.

In rare-event searches, it is crucial to estimate the background, investigate the background sources, and develop techniques to discriminate them from signals. Different pulse shape-based analysis algorithms are developed in the MAJORANA DEMONSTRATOR. In this dissertation, a machine learning approach and its performance are discussed. An interpretable machine learning model has been built, capable of efficiently discriminating single-site and multi-site events, which are proxies to signals and backgrounds in $0\nu\beta\beta$ searches. The performance is as good as the traditional approach of AvsE with far less parameter tuning. Also, the model can be trained with all detector data simultaneously, which can benefit future experiments with a large number of detectors like

LEGEND.

The work presented in this dissertation directly impacts LEGEND and can be extended. LEGEND will use a similar calibration procedure and plans to maintain the energy performance. LEGEND is aware of neutrons from the calibration sources, and a different design is adapted. The software used here is also used to predict radiogenic neutron background in LEGEND. Last but not least, the machine learning method is actively being investigated, and it is promising to use in LEGEND.

Bibliography

[1] J. Chadwick, Verh. Phys. Gesell. **16**, 383 (1914).

[2] C. D. Ellis, Proceedings of the Royal Society of London. Series A, Containing Papers of a Mathematical and Physical Character **99**, 261 (1921).

[3] C. D. Ellis and W. A. Wooster, Proceedings of the Royal Society of London. Series A, Containing Papers of a Mathematical and Physical Character **117**, 109 (1927).

[4] L. Meitner and W. Orthmann, Zeitschrift fur Physik **60**, 143 (1930).

[5] J. Chadwick, Proceedings of the Royal Society of London. Series A, Containing Papers of a Mathematical and Physical Character **136**, 692 (1932).

[6] E. Fermi, Z. Phys. **88**, 161 (1934).

[7] K. Collaboration *et al.*, arXiv preprint hep-ex/0109033 (2001).

[8] C. L. Cowan Jr, F. Reines, F. Harrison, H. Kruse, and A. McGuire, Science **124**, 103 (1956).

[9] T. D. Lee and C. N. Yang, Phys. Rev. **104**, 254 (1956).

[10] C.-S. Wu, E. Ambler, R. Hayward, D. Hoppes, and R. P. Hudson, Physical review **105**, 1413 (1957).

[11] M. Goldhaber, L. Grodzins, and A. Sunyar, Physical Review **109**, 1015 (1958).

[12] J. Steinberger, Physical Review **74**, 500 (1948).

[13] G. Danby, J. M. Gaillard, K. Goulianos, L. M. Lederman, N. Mistry, M. Schwartz, and J. Steinberger, Physical Review Letters **9**, 36 (1962).

[14] M. L. Perl, G. Abrams, A. Boyarski, M. Breidenbach, D. Briggs, F. Bulos, W. Chinowsky, J. Dakin, G. Feldman, C. Friedberg, *et al.*, Physical Review Letters **35**, 1489 (1975).

[15] K. Kodama, N. Ushida, C. Andreopoulos, N. Saoulidou, G. Tzanakos, P. Yager, B. Baller, D. Boehnlein, W. Freeman, B. Lundberg, *et al.*, Physics Letters B **504**, 218 (2001).

[16] S. L. Glashow, Nuclear physics **22**, 579 (1961).

[17] S. Weinberg, Physical review letters **19**, 1264 (1967).

[18] A. Salam, in *Selected Papers Of Abdus Salam: (With Commentary)* (World Scientific, 1994) pp. 244–254.

[19] D. J. Gross and F. Wilczek, Physical Review Letters **30**, 1343 (1973).

[20] B. Pontecorvo, Zhur. Eksptl'. i Teoret. Fiz. **34** (1958).

[21] Z. Maki, M. Nakagawa, and S. Sakata, Progress of Theoretical Physics **28**, 870 (1962).

[22] R. Davis Jr, D. S. Harmer, and K. C. Hoffman, Physical Review Letters **20**, 1205 (1968).

[23] B. T. Cleveland, T. Daily, R. Davis Jr, J. R. Distel, K. Lande, C. Lee, P. S. Wildenhain, and J. Ullman, The Astrophysical Journal **496**, 505 (1998).

[24] J. N. Bahcall, N. A. Bahcall, and G. Shaviv, Physical Review Letters **20**, 1209 (1968).

[25] V. Gribov and B. Pontecorvo, Physics Letters B **28**, 493 (1969).

[26] B. Kayser, Neutrino Mass , 1 (2003).

[27] S. Abe, T. Ebihara, S. Enomoto, K. Furuno, Y. Gando, K. Ichimura, H. Ikeda, K. Inoue, Y. Kibe, Y. Kishimoto, *et al.*, Physical review letters **100**, 221803 (2008).

[28] Q. R. Ahmad, R. Allen, T. Andersen, J. Anglin, J. Barton, E. Beier, M. Bercovitch, J. Bigu, S. Biller, R. Black, *et al.*, Physical review letters **89**, 011301 (2002).

[29] Y. Fukuda, T. Hayakawa, E. Ichihara, K. Inoue, K. Ishihara, H. Ishino, Y. Itow, T. Kajita, J. Kameda, S. Kasuga, *et al.*, Physical review letters **81**, 1562 (1998).

[30] K. Eguchi, S. Enomoto, K. Furuno, J. Goldman, H. Hanada, H. Ikeda, K. Ikeda, K. Inoue, K. Ishihara, W. Itoh, *et al.*, Physical Review Letters **90**, 021802 (2003).

[31] P. F. de Salas, D. Forero, S. Gariazzo, P. Martínez-Miravé, O. Mena, C. Ternes, M. Tórtola, and J. Valle, Journal of High Energy Physics **2021**, 1 (2021).

[32] V. Antonelli, L. Miramonti, and G. Ranucci, Universe **6**, 52 (2020).

[33] P. A. M. Dirac, Proceedings of the Royal Society of London. Series A, Containing Papers of a Mathematical and Physical Character **117**, 610 (1928).

[34] E. Majorana, Nuovo Cim **14**, 50 (1937).

[35] A. Balantekin and B. Kayser, arXiv preprint arXiv:1805.00922 (2018).

[36] T. Ohlsson and S. Zhou, Nature Communications **5**, 1 (2014).

[37] F. R. Klinkhamer and N. S. Manton, Physical Review D **30**, 2212 (1984).

[38] A. D. Sakharov, in *In The Intermissions... Collected Works on Research into the Essentials of Theoretical Physics in Russian Federal Nuclear Center, Arzamas-16* (World Scientific, 1998) pp. 84–87.

[39] M. Goeppert-Mayer, Physical Review **48**, 512 (1935).

[40] R. Saakyan, Annual Review of Nuclear and Particle Science **63**, 503 (2013).

[41] S. Elliott, A. Hahn, and M. Moe, Physical Review Letters **59**, 2020 (1987).

[42] G. Racah, Nuovo cimento **14**, 322 (1937).

[43] E. Majorana, Il Nuovo Cimento (1924-1942) **14**, 171 (1937).

[44] W. Furry, Physical Review **56**, 1184 (1939).

[45] J. C. Helo, M. Hirsch, T. Ota, and F. dos Santos, Journal of High Energy Physics **2015**, 1 (2015).

[46] J. Vergados, H. Ejiri, and F. Šimkovic, Reports on Progress in Physics **75**, 106301 (2012).

[47] J. Schechter and J. W. Valle, Physical Review D **25**, 2951 (1982).

[48] S. Stoica and M. Mirea, Frontiers in Physics **7**, 12 (2019).

[49] J. Engel and J. Menéndez, Reports on Progress in Physics **80**, 046301 (2017).

[50] F. T. Avignone III, S. R. Elliott, and J. Engel, Reviews of Modern Physics **80**, 481 (2008).

[51] S. Dell'Oro, S. Marcocci, and F. Vissani, Physical Review D **90**, 033005 (2014).

[52] N. Abgrall *et al.* (LEGEND Collaboration), arXiv preprint arXiv:2107.11462 (2021), 2107.11462 .

[53] V. I. Tretyak and Y. G. Zdesenko, Atomic Data and Nuclear Data Tables **80**, 83 (2002).

[54] M. J. Dolinski, A. W. Poon, and W. Rodejohann, arXiv preprint arXiv:1902.04097 (2019).

[55] S. Alvis, I. Arnquist, F. Avignone III, A. Barabash, C. Barton, V. Basu, F. Bertrand, B. Bos, M. Busch, M. Buuck, *et al.*, Physical Review C **100**, 025501 (2019).

[56] M. Agostini, G. Araujo, A. Bakalyarov, M. Balata, I. Barabanov, L. Baudis, C. Bauer, E. Bellotti, S. Belogurov, A. Bettini, *et al.*, Physical review letters **125**, 252502 (2020).

[57] I. Arnquist, F. Avignone III, A. Barabash, C. Barton, P. Barton, K. Bhimani, E. Blalock, B. Bos, M. Busch, M. Buuck, *et al.*, arXiv preprint arXiv:2207.07638 (2022).

[58] O. Azzolini, J. Beeman, F. Bellini, M. Beretta, M. Biassoni, C. Brofferio, C. Bucci, S. Capelli, V. Caracciolo, L. Cardani, *et al.*, arXiv preprint arXiv:2206.05130 (2022).

[59] A. Li, theKamLAND Zen Collaboration, *et al.*, in *Journal of Physics: Conference Series*, Vol. 1468 (IOP Publishing, 2020) p. 012201.

[60] I. Nutini, D. Adams, C. Alduino, K. Alfonso, F. Avignone III, O. Azzolini, G. Bari, F. Bellini, G. Benato, M. Beretta, *et al.*, International Journal of Modern Physics A **37**, 2240014 (2022).

[61] G. Anton, I. Badhrees, P. Barbeau, D. Beck, V. Belov, T. Bhatta, M. Breidenbach, T. Brunner, G. Cao, W. Cen, *et al.*, Physical review letters **123**, 161802 (2019).

[62] R. Arnold, C. Augier, A. Barabash, A. Basharina-Freshville, S. Blondel, S. Blot, M. Bongrand, D. Boursette, V. Brudanin, J. Busto, *et al.*, The European Physical Journal C **78** (2018).

[63] J. Heise, in *Journal of Physics: Conference Series*, Vol. 606 (IOP Publishing, 2015) p. 012015.

[64] M. Agostini, G. Benato, J. A. Detwiler, J. Menéndez, and F. Vissani, Physical Review C **104**, L042501 (2021).

[65] I. J. Arnquist *et al.* (Majorana Collaboration), Phys. Rev. C **103**, 015501 (2021).

[66] S. I. Alvis *et al.* (Majorana Collaboration), Phys. Rev. Lett. **120**, 211804 (2018).

[67] N. Abgrall *et al.* (Majorana Collaboration), Phys. Rev. Lett. **118**, 161801 (2017).

[68] N. Abgrall *et al.* (Majorana Collaboration), The European Physical Journal C **76** (2016).

[69] S. I. Alvis *et al.* (Majorana Collaboration), Phys. Rev. D **99**, 072004 (2019).

[70] N. Abgrall, I. J. Arnquist, F. Avignone Iii, H. O. Back, A. S. Barabash, F. Bertrand, M. Boswell, A. Bradley, V. Brudanin, M. Busch, *et al.*, Nuclear Instruments and Methods in Physics Research Section A: Accelerators, Spectrometers, Detectors and Associated Equipment **828**, 22 (2016).

[71] C. Christofferson, N. Abgrall, S. Alvis, I. Arnquist, F. Avignone III, A. Barabash, C. Barton, F. Bertrand, T. Bode, A. Bradley, *et al.*, in *AIP Conference Proceedings*, Vol. 1921 (AIP Publishing LLC, 2018) p. 060005.

[72] N. Abgrall, M. Amman, I. Arnquist, F. Avignone, A. Barabash, C. Barton, P. Barton, F. Bertrand, K. Bhimani, B. Bos, *et al.*, Journal of Instrumentation **17**, T05003 (2022).

[73] N. Abgrall, E. Aguayo, F. Avignone III, A. Barabash, F. Bertrand, A. Bradley, V. Brudanin, M. Busch, M. Buuck, D. Byram, *et al.*, Astroparticle Physics **93**, 70 (2017).

[74] P. A. Burns, L. J. Martin, and J. R. Moroney, Nuclear Instruments and Methods in Physics Research Section A: Accelerators, Spectrometers, Detectors and Associated Equipment **286**, 480 (1990).

[75] P. Barton, P. Luke, M. Amman, Y.-D. Chan, J. Detwiler, J. Loach, R. Martin, A. Poon, C. Tindall, and K. Vetter, in *2011 IEEE Nuclear Science Symposium Conference Record* (IEEE, 2011) pp. 1976–1979.

[76] D.-M. Mei and A. Hime, Physical Review D **73**, 053004 (2006).

[77] S. I. Alvis *et al.* (Majorana Collaboration), Phys. Rev. C **99**, 065501 (2019).

[78] I. Arnquist, F. Avignone, A. Barabash, C. Barton, F. Bertrand, E. Blalock, B. Bos, M. Busch, M. Buuck, T. Caldwell, *et al.*, The European Physical Journal C **82**, 1 (2022).

[79] C. E. Aalseth, N. Abgrall, E. Aguayo, S. Alvis, M. Amman, I. J. Arnquist, F. Avignone III, H. O. Back, A. S. Barabash, P. Barbeau, *et al.*, Phys. Rev. Lett. **120**, 132502 (2018).

[80] I. J. Arnquist *et al.* (Majorana Collaboration), Phys. Rev. C **105**, 014617 (2022).

[81] I. J. Arnquist *et al.* (Majorana Collaboration), Phys. Rev. C **105**, 064610 (2022).

[82] I. Arnquist, F. Avignone III, A. Barabash, C. Barton, E. Blalock, B. Bos, M. Busch, M. Buuck, T. Caldwell, Y. Chan, *et al.*, arXiv preprint arXiv:2202.01343 (2022).

[83] I. Arnquist, F. Avignone III, A. Barabash, C. Barton, K. Bhimani, E. Blalock, B. Bos, M. Busch, M. Buuck, T. Caldwell, *et al.*, arXiv preprint arXiv:2203.02033 (2022).

[84] I. Arnquist, F. Avignone III, A. Barabash, C. Barton, K. Bhimani, E. Blalock, B. Bos, M. Busch, M. Buuck, T. Caldwell, *et al.*, arXiv preprint arXiv:2206.05789 (2022).

[85] I. Arnquist, F. Avignone III, A. Barabash, C. Barton, K. Bhimani, E. Blalock, B. Bos, M. Busch, M. Buuck, T. Caldwell, *et al.*, arXiv preprint arXiv:2206.10638 (2022).

[86] J. T. Anderson, R. Brito, D. Doering, T. Hayden, B. Holmes, J. Joseph, H. Yaver, and S. Zimmermann, in *2007 IEEE Nuclear Science Symposium Conference Record*, Vol. 3 (2007) pp. 1751–1756.

[87] N. Abgrall *et al.* (Majorana Collaboration), IEEE Transactions on Nuclear Science **68**, 359 (2021).

[88] W. R. Leo, *Techniques for nuclear and particle physics experiments: a how-to approach* (Springer Science & Business Media, 2012).

[89] V. T. Jordanov and G. F. Knoll, Nuclear Instruments and Methods in Physics Research Section A: Accelerators, Spectrometers, Detectors and Associated Equipment **345**, 337 (1994).

[90] N. Abgrall, I. Arnquist, F. Avignone III, A. Barabash, F. Bertrand, M. Boswell, A. Bradley, V. Brudanin, M. Busch, M. Buuck, *et al.*, Nuclear Instruments and Methods in Physics Research Section A: Accelerators, Spectrometers, Detectors and Associated Equipment **872**, 16 (2017).

[91] L. Longoria, A. Naboulsi, P. Gray, and T. MacMahon, Nuclear Instruments and Methods in Physics Research Section A: Accelerators, Spectrometers, Detectors and Associated Equipment **299**, 308 (1990).

[92] M. Hammed, P. Gray, A. Naboulsi, and T. Mac Mahon, Nuclear Instruments and Methods in Physics Research Section A: Accelerators, Spectrometers, Detectors and Associated Equipment **334**, 543 (1993).

[93] G. Kanisch, Nuclear Instruments and Methods in Physics Research Section A: Accelerators, Spectrometers, Detectors and Associated Equipment **855**, 118 (2017).

[94] I. S. Guinn, *The Search for Double-Beta Decay to Excited States in 76-Ge using the* MAJORANA DEMONSTRATOR, Ph.D. thesis, University of Washington (2019).

[95] F. James and M. Roos, Comput. Phys. Commun. **10**, 343 (1975).

[96] R. Brun and F. Rademakers, Nuclear instruments and methods in physics research section A: accelerators, spectrometers, detectors and associated equipment **389**, 81 (1997).

[97] S. Duane, A. D. Kennedy, B. J. Pendleton, and D. Roweth, Physics letters B **195**, 216 (1987).

[98] R. M. Neal *et al.*, Handbook of markov chain monte carlo **2**, 2 (2011).

[99] M. Girolami and B. Calderhead, Journal of the Royal Statistical Society: Series B (Statistical Methodology) **73**, 123 (2011).

[100] P. Chu *et al.*, "Energy performance of the Majorana Demonstrator," ().

[101] P. Chu *et al.*, "Energy systematic of Majorana Demonstrator (Internal)," ().

[102] N. Abgrall *et al.* (Majorana Collaboration), IEEE Transactions on Nuclear Science **68**, 359 (2021).

[103] M. Carson *et al.*, Astroparticle Physics **21**, 667–687 (2004).

[104] J. Cooley *et al.*, Nuclear Instruments and Methods in Physics Research Section A: Accelerators, Spectrometers, Detectors and Associated Equipment **888**, 110–118 (2018).

[105] Z. Chen, X. Zhang, Z. Yu, J. Cao, and C. Yang, Phys. Rev. D **104**, 092006 (2021).

[106] M. Febbraro *et al.*, Phys. Rev. Lett. **125**, 062501 (2020).

[107] W. B. Wilson, R. T. Perry, E. F. Shores, W. S. Charlton, T. A. Parish, G. P. Estes, T. H. Brown, E. D. Arthur, M. Bozoian, T. R. England, D. G. Madland, and J. E. Stewart, (2002).

[108] S. S. Westerdale, (2016), 10.2172/1350520.

[109] P. Mohr, Phys. Rev. C **97**, 064613 (2018).

[110] J. Zhao, Z.-Y. Yu, J.-L. Liu, X.-B. Li, F.-H. Zhang, and D.-M. Xia, Chinese Physics C **38**, 116201 (2014).

[111] B. Guo *et al.*, The Astrophysical Journal **756**, 193 (2012).

[112] M. La Cognata *et al.*, The Astrophysical Journal **777**, 143 (2013).

[113] S. Cristallo *et al.*, The Astrophysical Journal **859**, 104 (2018).

[114] M. Arnould and S. Goriely, Progress in Particle and Nuclear Physics **112**, 103766 (2020).

[115] C. N. Davids, Nuclear Physics A **110**, 619 (1968).

[116] M. Heil *et al.*, Phys. Rev. C **78**, 025803 (2008).

[117] J. K. Bair and F. X. Haas, Phys. Rev. C **7**, 1356 (1973).

[118] H. Drotleff, A. Denker, H. Knee, M. Soine, and G. Wolf, The Astrophysical Journal **414**, 735 (1993).

[119] S. Harissopulos *et al.*, Phys. Rev. C **72**, 062801 (2005).

[120] C. Broggini, D. Bemmerer, A. Caciolli, and D. Trezzi, Progress in Particle and Nuclear Physics **98**, 55 (2018).

[121] W. A. Peters, Phys. Rev. C **96**, 029801 (2017).

[122] A. Koning, S. Hilaire, and S. Goriely, User Manual, NRG, The Netherlands (2013).

[123] M. Chadwick *et al.*, Nuclear Data Sheets **112**, 2887 (2011), special Issue on ENDF/B-VII.1 Library.

[124] S. Westerdale and P. Meyers, Nuclear Instruments and Methods in Physics Research Section A: Accelerators, Spectrometers, Detectors and Associated Equipment **875**, 57 (2017).

[125] R. Ajaj *et al.* (DEAP Collaboration), Phys. Rev. D **100**, 022004 (2019).

[126] J. Tuli, Nuclear Instruments and Methods in Physics Research Section A: Accelerators, Spectrometers, Detectors and Associated Equipment **369**, 506 (1996).

[127] J. F. Ziegler, M. D. Ziegler, and J. P. Biersack, Nuclear Instruments and Methods in Physics Research Section B: Beam Interactions with Materials and Atoms **268**, 1818 (2010).

[128] M. Bhike, B. Fallin, Krishichayan, and W. Tornow, Physics Letters B **741**, 150 (2015).

[129] C. Wiesinger, L. Pandola, and S. Schönert, The European Physical Journal C **78** (2018).

[130] S. Agostinelli *et al.* (GEANT4 Collaboration), Nuclear Instruments and Methods in Physics Research Section A: Accelerators, Spectrometers, Detectors and Associated Equipment **506**, 250 (2003).

[131] M. Boswell *et al.*, IEEE Transactions on Nuclear Science **58**, 1212 (2011).

[132] L. Baudis *et al.*, Journal of Instrumentation **10**, P12005 (2015).

[133] I. Arnquist, F. Avignone III, A. Barabash, C. Barton, K. Bhimani, E. Blalock, B. Bos, M. Busch, M. Buuck, T. Caldwell, *et al.*, arXiv preprint arXiv:2203.14228 (2022).

[134] G. J. Feldman and R. D. Cousins, Phys. Rev. D **57**, 3873 (1998).

[135] R. Heaton, H. Lee, P. Skensved, and B. Robertson, Nuclear Instruments and Methods in Physics Research Section A: Accelerators, Spectrometers, Detectors and Associated Equipment **276**, 529 (1989).

[136] M. Agostini, M. Allardt, E. Andreotti, A. Bakalyarov, M. Balata, I. Barabanov, M. Barnabé Heider, N. Barros, L. Baudis, C. Bauer, *et al.*, The European Physical Journal C **73**, 1 (2013).

[137] A. Caldwell, F. Cossavella, B. Majorovits, D. Palioselitis, and O. Volynets, The European Physical Journal C **75**, 1 (2015).

[138] S. Delaquis, M. Jewell, I. Ostrovskiy, M. Weber, T. Ziegler, J. Dalmasson, L. Kaufman, T. Richards, J. Albert, G. Anton, *et al.*, Journal of Instrumentation **13**, P08023 (2018).

[139] S. Hochreiter and J. Schmidhuber, Neural computation **9**, 1735 (1997).

[140] K. Cho, B. Van Merriënboer, C. Gulcehre, D. Bahdanau, F. Bougares, H. Schwenk, and Y. Bengio, arXiv preprint arXiv:1406.1078 (2014), 10.48550/ARXIV.1406.1078.

[141] D. Bahdanau, K. Cho, and Y. Bengio, arXiv preprint arXiv:1409.0473 (2014), 10.48550/ARXIV.1409.0473.

[142] A. Paszke, S. Gross, F. Massa, A. Lerer, J. Bradbury, G. Chanan, T. Killeen, Z. Lin, N. Gimelshein, L. Antiga, *et al.*, Advances in neural information processing systems **32** (2019).

[143] S. Karsoliya, International Journal of Engineering Trends and Technology **3**, 714 (2012).

[144] C. C. Nick Ruof, Walter Pettus, "Multi-site event discrimination for the MAJORANA DEMONSTRATOR," .

[145] V. Guiseppe, J. Lopez, D. Radford, R. Varner, and C.-H. Yu, "ORNL analysis," .